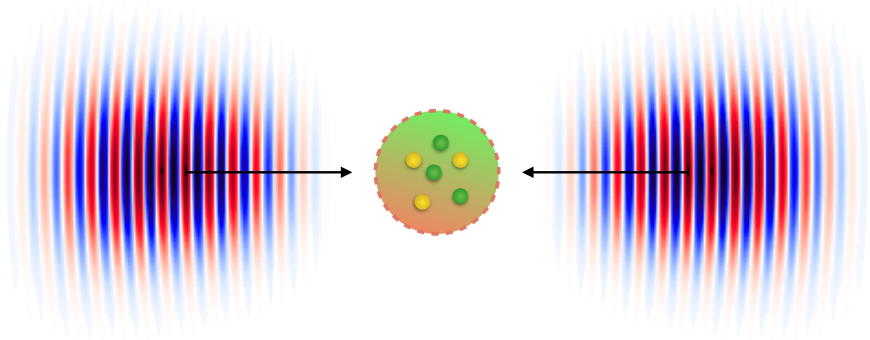

# Vacuum Polarization Solver

**Pedro Vidal Cabrita Carneiro**

Thesis to obtain the Master of Science Degree in

**Engineering Physics**

**Supervisors**
Prof. Luís Miguel de Oliveira e Silva
Dr. Thomas Emmanuel Aurelien Grismayer

**Examination Committee**
Chairperson: Prof.Luís Paulo da Mota Capitão Lemos Alves
Supervisor: Dr. Thomas Emmanuel Aurelien Grismayer
Members of the Committee: Prof. Vasco António Dinis Leitão Guerra
Prof. José Tito da Luz Mendonça

**September 2016**

# Acknowledgements

The thesis about to be presented, which I am very proud of, is the result of thousands of hours invested by many people both directly in the work, but also invested in my development by the means of education and/or friendship. I will attempt to do justice by thanking all of you.

To Thomas Grismayer, one of my supervisors and the older brother I never had; thank you for all the amusing hours we spent together producing this work, but also for all the physics you taught me and for all the fun we had researching things like how many times Sommerfeld was nominated for Nobel prize, how many red cards Sergio Ramos has had. Besides being an excellent supervisor, you taught me valuable personal skills to overcome my shyness and always leading our work by giving the example of never giving up and placing the quality of the physics above all else. To my other supervisor, Luís Oliveira e Silva, for all you invested in me, for your availability to solve every problem in order to protect your own, your strategic vision regarding the frontiers of science and for working in your sleep to provide outstanding conditions to all researchers at the Group of lasers and Plasmas (GoLP). One thing we all learned for sure is that there are certain carriages in German trains in which one must be careful when talking!

To my teachers in MEFT, I believe you never get enough credit for your work (just the opposite in fact). A special thanks to some of my best, most inspirational teachers, Vasco Guerra, Filipe Joaquim, Luís Lemos Alves, Nuno Loureiro, Jorge Romão and Teresa Peña.

To Isabel Ribeiro, a true mentor since day 1, to whom I owe so much.

To my friends, Rui André present from the moment we changed course to physics, always ready to put the well-being of others above your own and to play 'cabecudos', André Martins for proofreading my thesis and for our friendship that will surely last, Fábio Cruz for your true friendship and for our great travels (uhh, laser, yes yes), Paulo Ratinho for all the fun conversations but also for what you taught me and your honest advice, and Vitor Hariton for our afternoon conversations. To my *Squadra Azzura*, specially Fabrizio, for our deep conversations and sincere friendship. To Swen Künzel, for always knowing what the status is and mentoring me through these years by teaching me to challenge common thought.
To all the people at GoLP for all the pleasent lunches, team meetings and GoLP days. Thank you to Nitin since day one, Marija for her constant energy, Jorge for our pleasent conversations, Ricardo for all his help on the tricky technical aspects but also for always being available and all other team members for the great time we all had.

To my Family, you deserve a special acknowledgment. To my father and brother for being my best friends; I will always treasure all the benfica games, golf matches and so many other great moments. To my sister, please remain confident and true. To all my cousins for always looking up to me and supporting me. Finally, to my grandparents, who always tooke me in as their son and moulded my character. To my grandmother, Maria do Carmo, you took me in 6 years ago and took care of me as a

true son. I am glad to have become your friend and come to admire you're attitude towards others. To my mother for all her love, sacrifice and hard work to assure me and my brothers had the best education and conditions to thrive in happiness, I would like to dedicate this work to you :)

To Marta, for all her sacrifice during the past 5 years so that I could achieve my academic and professional goals; for all the *voltinhas* that kept me mentally sane and all the programs at Azambuja, Algarve, Poland, London... you name it. Essentialy, thank you for loving me and making me happy.

# Resumo

Neste trabalho, abordamos a dinâmica do vácuo quântico usando uma teoria semi-clássica desenvolvida por Heisenberg-Euler que trata o vácuo como um meio effetivo introduzindo uma polarização e magnetização, não lineares, como correções às equações de Maxwell. Começamos por rever a origem e validade da teoria desenvolvida efetuando ainda uma revisão da literatura teórica, numérica e experimental. De seguida, apresentamos o resultado do principal objetivo do trabalho: o desenvolvimento de um novo método numérico para resolver o conjunto de equações de Maxwell-Heisenberg-Euler, pela primeira vez, em multi-dimensões.

Testamos a precisão do algoritmo desenvolvido, reproduzindo em 1D a birrefringência do vácuo e a geração de harmónicas num cenário em que se contra-propagam duas ondas planas. A versatilidade do código é demonstrada em 2D ao apresentar resultados de simulações de interações entre 2 impulsos Gaussianos, com parâmetros realistas, que permitem a geração de harmónicas mais elevadas.

Finalmente, fazemos uma análise das assinaturas experimentais que podemos esperar em cenários realistas. Para tal, consideramos um cenário em que se faz interagir um laser ultra-intenso de frequência ótica, com um laser raio-X a sondar o vácuo quântico. Demonstramos a existência de uma elliticidade induzida na polarização da sonda raio-X, tal como uma rotacão no ângulo de polarização. Estes resultados finais mostram a utilidade da ferramenta numérica desenvolvida neste trabalho, tal como as respectivas análises teóricas, que complementam todo o trabalho teórico e experimental desenvolvido pela comunidade, com o objetivo de detetar o vácuo quântico.

**Palavras Chave:** Vácuo Quântico, Heisenberg-Euler, Algoritmo numérico, Equações de Maxwell

# Abstract

In this work we address the quantum dynamics of the vacuum using a semi-classical theory developed by Heisenberg-Euler, treating the vacuum as an effective nonlinear medium by correcting the classical Maxwell's equations with a polarisation and magnetisation of the vacuum. We begin with a review of the derivation and validity of the theory and perform a review of the theoretical, numerical and experimental literature on the subject.

We present the result of the main objective of this thesis: the development of a new numerical method to solve the set o Maxwell-Heisenberg-Euler equations, for the first time, in multi-dimensions.

We then test the precision of the algorithm by reproducing in 1D the birefringence of the vacuum and by comparing the generation of high harmonics in the counter-propagation of two plane waves. The robustness of the code is demonstrated in 2D with simulations of the interaction between two Gaussian pulses, with realistic parameters, generating the respective high harmonics.

Finally, we perform a theoretical analysis and corresponding simulations, of the experimental signatures that can be expected in realistic scenarios. We consider an X-ray laser pulse probing the quantum vacuum by interacting with an ultra-intense optical laser pump. Our results show that an ellipticity is induced in the polarisation of the probe laser, but also a rotation in the angle of polarisation. These results show the usefulness of the numerical tool developed in this work, and the respective theoretical analysis, thus complementing the community's current theoretical and experimental effort to detect the quantum vacuum.

**Key words:** Quantum Vacuum, Heisenberg-Euler, Numerical algorithm, Maxwell's Equations

# Contents

# List of Figures

# List of Tables

# Chapter 1

# Introduction

## 1.1 Vacuum

Vacuum, the Latin word for "an empty space", is a concept deeply rooted in many physical theories. This notion puzzled some of the greatest minds in History. Indeed, Aristotle and Plato themselves argued that such a state of nothingness could not exist [1], whereas in the 13th century the notion of a true vacuum deeply conflicted with God's omnipotence, as it was speculated that God would be unable to produce vacuum [1]. It was not until the 17th century that Torricelli and Blaise Pascal demonstrated a partial vacuum in their famous experiments [1]. With the electromagnetic (EM) description of waves by Maxwell's equations and the advances in thermodyanamics, the idea of a classical vacuum seemed to be well established by the turn of the 19th century. However, this notion was once again revolutionized by Paul Dirac in 1930 by proposing a vacuum filled with an infinite sea of electrons with negative energy [2]. This interpretation solved a delicate issue arising from the solution of Dirac's equation, known as the *radiation catastrophe* whereby if free states of negative energy were to exist, then an electron in a 1s orbital, for example, could decay to a state of negative energy and from that state to one of even lower energy, until a state of $-\infty$ energy thus making the hydrogen atom unstable. The infinite sea interpretation means that an electron from a negative energy state could be excited by absorbing a photon with an energy equal to twice its rest mass, leaving behind a "hole". The consequence of the "hole theory" was stated by Dirac [3]:

*A hole, if there were one, would be a new kind of particle, unkown to experimental physics, having the same mass and opposite charge to an electron.*

This was the first prediction of the existence of the positron, to be experimentally discovered in 1932. The notion of a vacuum as a true state of emptiness was once again modified. In fact, Quantum Electrodynamics (QED) and many other quantum field theories, lend themselves to the same interpretation, making one thing clear: the so called "true" vacuum seems to be rich in dynamics, and not a static state of void. This realisation leads to astonishing physical consequences.

Heisenberg understood the deep implications of the hole theory and in 1934 published two seminal papers on the formalism behind the fluctuations of the quantum vacuum [4, 5]. Heisenberg also proposed that the fluctuations of electron-positron pairs could lead to a quantum nonlinear vacuum [5]. The exact nature of the nonlinearity of the quantum vacuum would become the PhD thesis of

Hans Euler, a student of Heisenberg. From their work resulted the conclusion that the vacuum could be polarized much like any other medium and that this effect could be taken into account, to leading order on the fine structure constant, as corrections to the Maxwell's equations [6].

## 1.2 Motivation

The work developed by Heisenberg-Euler (HE) is known as the QED corrections to Maxwell's equations [6]. The HE model effectively treats the quantum vacuum as a medium whose response is taken into account as extra polarization and magnetization terms in Maxwell's equations. This formalism is extremely useful as it maintains the classical concept of EM fields instead of using the full second quantization formalism. This approach treats the electron-positron pair vacuum in the low field $E \ll E_s$, low frequency $\omega \ll \omega_c$, limit of the EM fields, where the Compton frequency is given by $\omega_c = m_e c^2/\hbar$ and the Schwinger critical field $E_{Sch} = m_e^2 c^3/e\hbar$. The Schwinger field has a value of $E_{Sch} = 1.3 \times 10^{18}$ V/m and was first identified by Sauter [7](although the idea is attributed to Born [8]) as the field strength at which one expects a Dirac sea electron to tunnel into the positive energy continuum, thus polarizing the vacuum (with real particles).

The HE virtual polarization effect remains to be experimentally observed. However, with the expected peak intensities, up to $10^{23} - 10^{24}$ Wcm$^{-2}$, to be delivered by large scale facilities such as the Extreme Light Infrastructure (ELI) or the VULCAN 20 PW project, the regime where these virtual fluctuations can be detected is finally within reach [9]. On the other hand, the existence of exotic astrophysical scenarios such as pulsar and neutron star magnetospheres, are known to contain such extremely high field intensities [10] where these effects play an important role [11].

The main objective of this thesis is to develop an efficient numerical algorithm that can solve the HE modified Maxwell's equations in a self-consistent manner. This tool is to be incorporated in the massively parallel, fully relativistic, Particle-in-Cell code (PIC) Osiris [12]. A PIC code can model the behaviour of multi-species plasmas, in the presence of strong EM fields, at the kinetic scale [13]. Incorporating such a QED Maxwell's equation solver in a PIC code provides an unique opportunity to study the dynamics of the quantum vacuum in any laser-laser interaction, as well as in plasmas of extremely high energy density dominated by EM fields. The scope of this work can, therefore, be divided in three main areas:

- Develop a stable and robust algorithm to solve a set of nonlinear Maxwell equations in multi-dimensions.

- Benchmark and optimization of experimental setups aiming to detect the HE vacuum fluctuations for the first time using laser-laser interactions. A multi-dimensional self-consistent analysis shall be a novelty within the community.

- Reproduce, with simulations, existing predictions within the literature for several setups.

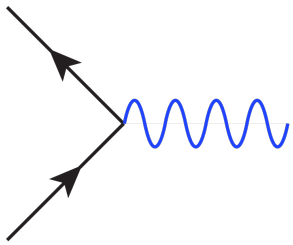

FIGURE 1.1: The fundamental QED vertex. This vertex is deduced from the QED Lagrangian density when a coupling between a relativistic fermion and a EM field is included. The coupling constant is the electron charge e. Using combinations of the fundamental vertex, all interactions and processes in QED can be represented.

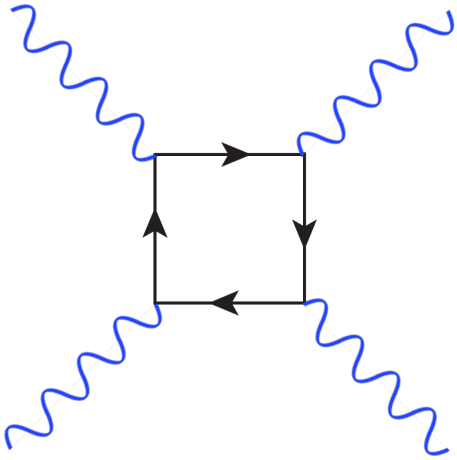

FIGURE 1.2: Feynman diagram of light-by-light scattering. This is the interaction that triggers the virtual vacuum polarization. The naming of "virtual" polarization is due to the fact that the electron-positron pairs are generated as internal fermionic lines in the diagram

## 1.3 Theoretical framework

The theory of QED studies the interactions between fermions and photons using a relatively simple quantum field theory formalism. The theory of QED is one of the most successfully tested theories in physics, in the perturbative regime. As Richard Feynman so eloquently put it:

*"If we measure the distance from New York to Los Angeles, the precision would be the thickness of a human hair."*

This statement is equivalent to a precision of $10^{-8}$. The fundamental QED vertex is shown in Fig.1.1 and can be seen as the coupling of a fermion (electron in this case) with a quantum of the EM field (photon). The constant that couples these two fields is the fine structure constant $\alpha \approx \frac{1}{137}$. As David Griffiths states in his textbook when describing this fundamental vertex, [14],

*"All electromagnetic phenomena are ultimately reducible to the following elementary process."*

Using the fundamental vertex, and combinations of it, we can draw the respective Feynman diagram for each EM process. The HE QED corrections to Maxwell's equations, physically represent the lowest order photon-photon QED interaction. The respective Feynman diagram is shown in Fig.1.2 where it is clear that the photon-photon scattering is due to the polarization of the vacuum via a pair of virtual electron-positron pairs (internal fermionic lines). In their 1936 paper [6], Heisenberg-Euler arrived at the expression for the full nonlinear correction to the Lagrangian of the EM field. Their result is derived from a non-perturbative calculation incorporating all orders in an uniform (background) EM field and can be found in the abstract of their paper:

$$\mathcal{L} = \frac{e^2}{hc}\int_0^\infty \frac{d\eta}{\eta^3} e^{-\eta}\left\{ i\eta^2(\mathbf{E}\cdot\mathbf{B})\frac{\cos\left(\frac{\eta}{E_{Sch}}\sqrt{E^2-B^2+2i(\mathbf{E}\cdot\mathbf{B})}+c.c\right)}{\cos\left(\frac{\eta}{E_{Sch}}\sqrt{E^2-B^2+2i(\mathbf{E}\cdot\mathbf{B})}-c.c\right)} + E_{Sch}^2 + \frac{\eta^2}{3}(B^2-E^2)\right\}, \tag{1.1}$$

Where $E_{Sch}$ is the Schwinger field E,B the background electric and magnetic fields, respectively and $\eta$ a parameter introduced for convenience. The weak field expansion of the Lagrangian ($|E|/E_{Sch} \ll 1$), leads to the modified Maxwell Lagrangian, corrected to the lowest order in QED. This limit is the starting point of this work,

$$\mathcal{L} = \varepsilon_0\mathcal{F} + \xi(4\mathcal{F}^2 + 7\mathcal{G}^2)\,. \tag{1.2}$$

where the effective coupling parameter for this interaction is given by

$$\xi = \frac{20\alpha^2\varepsilon_0^2\hbar^3}{45m_e^4c^5} \sim 10^{-51}\ [\mathrm{Fm/V^2}]\ \ (\mathrm{SI})\,, \tag{1.3}$$

and $\mathcal{F}$ and $\mathcal{G}$ are the two EM invariants, obtained from the Maxwell field tensor $F_{\mu\nu}$:

$$\mathcal{F} = \frac{1}{2}(E^2 - c^2B^2), \qquad \mathcal{G} = c(\mathbf{E}\cdot\mathbf{B}). \tag{1.4}$$

The first term in eq.(1.2) yields the classical Maxwell's equatons in vacuum whereas the remaining terms are the HE QED corrections. Re-writing these expressions in a covariant manner in terms of the field tensor is useful in order to derive the dynamical equations via the Euler-Lagrange equations of motion. We therefore re-write the Lagrangian by noting that

$$\mathcal{F} = \frac{1}{2}(E^2 - c^2B^2) = F^{\mu\nu}F_{\mu\nu}, \tag{1.5}$$

$$\mathcal{G} = c(\mathbf{E}\cdot\mathbf{B}) = -\frac{1}{4}G_{\mu\nu}F^{\mu\nu} = -\frac{1}{8}\epsilon_{\alpha\beta\mu\nu}F^{\alpha\beta}F^{\mu\nu}, \tag{1.6}$$

where $\epsilon_{\alpha\beta\mu\nu}$ is the Levi-Civita symbol. In the theory of fields, the generalized coordinates ($q$,$\dot{q}$), are replaced by fields (functions of coordinates) and their derivatives [14]. In this case, the natural field to identify is the potential 4-vector $A_\mu$, obeying the usual relation $F_{\mu\nu} = \partial_\mu A_\nu - \partial_\nu A_\mu$. The Euler-Lagrange equations that will yield the modified Maxwell's equations are thus:

$$\frac{\partial\mathcal{L}}{\partial A_\mu} - \partial_\nu\left(\frac{\partial\mathcal{L}}{\partial_\nu A_\mu}\right) = 0. \tag{1.7}$$

This is a long but straightforward calculation analogous to the usual derivation of the covariant set of Maxwell's equations. Although the resulting expression is fully covariant, its most useful form is when the indices are explicitly replaced (resulting in vector equations). The final result can be written as:

$$\frac{\partial \mathbf{B}}{\partial t} + \nabla \times \mathbf{E} = 0 \tag{1.8}$$

$$\nabla \cdot \mathbf{B} = 0 \tag{1.9}$$

$$\nabla \times \mathbf{H} - \frac{\partial \mathbf{D}}{\partial t} = 0 \tag{1.10}$$

$$\nabla \cdot \mathbf{D} = 0\,, \tag{1.11}$$

with

$$\mathbf{D} = \epsilon_0 \mathbf{E} + \mathbf{P} \tag{1.12}$$

$$\mathbf{B} = \mu_0 \mathbf{H} + \mathbf{M}\,. \tag{1.13}$$

Equations (1.8)-(1.13) are the usual Maxwell's equations in a medium absent of real currents. The HE QED fluctuations manifest themselves as a nonlinear polarization and magnetization of the vacuum given by:

$$\mathbf{P} = 2\xi \left[2(E^2 - c^2B^2)\mathbf{E} + 7c^2(\mathbf{E}\cdot\mathbf{B})\mathbf{B}\right] \tag{1.14}$$

$$\mathbf{M} = -2\xi c^2 \left[2(E^2 - c^2B^2)\mathbf{B} - 7(\mathbf{E}\cdot\mathbf{B})\mathbf{E}\right]\,. \tag{1.15}$$

It is evident from eq. (1.3) that the HE QED corrections to the Lagrangian are very small compared to the usual Maxwell terms. This means that only in the presence of strong EM fields will these corrections be non-negligible, as is clear from the cubic field dependence of eq. (1.14) and eq. (1.15) . An immediate and interesting feature of this theory is that for a plane wave, $\mathcal{F} = \mathcal{G} = 0$, meaning that a plane wave is not affected by the HE nonlinearities.

The main objective of this thesis is to develop and optimize an efficient algorithm that can solve this set of nonlinear Maxwell equations whilst incorporated in a massively parallel PIC code. We will now briefly describe how the PIC method works and what are it's main advantages.

## 1.4 PIC method

The PIC method consists of self-consistently solving the equations of motion for all the particles in a discretized spatial grid and it is ideal to study kinetic scale phenomena [13]. Each macro particle (representing an ensemble of real particles) is initialized in the grid. The charge and current densities are then deposited at the edges of the grid-cells, from which the electric and magnetic fields are computed by Maxwell's equations. The fields are interpolated back to the positions of the particles, and these are updated in time by integrating the relativistic Lorentz equation of motion. By modifying the algorithm that solves Maxwell's equations to include QED vacuum fluctuations effects, the PIC method ensures that the single particle dynamics will evolve according to the QED corrected, self-consistent, EM fields.

PIC codes can be used in a variety of contexts traditionally ranging from laser-plasma interaction, to plasma instabilities or even to study Inertial confinement fusion (ICF). On the other hand, the increasing consensus regarding the importance of quantum dynamics in the collective effects of many extreme laser plasma systems has motivated the development of novel numerical tools that couple the multiple scales associated with the problem. Numerical codes that simulate quantum radiation reaction [15–17] and pair production effects [18–22], have already made important predictions in extreme energy density scenarios [22–24]. However, a method to include the effect of vacuum polarization via the creation of virtual pairs, in multi-dimensions and for a broad set of initial conditions, has not been proposed yet. In particular, the ability to fully self-consistently couple the dynamics of relativistic particles with the various ultra-high intensity processes with vacuum polarization effects has not been accomplished.

## 1.5 State of the Art

Vacuum polarization, via the fluctuation of virtual electron-positron pairs, remains to be detected experimentally. In recent years, this topic has motivated great interest in light of the possibility of detecting the dynamics of the quantum vacuum with the development of new laser facilities [25]. A thorough and complete review on the topic of strong field QED in the context of laser interactions by Di Piazza et al. may be found in [26].

The fundamental dimensonless parameter used to describe a laser amplitude, $a_0$, is defined as,

$$a_0 = \frac{eE\lambda_0}{m_e c^2}, \tag{1.16}$$

representing the normalised laser vector potential and also standing for the classical ratio of the energy gained by an electron traversing the laser field E across a laser wavelength $\lambda_0$. For a laser wavelength in $\mu$m, the relation between $a_0$ and the intensity is

$$a_0 = \sqrt{\frac{I_{[W/cm^2]}\lambda^2_{0[\mu m]}}{1.37 \times 10^{18}}} \tag{1.17}$$

Table 1 in [25], compares the expected intensities and respective $a_0$ of existing and future planned laser facilities. In that table a clear emphasis goes to the ELI and Vulcan projects estimated to deliver peak intensities of $10^{25}$ and $10^{23}$ W/cm$^2$ with 1 $\mu$m wavelength radiation corresponding to a $a_0$ of 200 and 5000, respectively. Combining Eq.(1.3) with Eq.(1.16), a useful relation can be derived to obtain the order of the HE corrections compared to unity,

$$\frac{\mathcal{L}_{HE}}{\mathcal{L}_{QED}} = \frac{\xi E^2}{\varepsilon_0} \sim 6 \times 10^{-23}[\mu m]^2 \frac{a_0^2}{\lambda^2_{0[\mu m]}}. \tag{1.18}$$

Eq.(1.18) serves as a quick estimate for the relevance of the HE QED corrections in a given setup.

From a theoretical point of view, diverse setups have been considered in order to explore these corrections. A brief overview shall be given here. An immediate consequence of the modified HE QED Maxwell equations is that in the presence of a strong static field a probe pulse will propagate in vacuum with an index of refraction $n \neq 1$, leading to vacuum birefringence [27]. In particular, a strong static field will induce a very small ellipticity on a probe pulse with initial linear polarization. The PLVAS experiment [28], aims to detect such an effect using a high finesse ($> 2 \times 10^5$) Fabry-Perot cavity and two permanent magnets of 2.5 T. The expected change in the index of refraction of the EM wave propagation in vacuum can be calculated to be $\Delta n^{QED} = 2 \times 10^{-23}$, indeed an extremely small quantity. In 2012, the experiment described in [28], has placed an upper limit on the value of the fundamental coupling constant of the interaction, Eq.(1.3), of $\xi < 2.85 \times 10^{-49}$.

The development of Chirped Pulse Amplification (CPA) has allowed for both the power and the intensity of lasers to grow at a steady rate. This technological development inspired a different approach to detect the effects of vacuum polarization as pointed by Di Piazza et al. [29]. In their analysis the interaction between a linearly polarized x-ray probe beam and a focused, intense standing laser wave was proposed and studied theoretically, giving rise to diffraction effects of the probe pulse and leading once again to both a polarization rotation angle and an induced ellipticity. This setup, however, is far more complex from a theoretical point of view due to finite spot size transverse effects and pulse dynamics. The full complexity can only be captured with numerical simulations thus making this setup very interesting to simulate with the computational tool to be developed in this thesis. Compared to the PLVAS experiment, it is estimated that such a setup can induce an ellipticity 2 orders of magnitude greater [29]. Furthermore, this method is single passage in the sense that it does not require an optical cavity as in PLVAS. A similar experimental setup in the framework of the Helmholtz International Beamline for Extreme Fields (HIBEF), is currently being planned at DESY (Deutsches Elektronen-Synchrotron) [30].

Other exotic setups have also been proposed. In 2000, M.Solijacic and M.Segev [31] showed that in a full 3D setup the HE QED Maxwell equations support nondiffracting spatial radiation solitons that can propagate for very long distances without changing their shape. These solitons present an exciting physical system to be studied in future experiments and clearly a 3D simulation of such a setup would further motivate its implementation. In 2013, B.King, Di Piazza and C.Keitel, proposed a double slit-like experiment where two ultra-intense Gaussian pulses are tightly focused and an (almost) antiparallel probe beam of much wider spot size is counterpropagated leading to a diffraction pattern as shown in Fig. 1.3. This setup was named the Matterless Double Slit [32]. Finally, in ref [33] the existence of new modes generated within a waveguide was shown and this was proposed as a way to detect the QED nonlinearities [33], using technology currently available with state-of-the-art but relatively modest field strengths E $\approx 30$ MV/m.

A few efforts have been aimed at developing the computational tools to self-consistently solve the HE QED Maxwell equations. The first algorithm was developed in 2014 in [34]. In that work, limited to 1D academic setups, it was shown that by interacting two colliding plane wave pulses (with different parameters), higher harmonics of the original probe pulse are generated. An analytic treatment was performed by solving the corresponding wave equation. The numerical method used in this work is one dimensional and involves matrix inversions to solve the modified Maxwell's equations. In principle this method could be extended to higher dimensions. However, not only does

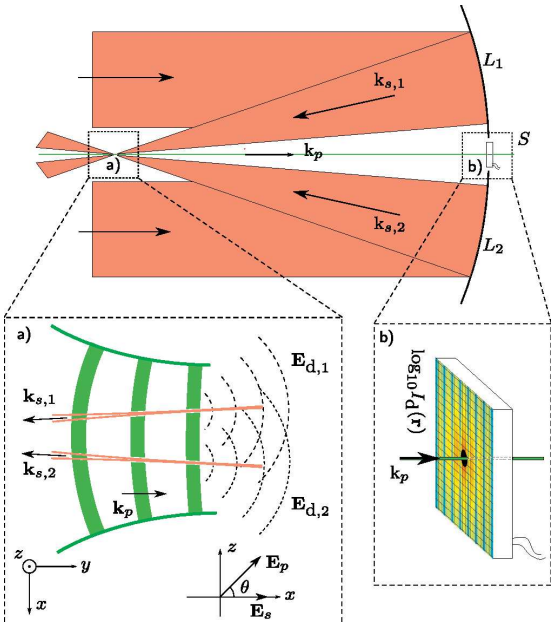


FIGURE 1.3: Matterless double slit setup: lenses L1 and L2, focus two ulta-intense gaussian pulses are counterpropagated at a small and symmetric angle to a probe pulse with a much larger waist leading to an interference pattern in the screen S (b). Figure 1 in original article [32]

the computational demand increase significantly, but also, the nature of this scheme is not adequate within the usual PIC algorithm. The algorithm to be developed in this thesis is an alternative to this method, being an extension of the Yee algorithm which is finite difference in nature. It should be mentioned that, in [34], higher order multi-photon QED corrections are taken into account for the one dimensional setup proposed. These higher order corrections are shown to create a steepening of the probe pulse, an effect named as an "Electromagnetic shock". Although the higher order corrections are not within the scope of this thesis, it is expected that the numerical tool developed in this thesis can be extended in a straightforward manner to include such effects.

A final note regarding an extremely comprehensive and complete review of the Heisenberg-Euler effective action by G.Dunne can be found in [8]. This procedings paper covers the talk given at the conference QFEXT11 commemorating the 75th anniversary of the original HE publication, and it provides an excellent historical review on the topic and a complete overview on the formalism behind the HE QED corrections and how it can be derived in alternative manners such as via the Feynman-Schwinger proper time formulation.

# Chapter 2

# Numerical methods: QED solver

Maxwell's equations modified by the Heisenberg-Euler quantum vacuum corrections constitute a set of nonlinear partial differential equations. The objective of this chapter is to explain the numerical algorithm developed to solve this new set of nonlinear equations numerically in multi-dimensions and for a broad set of initial conditions. The chapter is organized as follows: we start, in section 2.1, with a brief description of the Yee scheme, a finite difference algorithm to solve the set of linear Maxwell's equations. In section 2.2 we present our QED solver as a generalization of the Yee scheme to a nonlinear system and explain each step of the algorithm in detail. In section 2.3 we explain how to perform a numerical stability analysis and generalize the usual linear mode analysis to our nonlinear solver. Finally, in section 2.4 we discuss some of the details of how the algorithm was incorporated in the PIC code Osiris, in an user guide approach.

## 2.1 Maxwell equation solver: Yee Scheme

### 2.1.1 Summary

A standard finite-difference time domain (FDTD) method to solve Maxwell's equations is the Yee Algorithm [35]. The Yee scheme, to be described below, solves simultaneously for both electric and magnetic fields by solving Faraday's and Ampère's law, respectively. The explicit linear dependence of Maxwell's equations on the fields allows the field solver to be centered both in space and time (leap frog scheme), thus providing a robust, second order accurate scheme without the need to solve for simultaneous equations or matrix inversion [36]. Moreover, the efficiency and simplicity of the Yee scheme allows an easy incorporation into numerically parallel PIC codes. Following [36], we will go through the essentials of the Yee scheme, from what it means to discretize a differential equation, to the problems that the algorithm offers when adding the QED corrections to Maxwell's equations.

### 2.1.2 Numerical discretisation of Maxwell equations

The Yee scheme solves the Maxwell's equations using a numerical method called finite-difference time domain (FDTD). The Maxwell's equations in vacuum, can be written in a vector form as

$$\vec{\nabla} \cdot \vec{E} = 0, \tag{2.1a}$$

$$\vec{\nabla} \cdot \vec{B} = 0, \tag{2.1b}$$

$$\vec{\nabla} \times \vec{B} - \frac{1}{c^2}\frac{\partial \vec{E}}{\partial t} = 0, \tag{2.1c}$$

$$\frac{\partial \vec{B}}{\partial t} + \vec{\nabla} \times \vec{E} = 0\,, \tag{2.1d}$$

where eqs.(2.1c-2.1d) are the time-dependent equations dictating the dynamics of the EM fields, whereas the divergence equations, eqs.(2.1a-2.1b) serve as constraints that must be valid at all times. Furthermore, it can be easily shown that eqs.(2.1a-2.1b) are not independent from eqs.(2.1c-2.1d), meaning that by solving the time-dependent equations for the fields in a self-consistent way, the divergence equations will automatically be satisfied for all times. Kane Yee in 1966, derived a set of finite difference equations from eqs.(2.1c-2.1d) to advance the electric and magnetic field in time, respectively. The accuracy and robustness of Yee's algorithm comes from the discretisation of the equations in both time and space combined with the linearity of the equations themselves. The algorithm benefits from second order accuracy due to the fact that the fields are centered both in time and in space, as we shall now explain.

To illustrate this in a one-dimensional example, we start by writing (2.1c-2.1d) in an explicit component form. The one-dimensionality of the problem means that there can only be non-zero derivatives in one spatial direction (in this case, the x-direction), even though the EM fields can be defined in all three Cartesian directions. This yields:

$$\partial_t E_x = 0 \tag{2.2a}$$

$$\partial_t E_y = -c^2 \partial_x B_z \tag{2.2b}$$

$$\partial_t E_z = c^2 \partial_x B_y \tag{2.2c}$$

$$\partial_t B_x = 0 \tag{2.2d}$$

$$\partial_t B_y = \partial_x E_z \tag{2.2e}$$

$$\partial_t B_z = -\partial_x E_y\,, \tag{2.2f}$$

let the indexes $i$ and $n$ denote the spatial and temporal discretised position on the grid respectively. In this notation, an electric field evaluated at position $x = i\Delta x$ and at time $t = n\Delta t$ is denoted by $E(x,t) = E_i^n$. We are now in a position to discretise eqs.(2.2a-2.2f) along the x-direction in one-dimension (meaning there can only be derivatives in the x-direction). The spatial grid on which eqs.(2.2a-2.2f) are discretised is shown in Fig.2.1 where we emphasize the fact that the electric and magnetic fields are not evaluated in the same spatial positions, but instead are displaced by half a cell (from i to i+1/2). This illustrates a crucial feature of the Yee algorithm: the fact that the fields are de-centered in space. The importance of this de-centering can be understood by looking at the system of equations (2.2a-2.2f), where we see that in order to advance a field at a given point (time

derivative term), the spatial derivative of the other field must be computed. However, since calculating a spatial derivative of a field involves evaluating the values of the field at nearby points, the grid disposition shown in Fig.2.1, makes this derivative correctly centered in space as the required fields are only displaced by $\Delta x/2$ to either side. Furthermore, the Yee algorithm is also correctly centered in time meaning that to advance a field from time step n to n+1, using the system (2.2a-2.2f), the spatial derivatives terms are not only shifted in space by $\Delta x/2$, but are also evaluated at the time step $n+1/2$. Again, this shift in time by half a step, of the fields, allows the Yee scheme to be second-order accurate in time and is known as a leap-frog configuration.

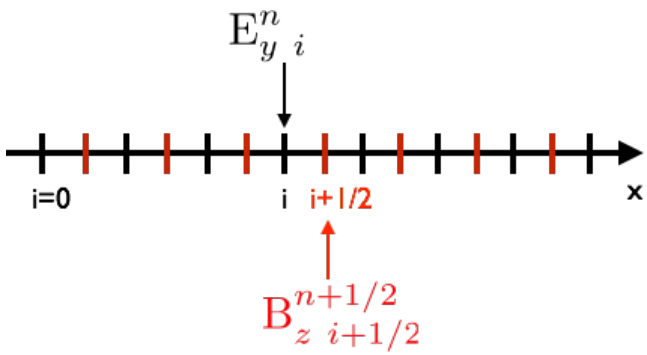


FIGURE 2.1: One dimensional spatial grid illustrating the disposition of the electric and magnetic fields. This illustrates the fact that the both fields are staggered both in space and in time

The concepts just described, become clear when explicitly discretising the system (2.2a-2.2f). As an example, eqs.(2.2b,2.2f) are discretised below. Together, these equations self-consistently account for the temporal evolution of the $E_y$ and $B_z$ field components. This discretisation yields:

$$\frac{E_{y\ i}^{n+1} - E_{y\ i}^{n}}{\Delta t} = -c^2 \left( \frac{B_{z\ i+1/2}^{n+1/2} - B_{z\ i-1/2}^{n+1/2}}{\Delta x} \right), \tag{2.3a}$$

$$\frac{B_{z\ i+1/2}^{n+1/2} - B_{z\ i+1/2}^{n-1/2}}{\Delta t} = -\left( \frac{E_{y\ i+1}^{n} - E_{y\ i}^{n}}{\Delta x} \right). \tag{2.3b}$$

The numerical scheme is finalized by taking eqs.(2.3a-2.3b), and rearranging as follows,

$$E_{y\ i}^{n+1} = E_{y\ i}^{n} - \frac{c^2 \Delta t}{\Delta x} (B_{z\ i+1/2}^{n+1/2} - B_{z\ i-1/2}^{n+1/2}) \tag{2.4a}$$

$$B_{z\ i+1/2}^{n+1/2} = B_{z\ i+1/2}^{n-1/2} - \frac{\Delta t}{\Delta x} (E_{y\ i+1}^{n} - E_{y\ i}^{n}). \tag{2.4b}$$

Eqs.(2.4a,2.4b) are complete in describing the self-consistent evolution of the fields $E_y$ and $B_z$, but also illustrate the concepts of spatial and temporal centering of the fields. This is clear by noting that to evolve any quantity from time step $n$ to $n+1$, this is done by incrementing the field at the same place at time step $n$, by the other field evaluated at time step $n+1/2$ and at adjacent spatial positions. It is straightforward to repeat this process for the equations for the remaining field components and in higher dimensions due to the linearity of the system of equations.

A more complete discussion and generalization of the Yee Scheme in multi-dimensions can be found in chapter 3 of [36], in particular the beautiful relation between how the EM fields are disposed

within a 3D spatial grid cell, and the physical meaning of Maxwell's equations in the differential form.

## 2.2 QED solver: generalized Yee scheme

To solve the QED Maxwell equations, a modified Yee scheme was developed to address the two main difficulties which arise from the nonlinear polarization and magnetization of the vacuum, eqs.(1.14-1.15). The first difficulty is a direct consequence of the loss of linearity in the modified Maxwell's equations. To understand this difficulty, we recover the one-dimensional example from sec.2.1 and re-write eqs.(2.3a,2.3b) including the nonlinear quantum vacuum terms

$$\frac{E_{y\,i}^{n+1} - E_{y\,i}^{n}}{\Delta t} + \frac{P_{y\,i}^{n+1} - P_{y\,i}^{n}}{\Delta t} = -c^2 \left( \frac{B_{z\,i+1/2}^{n+1/2} - B_{z\,i-1/2}^{n+1/2}}{\Delta x} \right) + \frac{1}{\mu_0} \left( \frac{M_{z\,i+1/2}^{n+1/2} - M_{z\,i-1/2}^{n+1/2}}{\Delta x} \right) \tag{2.5a}$$

$$\frac{B_{z\,i+1/2}^{n+1/2} - B_{z\,i+1/2}^{n-1/2}}{\Delta t} = - \left( \frac{E_{y\,i+1}^{n} - E_{y\,i}^{n}}{\Delta x} \right). \tag{2.5b}$$

To complete the numerical algorithm in a self-consistent way including the vacuum polarization and magnetization, we would have to rearrange eqs.(2.5a-2.5b) to isolate the terms for $E^{n+1}$ and $B^{n+1/2}$, respectively. However it is clear that this is no longer possible as the polarization term evaluated at time step $n+1$ is a nonlinear function of all EM field components at $n+1$, which are exactly the quantities we wish to compute. This example illustrates how the nonlinearity introduced in Maxwell's equations due to the HE corrections, no longer allows the use of the Yee algorithm to advance the EM fields in time in a straightforward manner.

The second difficulty that arises when attempting to apply the Yee algorithm to the Maxwell's equations corrected by the HE QED terms, is the fact that the nonlinear polarization and magnetization terms depend on the EM invariants $E^2 - B^2$ and $\vec{E} \cdot \vec{B}$. Both these quantities require the knowledge of all the fields in every grid position as opposed to the usual spatially staggered field configuration described in the previous section. This is a significant obstacle regarding the essence of the Yee scheme as the algorithm may no longer be correctly spatially centered.

The two main problems that arise when attempting to apply the Yee scheme to the nonlinear set of QED Maxwell's equations are therefore the fact that the modified Ampère's law requires the knowledge of future fields and the need to know the value of all field components in every grid position to calculate the polarization and magnetization of the vacuum. The former difficulty served as the main motivation to develop our modified Yee scheme. The steps of the algorithm we propose are illustrated in Fig.2.2 and shall now be described for a time step $\Delta t$:

- we begin by advancing the fields using the standard Yee scheme (i.e. without accounting for the polarization and magnetization of the vacuum). This setup allows us to obtain predicted quantities for the values of the fields at the new time. This approach is based on the standard technique of the predictor-corrector method, where the linear Maxwell equations are solved as the zeroth order solution to the fields;

- the predicted field values are then interpolated at all spatial grid points using a cubic spline interpolation method thus allowing to calculate quantities such as the EM invariants and respective polarization and magnetization of the vacuum, to lowest order;
- the polarization and magnetization are then used to advance the electric field via the modified Ampère's law;
- the convergence loop re-injects this new electric field value back into the polarization and magnetization source terms to refine these quantities and re-calculate the electric field iteratively. This loop is reiterated until the electric converges to a value within the desired accuracy;
- after convergence is achieved, Faraday's law is advanced, identically to the linear Yee scheme, benefiting from the fact that the electric field values being used are self-consistent with the QED corrections.

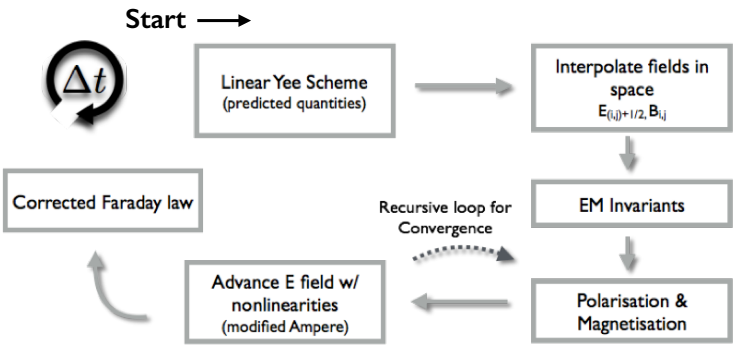


FIGURE 2.2: Full loop of the modified Yee scheme

It must be emphasized that this method is only valid as long as the effects of the polarization and magnetization of the medium are small compared to the non-perturbed propagation of the fields given as solutions to Maxwell's equations in classical vacuum. This condition is automatically satisfied for realistic values of electromagnetic fields available in current, or near future, technology. In this regime, the QED theory is valid since the Schwinger field, above which the production of real electron-positron pairs is possible, corresponds to an electric field of $E_{Sch} \sim 10^{18}$V/m, whereas ambitious laser facilities aim to push available intensities to the $10^{23} - 10^{24}$ W/cm$^2$ ($E \sim 10^{15}$V/m) range. The order of the $\xi$ parameter in eqs.(1.3,1.14,1.15) clearly helps to ensure the validity of the method. Therefore, this scheme highly benefits from the fact that the nonlinear QED corrections of the vacuum are perturbative in nature. The convergence loop can be seen as a Born-like series since for every re-insertion of the fields back into the nonlinear source term, there is a gain in accuracy of one order in the expansion parameter to the result. The algorithm proposed here solves Ampère's law by treating the nonlinear corrections as a source term, in an iterative manner,

$$\vec{\nabla} \times \vec{B} - \partial_t \vec{E} = \vec{S}_{NL}[E, B], \tag{2.6}$$

where $\vec{S}_{NL} = \vec{\nabla} \times \vec{M} + \partial_t \vec{P}$. From this discussion and eq.(2.6), we can conclude that this generalization of the Yee scheme can be extended beyond the framework of QED corrections to the vacuum as

it is valid to solve Maxwell's equations in any nonlinear medium provided that the polarization and magnetization are given and that their order is such that they can be treated as a perturbation. This possible generalization enhances the range of applicability of our algorithm. Furthermore, the inclusion of a current in the algorithm ($J \neq 0$ in Ampère's law) can be done, both within a PIC framework or for a macroscopic field dependent current by including the current term in the initial standard Yee scheme loop where the predictor quantities are computed. This is another key feature regarding the ability to couple our proposed generalized Yee solver to the PIC framework.

### 2.2.1 Interpolation of the fields

The algorithm requires that all fields are calculated at the same spatial positions. When considering the spatial interpolation of the self-consistent fields given by the Yee Algorithm we found a clear asymmetry between interpolating the electric field at the magnetic field position or vice-versa in terms of the precision of the EM invariant $E^2 - B^2$ for both cases. Since a plane wave is a trivial solution of the QED Maxwell equations, the invariants calculated in the simulation should be identically zero [37]. Figure 2.3 shows the distribution of the EM fields within a two-dimensional Yee grid cell. We found that all the standard interpolation schemes yield invariants with much greater precision at the lower left corner of the cell compared to the other positions. This difference in precision was found to be of two orders of magnitude when tested for a plane wave in 1D, which can affect the stability and precision of the code. The reason for this artifact is due to the way that the fields are initialized within the simulation domain. In particular, the fact that the electric and magnetic fields must be initialized with a shift both in space and time, creates an asymmetry between interpolating a field to the corresponding position of the other field, even if this interpolation is done in a centered manner. The solution we have adopted to address this problem is to calculate all the fields at the cell corner where the invariants are known to be of higher precision. For instance, the $B_z$ component at the left corner of the cell becomes

$$B_{z\ i,j} = \mathcal{I}(B_{z\ i+\frac{1}{2},j+\frac{1}{2}}, B_{z\ i-\frac{1}{2},j+\frac{1}{2}}, B_{z\ i+\frac{1}{2},j-\frac{1}{2}}, B_{z\ i-\frac{1}{2},j-\frac{1}{2}}),$$

where $\mathcal{I}$ is an interpolation function. Once all fields are calculated at the $(i, j)$ positions, we can compute the invariants at these positions and then re-interpolate these invariants directly to the other grid cell points in a similar fashion. The correct calculation of the EM invariants is necessary in order to evaluate the nonlinear polarization and magnetization of the vacuum via eqs.(1.14-1.15)

Having proposed a generalized Yee algorithm and explained in detail the algorithm along with its subtleties, we now move on to analyse the numerical stability properties of the algorithm. The motivation in performing this study is to investigate whether the algorithm is ultimately stable under the same conditions as the linear Yee algorithm , and if not, what parameters of the simulation can be used to control the stability in order the ensure the results obtained are physically meaningful in the desired regimes.

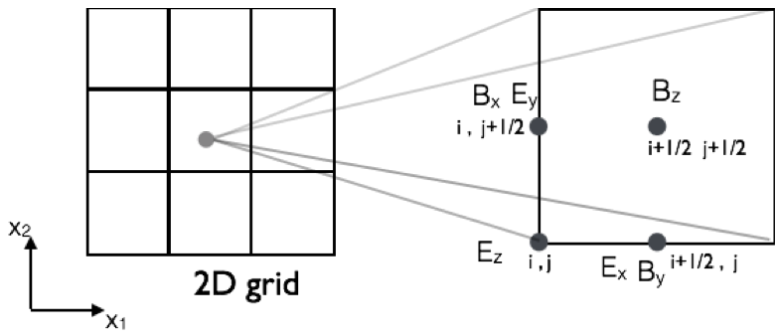


FIGURE 2.3: Two-dimensional Yee grid cell

## 2.3 Algorithm Stability: linear and nonlinear analysis

The method adopted to study the numerical stability of the QED polarization solver follows the standard mode analysis [36]. This method involves linearizing the discretized set of equations using a Fourier mode analysis. For the QED corrected Maxwell's equations, this amounts to introducing the following dependence for the EM fields

$$E = \tilde{E}e^{-j\omega t+jkx} \tag{2.7}$$

$$B = \tilde{B}e^{-j\omega t+jkx}, \tag{2.8}$$

where $\tilde{E}$ and $\tilde{B}$, represent the amplitudes of a given $\omega, k$ pair that satisfy the appropriate dispersion relation, to be identified. This representation of the fields can be discretized on a one-dimensional staggered grid, using the notation from 2.1, yielding,

$$E_i^n = \tilde{E}e^{-j\omega n\Delta t+jki\Delta x} \tag{2.9}$$

$$B_{i+1/2}^{n+1/2} = \tilde{B}e^{-j\omega(n+1/2)\Delta t+jk(i+1/2)\Delta x}, \tag{2.10}$$

Inserting eq.(2.9) and eq.(2.10) into the linear set of Maxwell's equations yields the numerical dispersion relation that is to be expected for a plane wave propagating on a grid with spatial and temporal resolution $\Delta x$ and $\Delta t$, respectively, is [36]

$$\omega_0 = \frac{1}{\Delta t}\arccos\left(1+\left(\frac{c\Delta t}{\Delta x}\right)^2(\cos(k\Delta x)-1)\right). \tag{2.11}$$

A notable case is when $\Delta t = \Delta x/c$ for which eq.(2.11) reduces to the EM dispersion relation for a plane wave in vacuum, $\omega_0 = ck$. To study the stability of the new set of QED-corrected Maxwell's equations using this method, a self-consistent numerical dispersion relation was derived. Due to the non-linearity of the equations, the new dispersion relation can be written as

$$\left(\frac{c\Delta t}{\Delta x}\right)^2\sin\left(\frac{k\Delta x}{2}\right)^2 - \sin\left(\frac{\omega\Delta t}{2}\right)^2 = \xi E_0^2 F_{NL}(\omega, k, \Delta x, \Delta t), \tag{2.12}$$

where $E_0$ is the amplitude of the wave and $F_{NL}$ is a nonlinear function of $\omega$, $k$, and the spatial and temporal steps. In the classical limit $\xi \to 0$ the RHS goes to zero and the dispersion relation reduces

to eq.(2.11). The explicit form of the nonlinear function $\mathrm{F}_{NL}$ is given by

$$\mathrm{F}_{NL} = \mathrm{Inv}(k,\omega) exp(-2j\phi) \left[ \left(\frac{\Delta t}{\Delta x}\right)^2 \sin\left(\frac{3\Delta x k}{2}\right) \sin\left(\frac{\Delta x k}{2}\right) - \sin\left(\frac{3\Delta t \omega}{2}\right) \sin\left(\frac{\Delta t \omega}{2}\right) \right] \tag{2.13}$$

Where $\phi = -(n+1/2)\omega\Delta t + k\Delta x i$ and $\mathrm{Inv}(k,\omega)$ represents the Fourier amplitude defined by $\mathrm{Inv}(k,\omega) = (E^2 - B^2)(k,\omega)$. A numerical plane wave propagating via our QED solver will therefore obey eq.(2.12).

Eq.(2.13) explicitly shows a great difficulty that arises from attempting to perform a linear numerical stability analysis on a nonlinear system of equations: the fact that the dispersion relation depends on both spatial and temporal grid indices $i$ and $n$, respectively. This, combined with the exponential function with imaginary argument, appears to show that the dispersion relation of an initialised plane wave will depend on the spatial and temporal positions on the grid. This represents a clear sign of instability and chaotic dynamics. On the other hand, the fact that the left-hand side of eq.(2.12) is a small correction to the linear dispersion relation, hints that this nonlinear behaviour discussed will only be a higher order correction. To make the analysis possible, we assume that the dispersion relation cannot depend on the spatial and temporal indices and therefore we perform the following replacement in eq.(2.13),

$$exp(-2j\phi) \rightarrow \frac{1}{\sqrt{2}}(1+j) \tag{2.14}$$

This approximation will later be verified by the results obtained. However, the reasoning behind our approximation is that the exponential term creates a unpredictable phase that slightly modifies the amplitude of the corrections to the linear dispersion relation with a factor that is varying in time and space. By taking this approximation, we are essentially taking the upper limit of this random phase, meaning that we are still capturing the important aspects of the numerical stability of the system.

To continue the analysis, we have to calculate the value of $\mathrm{Inv}(k,\omega)$ for the numerical plane wave introduced in the system. For a numerical plane wave the EM invariant $\vec{E}\cdot\vec{B}$ is identically zero, whereas the invariant $E^2 - B^2$ will not vanish identically due to finite spatial resolution and the fact that the fields must be interpolated in space to evaluate the invariants, as already discussed above. Therefore, the amplitude of this EM invariant depends on the interpolation method and grid resolution. We calculate this dependence by evaluating $E^2 - B^2$ at a given grid point, taking into account that a correct centering in space implies one of the fields must be interpolated to the position of the other. Interpolating the B field using linear interpolation is formally equivalent to computing

$$(E^2 - B^2)_i^n = E_i^2 - B_i^2 = E_i^2 - \left(\frac{B_{i+1/2} - B_{i-1/2}}{2}\right) \tag{2.15}$$

Having evaluated this EM invariant on a grid position using correctly centered fields, the final step is to substitute the amplitudes eqs.(2.9-2.10) and replace the magnetic field amplitude using Faraday's law. After some algebra this finally yields

$$\mathrm{Inv}(k,\omega) = E_0^2 \left[ 1 - \frac{\sin^2(k\Delta x/2)}{\sin^2(\omega\Delta t/2)} \cos^2\left(\frac{k\Delta x}{2}\right) \right]. \tag{2.16}$$

This expression was compared to the results extracted from one-dimensional simulations. The simulation setup comprised of a 1D periodic box initialised with a plane wave of amplitude $E_0$, such that the wavelength of the wave is a multiple of the box size. We repeated this simulation using different initial wavelengths corresponding to different seeded $k$ modes. Figure **??** shows a comparison between eq.(2.16) and simulations with several seeded $k$ modes and with $\xi E_0^2 = 10^{-4}$ , $\Delta t = 0.98\Delta x$ and $\Delta x = \pi/100$.

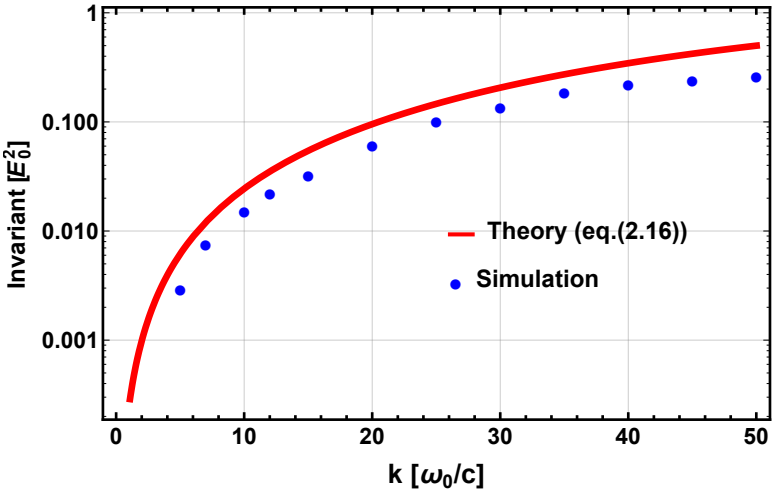


FIGURE 2.4: Amplitude of EM invariant $E^2 - B^2$ as a function of the seeded k-mode for a resolution $\Delta x = \pi/100$, $\Delta t = 0.98\Delta x$ and $\xi E_0^2 = 10^{-4}$. Simulation results in blue are compared to eq.2.16 in red.

The simulation points agree with the trend presented by the theoretical curve. This result shows that eq.(2.16) provides an upper bound to the interpolation error when seeding a particular $k$ mode. In particular, the results show that for higher wave numbers, up to the resolution limit, the order of magnitude of the invariant amplitude increases, tending towards unity. One shall therefore limit the simulations to low $k$ modes in order to insure the smallness of the invariants.

The stability of the QED Yee solver, i.e., the nonlinear dispersion relation, eq.(2.12) was solved using three methods: a numerical solution, an analytical solution through the linearization of the system via the ansatz $\omega = \omega_0 + \delta\omega$ with $\delta\omega \ll \omega_0$, and finally by estimating the growth rate of the maximum mode allowed by the grid resolution i.e. $k\Delta x = \pi$. The results are shown in Fig. 2.5 for simulations performed with a grid resolution of $\Delta x = 0.0314$, $\Delta t = 0.98\Delta x$ and $\xi E_0^2 = 10^{-4}$.

One can verify in Fig.2.5 that the analytic solution is in excellent agreement with the numerical integration. The maximum growth rate is given by

$$\mathrm{Im}(\delta\omega_{max}) \simeq \frac{2\xi E_0^2\sqrt{8\varepsilon}}{\Delta t}, \tag{2.17}$$

where $\varepsilon = 1 - \frac{\Delta t}{\Delta x}$. The maximum growth rate predicted theoretically serves therefore as an accurate rule-of-thumb criteria to understand how unstable a given simulation setup may be. Finally we took the solution of the perturbative expansion and studied the limit for small $k$ values, which yields

$$\lim_{k\Delta x \to 0} \mathrm{Im}(\delta\omega) = \frac{1}{4}\frac{\xi E_0^2 (k\Delta x)^5}{\Delta x}. \tag{2.18}$$

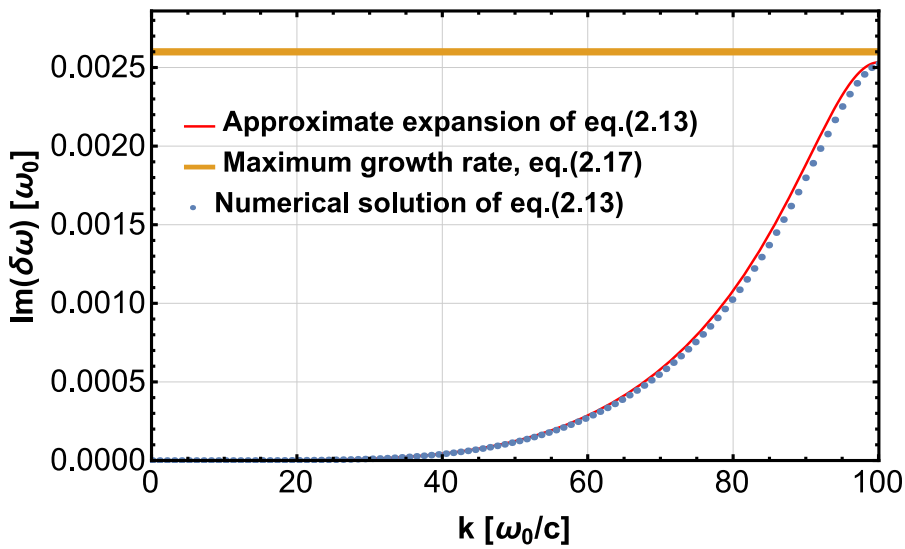


FIGURE 2.5: Imaginary part of solution of nonlinear dispersion relation, eq.(2.12), as a function of k-mode, calculated using three different methods. Simulation parameters used were $\Delta x = 0.0314$, $\Delta t = 0.98\Delta x$ and $\xi E_0^2 = 10^{-4}$.

Eq.(2.18) suggests that the smallest $k$ modes will be ultimately stable as, not only does the growth rate scale with the small quantity $\xi E_0^2$, but also due to the power law applied to the small value of $k\Delta x$. This is an important result since, in principle, the low k modes, for a given grid resolution, are those that will be seeded for a simulation setup.

These theoretical predictions were compared with one-dimensional simulations by extracting the growth rate of a given $k$ mode in the simulation domain. The process to extract this maximum growth rate was the following: after completing the simulation with a seeded $k$ mode, we applied a diagnostic that shows the amplitude of each $k$ mode as a function of time. An example this diagnostic for a given simulation is shown in Fig-.2.6 where we can see that the higher k-modes are those that have a more dynamic growth after a certain critical time. In Fig-2.6 we can also see a horizontal line at a low $k$ value that corresponds to the seeded mode.

To extract the maximum simulation growth rate, we perform a horizontal line-out by choosing the $k$ that achieves the highest amplitude. In Fig.2.6 this happens for $k = 83$, and the corresponding line-out is shown in Fig.2.7. In Fig.2.7, we observe a transient period of no growth in the fields before the onset of the linear growth phase, after which there is a period of linear growth. Finally, once the amplitude of the unstable k modes become comparable to that of the initial seeded mode, there is a blow-up of the fields and consequently and increase in EM energy at a rate far greater than an exponential. Finally, to measure the maximum growth for this simulation one must take the gradient of linear section in Fig.2.7.

The results for the maximum growth rate extracted are shown in Fig.2.8. The growth rate was extracted from the Fourier spectrum of the simulations for different values of $\xi E_0^2$. Figure 2.8 shows a close agreement between the maximum growth rates extracted and eq.(2.8). Our theoretical analysis shows that the growth rate of the most unstable mode scales linearly with $\xi E_0^2$. Furthermore, we

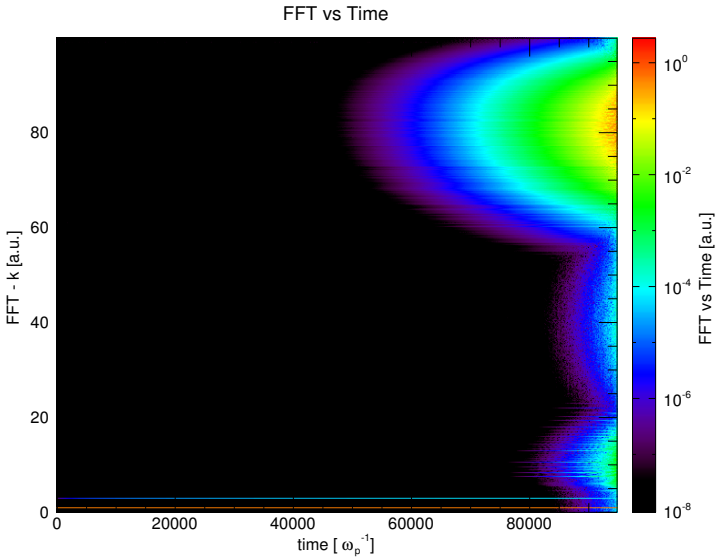


FIGURE 2.6: Amplitude of each k mode as a function of time.

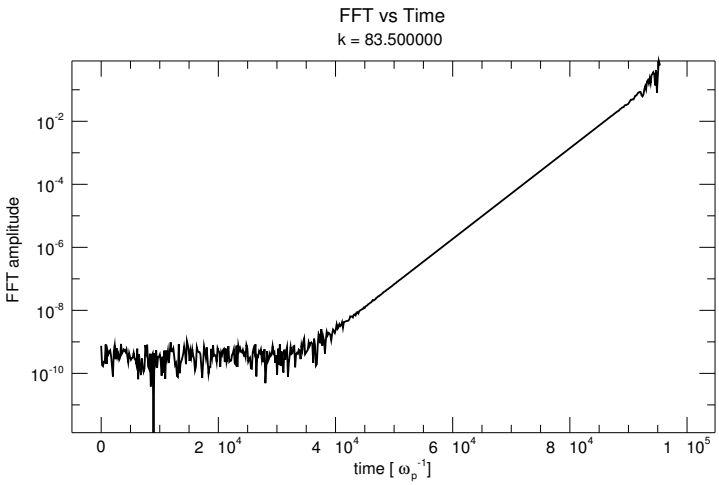


FIGURE 2.7: Line-out at $k = 83$ from Figure 2.6 to extract the temporal evolution of the fastest growing k-mode.

performed simulations under the same conditions, varying only the seeded $k$ mode and verified that this does not affect the growth rate of the most unstable high $k$ modes. Instead, it is the amplitude of the seeded mode that affects the growth rate of the higher $k$ modes by nonlinear coupling.

The transient time between the onset of the linear growth phase and the blowup can be estimated by assuming this blow-up occurs once the amplitude of the fastest growing $k$-modes $\delta\tilde{E}$ (initially this amplitude is at the numerical noise level, and can be measured from the initial spectrum of the fields in the simulation), become of the order of the initial seed amplitude. To estimate this time, we

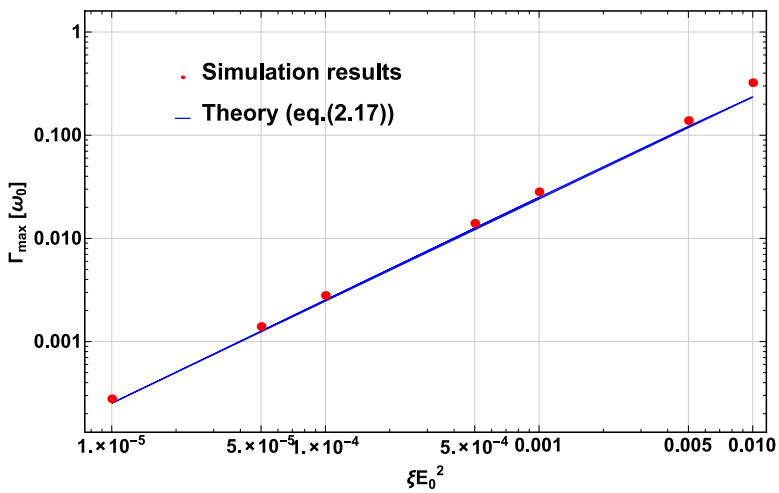


FIGURE 2.8: Comparison between maximum growth rate extracted from simulation with theoretical prediction calculated form the nonlinear dispersion relation. The Figure shows how this growth rate varies as a function of $\xi E_0^2$, which measures the importance of the nonlinear quantum vacuum corrections. The simulation parameters used were $\Delta x = 0.0314, \Delta t = 0.98\Delta x$ and a seeded $k_{\text{seed}} = 1$.

assume the electric field can be decomposed into

$$E(x,t) = E_0 + \delta\tilde{E}e^{\Gamma_k t} \tag{2.19}$$

we define $t_{\text{blow}}$ when$E_0 \sim \delta\tilde{E}e^{\Gamma_k t}$

$$t_{\text{blow}} \sim \frac{1}{\Gamma_k}\log\left(\frac{E_0}{\delta\tilde{E}}\right) \tag{2.20}$$

This expression can be simplified by inserting the upper bound for the growth rate eq.(2.17). This yields

$$t_{\text{blow}} \sim \frac{\Delta t}{\sqrt{\varepsilon}}\frac{1}{\xi E_0^2}\log\left(\frac{E_0}{\delta\tilde{E}}\right). \tag{2.21}$$

Note that to estimate this time the initial amplitude $\delta\tilde{E}$ must be extracted from an early time step of the simulation. For realistic values of $\xi E_0^2$, this time is far greater than any simulation setup one may wish to perform.

Finally note that our analysis seems to breakdown for the magic time step, by predicting that in this case eq(2.12) reduces identically to zero. This apparent inconsistency stems from the fact that a plane wave should not polarize the vacuum, not even the numerical vacuum making it natural that when we attempt to perform a linearization of a system that should yield vanishing EM invariants, this limit should be recovered. However, due to interpolation errors and finite resolution effects, the EM invariant $E^2 - B^2$ is not identically zero, from a numerical point of view. Finally, despite the inconsistency of our theoretical analysis in this limit, the results obtained from the simulations correctly match the theoretical predictions using a linear mode analysis.

## 2.4 Osiris implementation

The final section of this chapter is aimed at explaining the structure of the numerical algorithm we developed within the OSIRIS source code. All sections of the added code were written in Fortran90 language. This section is divided in three sub-sections: we start by explaining what are the inputs that the new algorithm requires and therefore what must be changed in the structure of the input deck. We then state the new functions that were introduced and where these functions are called within the code. Finally, we explain the diagnostics that were added to export useful auxiliary quantities such as the invariants, polarization and magnetization of the vacuum.

### 2.4.1 Code inputs

The fundamental coupling parameter of the theory $\xi$ given by eq.(1.3) determines the order of the quantum corrections from the HE Lagrangian and completely defines the effective 4-photon coupling. In particular, in the classical limit ($\hbar \to 0$) it tends to zero. This parameter must be given as an input parameter of the code within the global simulation parameters section of the input deck, the initialization is done as shown in the following example:

```
!----------global simulation parameters----------
simulation
{
omega_p0 = 1.88346d15,
csi = 1.0d-11,
}
```

Note, however that since this parameter has units of inverse of square of an electric field $E^{-2}$, the $\xi$ parameter introduced must be properly normalized. The natural quantity to normalize EM within a scenario involving the quantum vacuum, is the Schwinger critical field. Therefore the way chosen to normalize the $\xi$ parameter within our code is

$$\tilde{\xi} = \xi \left( \frac{E_s}{\tilde{E_s}} \right)^2 = \frac{2.6 \times 10^{-4}}{\tilde{E_s}^2} \tag{2.22}$$

Where $\tilde{E_s}$ is the Schwinger field normalized in the standard way for Osiris, ie: normalized using the characteristic frequency of the simulation. This normalization is given by

$$\tilde{E_s} = \frac{eE_s}{m_e \omega_0 c}. \tag{2.23}$$

### 2.4.2 Structure of solver

Taking into account the scheme of the algorithm presented in Fig.2.2, the main additions to the solver can be found in the os-emf-solver.f90 file. In this module, the advance-emf subroutine incorporates the crucial functions added to the solver. In this subroutine first the fields are evolved using the linear yee solver (or any other solver present in Osiris) in order to calculate the classical fields without the QED corrections. Having these fields with the appropriate boundary conditions, we interpolate the

EM fields to all grid position using the qed-interp subroutine. In the latest version of the code, the interpolating functions can be found in the os-emf-gridcenter.f90 file. Following the interpolations of the fields, the sub-routines that calculate the EM invariants and the nonlinear polarization and mangnetization of the vacuum are called. Finally, the final portion of the solver calls the functions nl-select-dedt and nl-select-dbdt, to calculate the electric and magnetic fields at the new time-step already taking into account the corrections of the quantum vacuum. The section of the code within the advance-emf subroutine where these functions are called is shown below for illustrtive purposes:

```
! Advance B half time step
 call dbdt( this, dt_b )
! call update_boundary_b( this, step = 1 )

 call copyb(this)
 call copymag(this)

 ! Advance E one full time step
 call dedt( this, jay, charge, dt_e, no_co )
 call update_boundary_e( this )

 ! Advance B another half time step
 call dbdt( this, dt_b )
 call update_boundary_b( this, step = 2 )

 call qed_interp(this, no_co)
 call invariant(this, no_co)
 call define_pm(this,csi, no_co)

 call select_nldedt(this, csi, dt_e,dt, no_co)
 call update_boundary_e( this)

 call select_nldbdt(this, dt_b, no_co)
 call update_boundary_b( this, step = 2 )
```

### 2.4.3 Diagnostics developed

Besides the post-processing diagnostics developed for specific scenarios and purposes, we added some diagnostics within the Osiris framework in order to visualze the new quantities that are useful within the QED solver. These include the EM invariants, the polarization and magnetization of the vacuum, as well as the EM fields now evaluated at all grid positions. To identify a field within a given Yee grid cell position we defined the following convention illustrated in Fig.2.9, where an index 00, 01, 10, 11 was assigned to each grid position. Therefore, in this convention, the diagnostic for the polarization at the center of a cell is called by "P-11", for example.

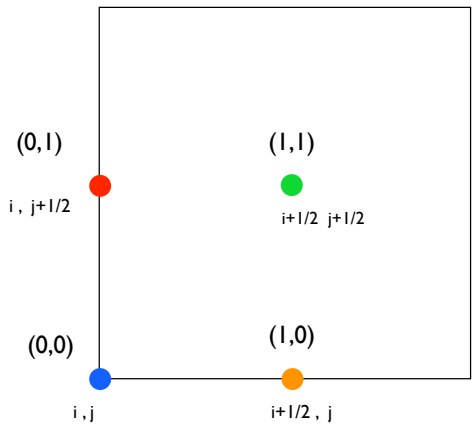


FIGURE 2.9: Two-dimensional Yee grid cell combined with respective convention adopted for indexing within the code

# Chapter 3

# Simulation results and code benchmarks

The algorithm proposed in the previous chapter comes as a novelty to both the computational physics community but specially to the strong field QED community. The objective of this chapter is to benchmark the numerical algorithm and show that it can be a reliable tool in multi-dimensional setups. The chapter is structured as follows: we start with one-dimensional setups to explore the mathematical techniques behind the birefringence of the vacuum and high harmonic generation, whilst proving that the algorithm implemented delivers correct physical results. After performing the one-dimensional benchmark we present a two-dimensional birefringence example to justify that the generalization of the algorithm to higher dimensions is accurate. Finally, we show how robust and useful the algorithm can be in two-dimensional scenarios by considering the counter-propagation and oblique collision of two laser pulses focused on the same point, showing results that would otherwise be unattainable without a self-consistent numerical analysis.

## 3.1 1D Results

A thorough benchmark of the functionality and robustness of the algorithm may only be obtained by comparing simulation results with analytical results in 1D simplified cases. One dimensional scenarios provide opportunities to test the code against analytical predictions. The two cases we exploit here are the vacuum birefringence in the presence of a strong static field and counter propagating plane waves. Whilst the first case is well studied in the literature [38, 39], the second case requires a finer analytical work, yielding nevertheless the well known result of generation of higher harmonics due to the nonlinear interaction as shown in [34, 40, 41] in different setups and physical regimes. The value of the parameter in normalized units for the simulations in this section is $\xi \sim 1 \times 10^{-15}$. However, the simulations here presented were performed with increased values of the $\xi$ parameter in order to better illustrate the method proposed here. This does not alter the physical relevance of the results as we shall show. Rather, this is simply a re-scaling of a constant in order to highlight the effects in a clearer way. In all the results presented in this section, the units were normalized to the characteristic laser frequency, $\omega_0$ and wave number, $k_0$. The normalizations are thus $t \to \omega_0 t$ and $x \to k_0 x$. These normalizations of space and time define the normalizations used for the fields, i.e: $E \to eE/mc\omega_0$ and $B \to eB/mc\omega_0$.

### 3.1.1 Vacuum Birefringence

The optical property of a change in refractive index of a material according to the polarization and propagation direction of the incoming light is called birefringence. If the optical medium in question is the vacuum, then this effect is refered to as vacuum birefringence. The birefringence of the vacuum is a thoroughly studied setup that stems from the nonlinear character of the polarisation of the vacuum and is therefore of great experimental interest [28]. A one dimensional wave packet traveling in the presence of a strong static field will experience a modified refractive index of the vacuum due to the HE corrections, as we shall now show. The physical interpretation for the modified refractive index of the vacuum is that the electron-positron fluctuations induced by the nonlinear coupling between the static field and the traveling wave pulse, act as an effective medium that will alter the phase velocity of the pulse. We will start with the example of a one dimensional pulse traveling in the region where a strong static electric field exists.

To obtain an approximate analytical expression, one assumes that the strong background field remains unperturbed by the nonlinearities. This motivates the following ansatz for the solution of modified Maxwell's equations

$$\vec{E} = \vec{E}_p(x,t) + \vec{E}_s, \tag{3.1}$$

where $E_p$ and $E_s$ represent the electromagnetic pulse and the static fields, respectively and $E_p \ll E_s$. Without loss of generality, we align the strong static field along the $y$ direction and study two cases: where the pulses' polarization is parallel or perpendicular to the strong static field. Starting with the parallel case we obtain the following initial field setup:

$$E_y = E_p(x,t) + E_s, \tag{3.2}$$

$$B_z = B_p(x,t), \tag{3.3}$$

such that $E_p$ and $B_p$ are self-consistently related via the Faraday law. Inserting this setup into the EM invariants and calculating the polarization and magnetization the vacuum yields (without any approximations)

$$P_y = 2\xi(E_s^3 + 3E_s^2 E_p + 2E_s E_p^2), \tag{3.4}$$

$$M_z = -2\xi(E_s^2 B_p + 2E_s B_p E_p). \tag{3.5}$$

We perform an ordering of the system by neglecting terms of order $O(E_s E_p^2)$. Furthermore, despite the fact that the $\xi E_s^3$ term clearly dominates in eq.(3.4), it is a constant by construction and will therefore vanish when inserted into Ampère's law, eq.(1.10), due to the differential operator applied to the polarization. We emphasize the fact that what is physically relevent is the derivatives of the polarization and magnetization of the vacuum. The relevant components of Ampère's law and Faraday equation are

$$\partial_t E_y = -\partial_x B_z - \partial_t P_y + \partial_x M_z \ , \tag{3.6a}$$

$$\partial_t B_z = -\partial_x E_y \ , \tag{3.6b}$$

coupled with eqs.(3.4-3.5). Inserting the vacuum polarization and magnetization derived above and

obtaining the wave-equation for one of the fields via the standard technique (differentiating each equation with respect to time/space and combining them) yields,

$$(1 + 6\xi E_s^2)\partial_t^2 E_p - (1 + 2\xi E_s^2)\partial_x^2 E_p = 0\,, \tag{3.7}$$

which is in the form of a wave equation with a refractive index given by

$$n_{\parallel} = \left(\frac{1 + 6\xi E_s^2}{1 + 2\xi E_s^2}\right)^{1/2} \approx 1 + 2\xi E_s^2. \tag{3.8}$$

We obtained the modification to the refractive index of the vacuum due to the coupling between the strong static field and the probe pulse. Notice that in the classical limit, $\xi \to 0$, we obtain the expected result of unity refractive index. This expression is in agreement with the literature where this effect was first derived in the context of exploring the birefringence of the quantum vacuum from a covariant point of view [39]. This method can be repeated in the case where the polarization of the pulse is perpendicular to the static electric field, yielding

$$n_{\perp} = \left(\frac{1 + 2\xi E_s^2}{1 - 5\xi E_s^2}\right)^{1/2} \approx 1 + \frac{7}{2}\xi E_s^2, \tag{3.9}$$

Notice that the product $\xi E_s^2$ appears as a relevant quantity. This is a recurring property of several setups. It must be ensured that this product is a small quantity, both for the validity of the theoretical framework but also from the algorithm point of view. This quantity controls whether the corrections to the unperturbed fields are small or not, a crucial feature for the stability of algorithm as, already discussed. As pointed out in [39], this procedure can be repeated in the case of a strong magnetic field rather than and electric field. Taking the parallel and perpendicular direction again to be defined with respect to the polarization of the probe pulse, we obtain the following refractive indexes for a probe pulse propagating in the presence of a strong static magnetic field, $B_s$:

$$n_{\parallel} = \left(\frac{1 + 2\xi B_s^2}{1 - 5\xi B_s^2}\right)^{1/2} \approx 1 + \frac{7}{2}\xi B_s^2, \tag{3.10}$$

$$n_{\perp} = \left(\frac{1 + 6\xi B_s^2}{1 + 2\xi B_s^2}\right)^{1/2} \approx 1 + 2\xi B_s^2, \tag{3.11}$$

which are exactly the sme result compared with the static electric field case with the role of the two modes interchanged.

The resultx obtained present an opportunity to test the accuracy of the code in a simple one dimensional setup where the only physical phenomena present is the change in the phase velocity of a pulse in the presence of a strong static field. The simulation setup consists of a strong static electric field of $10^{-3}E_{Sch}$, where $E_{Sch}$ is the Schwinger critical field, aligned along the $y$ direction and a Gaussian EM pulse propagating in the $x$ direction and polarized in the $y - z$ plane. The central wavelength of the EM Gaussian pulse is 1 $\mu$m and its duration 5.6 fs. Figure 3.1 shows two simulations for the same pulse after propagating once through a periodic box. In one case the propagation is in the classical vacuum, whereas the QED solver is used in the other. Qualitatively, the difference in propagation distance and the reduced electric field amplitude is consistent with the theory of a

pulse traveling in a refractive medium. To test the accuracy of the algorithm this same setup was run for different values of the product $\xi E_s^2$ for both the parallel and perpendicular setup. We chose to perform our analysis as a function of the product $\xi E_s^2$ as not only the theoretical expressions are proportional to this result but also to test if the algorithm is able to reproduce consistent results for several scales of this parameter, thus proving the algorithm robustness and the correctness of using increased values of the quantum coupling parameter $\xi$. The difference in phase velocity between the two pulses allows to extract directly the quantum vacuum refractive indexes and to compare with the analytical predictions of Eq.(3.8)-Eq.(3.9). The results of this comparison are shown in Fig. 3.2(a) and Fig.3.2(b) where an excellent agreement between simulation and theory is found.

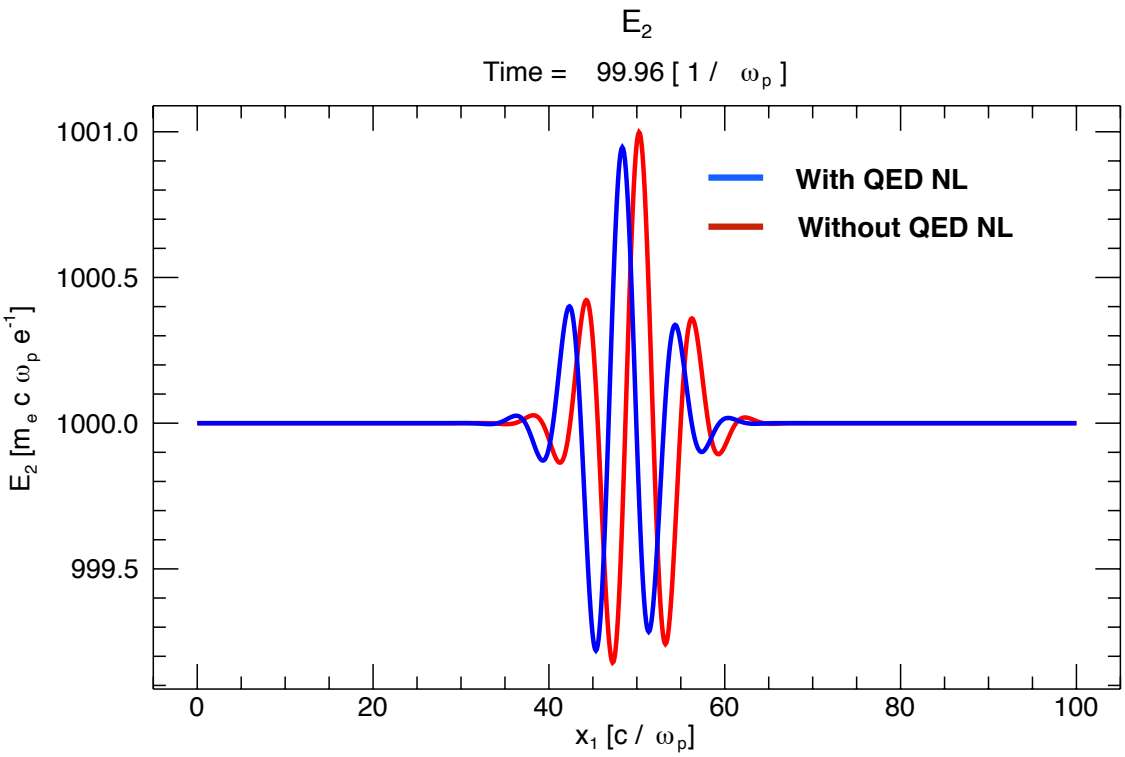


FIGURE 3.1: 1D Gaussian pulse after an entire propagation over a periodic box in the presence of a strong static field, with (blue) and without (red) QED nonlinearities

In this subsection we have derived the effect of the birefringence of the vacuum when a probe pulse propagates in the presence of a strong static field under different conditions, depending on whether the electric/magnetic field is parallel or perpendicular to the direction of polarization. The simulation results show a remarkable agreement with the theoretical expressions. The phenomena of the birefringence of the vacuum is a extremely active topic in the community as it provides a direct experimentally observable consequence of the quantum vacuum. In particular, the current state of the art setup is to counter-propagate a probe X-ray pulse with a strong optical pump laser. In this setup due to the difference of temporal scales of both lasers, the X-ray probe pulse effectively experiences a constant static EM field from the strong pump laser. The details of the very setup will be the topic

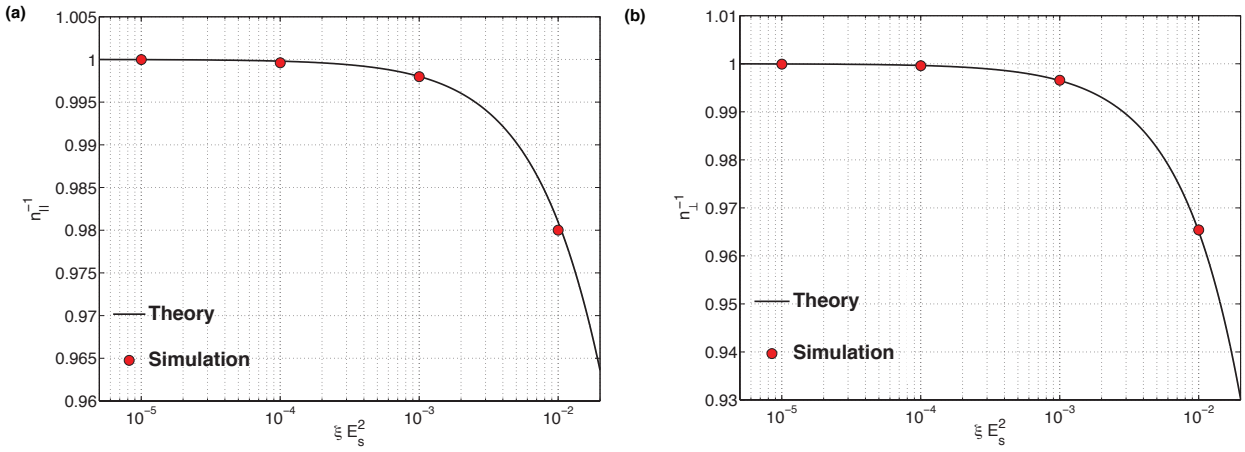


FIGURE 3.2: (a) Phase velocity $(c = 1)$ of probe pulse with polarization parallel to $E_s$, (b) Phase velocity $(c = 1)$ of probe pulse with polarization perpendicular to $E_s$, both as a function of $\xi E_s^2$ parameter

of 4.

### 3.1.2 Counter-propagating plane waves

The birefringence of the vacuum discussed in the previous section is useful to explore the analytical technique of solving the HE QED corrected Maxwell's equations in a limit where one of the fields is static. Another limit is when two waves with similar or equal wavelength and frequency counter-propagate. This setup requires a finer mathematical treatment as there is no longer a separation of scales that allows one to perform an ordering of the problem. Nevertheless, the procedure we will now perform is a valuable technique to solve a set of nonlinear Maxwell's equations with the ansatz that the self-consistent solution is a perturbation to a well known solution of a simpler linear situation. The setup consists of a 1D periodic box with two counter-propagating plane waves polarized in the $y$ direction, with the same frequency and amplitude, we can test how this interaction, which would normally result in a standing wave, is modified in the presence of the HE nonlinearities. This example also serves as an ideal benchmark for the accuracy and stability of the code, once an exact analytic result is obtained.

The theoretical analysis to address this scenario is similar to a Born series of partial waves. Assuming that the solution of the QED Maxwell's equations are of the type

$$E = E_{(0)} + E_{(1)} + E_{(2)} + ... \tag{3.12}$$

$$B = B_{(0)} + B_{(1)} + B_{(2)} + ... \ , \tag{3.13}$$

where $E_{(0)}$ and $B_{(0)}$ are the unperturbed standing wave fields with frequency and wave-number, $\omega_0 = k_0 = 1$, given by $E_{(0)} = E_0 \left[\cos(x-t) + \cos(x+t)\right]$ and $B_{(0)} = B_0 \left[\cos(x+t) - \cos(x-t)\right]$ whilst the remaining terms are successively higher order corrections to the standing wave fields,

weighted by an expansion parameter to be identified. Starting from the modified Maxwell's equations and inserting eq.(3.12) and eq.(3.13) as the expressions for the fields, we arrive at the wave equation for the first order correction to the electric field $E_{(1)}$

$$\Box\, E_1 = S_1(x,t), \tag{3.14}$$

where $\Box = \partial^\mu \partial_\mu$, with $\mu = 0, 1, 2, 3$, is the d'Alembert operator and the source term $S_1 = -\partial_t \partial_x M + \partial_t^2 P$. Inserting the zero order field in the source term, i.e. $P, M = f(E_{(0)}, B_{(0)})$, we arrive at

$$S_{(1)}(x,t) = 16\xi E_0^3 \cos(t)\cos(x)\left[3\cos(2t) - \cos(2x)\right] \tag{3.15}$$

This source term only accounts for the unperturbed fields being inserted into the nonlinear polarization and magnetization. The formal solution of this equation is given by the convolution between the source term and the Green's function of the one dimensional wave operator [42],

$$E_{(1)}(x,t) = \int_0^L \int_0^t dt' dx' G(x,x',t,t') S(x',t'), \tag{3.16}$$

where the Green's function is

$$G(x,x',t,t') = \frac{1}{2} H\left[(t-t') - |x-x'|\right]. \tag{3.17}$$

The modified electric field reads

$$E_{(1)}(x,t) = -2\xi E_0^3 \sin(t)\cos(x)\left[2\sin(2t)\left(\cos(2x) - 2\right) - 4t\right]. \tag{3.18}$$

The corrected field exhibits a secular growth term modulated by an oscillating term. We also notice that the relative amplitude between this term and the unperturbed field amplitude is $\xi E_0^2$ showing again that this perturbative treatment is valid as long as $\xi E_0^2 \ll 1$. Taking the spatial Fourier transform of $E_{(1)}$, we verify that the fundamental mode $\mathrm{k} = \mathrm{k}_0$ is reinforced by the linearly growing term and the appearance of an harmonic at $\mathrm{k} = 3\mathrm{k}_0$. Defining the Fourier transform of $E(x,t)$ as $\tilde{E}(k,t)$, we obtain

$$\tilde{E}_{(1)}(\mathrm{k} = \mathrm{k}_0) = 4\xi E_0^3 t \sin(t) + 3\xi E_0^3 \sin(t)\sin(2t), \tag{3.19}$$

$$\tilde{E}_{(1)}(\mathrm{k} = 3\mathrm{k}_0) = -\xi E_0^3 \sin(t)\sin(2t). \tag{3.20}$$

The next order correction to the field $E_{(2)}$, reveals a $\mathrm{k} = \mathrm{k}_0$ harmonic growing as $\mathrm{t}^2$, a secular $\mathrm{k}_0 = 3\mathrm{k}_0$ term and an oscillating $\mathrm{k} = 5\mathrm{k}_0$ term. Repeating this process to higher orders, we can show that this nonlinear interaction generates odd higher harmonics from vacuum with the relative amplitude between these harmonics obeying the ordering

$$\tilde{E}(\mathrm{k} = 2n+1) = (\xi E_0^2)^n \tilde{E}(\mathrm{k} = \mathrm{k}_0) \tag{3.21}$$

These predictions were compared with the results of the QED solver using field amplitude of $E_0 = 0.0025_{Sch}$, $\lambda_0 = 1$ $\mu$m plane waves and $\xi = 10^{-9}$, such that the higher harmonics can be accurately

resolved above the numerical noise. The spatial Fourier transform of the fields at a certain time is shown in Fig. 3.3 for two simulations, with and without the self-consistent inclusion of HE corrections. We observe that when the nonlinearities are present, the odd higher harmonics are generated with a relative amplitude that matches the ordering given in eq.(3.21). In order to compare the simulation results with eqs.(3.19-3.20), we subtracted from the full solution the classical vacuum electric field $(E_0)$ in order to remove the zeroth order standing wave contribution. We then performed the Fourier transform of this subtracted field. Finally, we tracked the temporal evolution of the amplitude of the $\mathrm{k} = \mathrm{k}_0$ mode in Fourier space and compared it with eq.(3.19). Figure 3.4 shows the temporal evolution of $E_1(\mathrm{k} = \mathrm{k}_0)$ and compares the theoretical points (red) to the simulation results (blue).

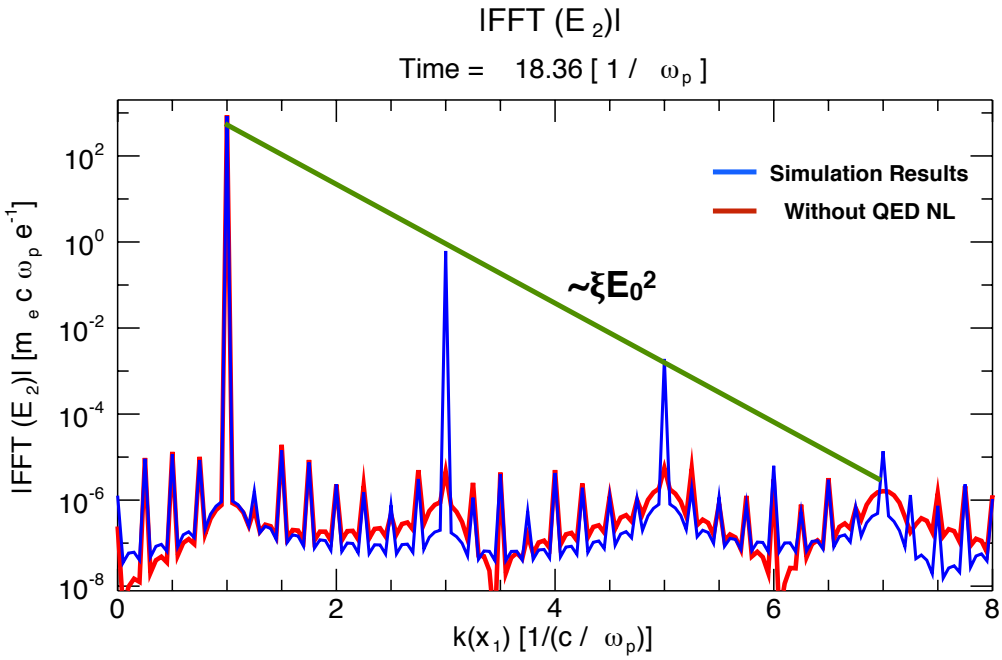


FIGURE 3.3: Spatial Fourier transform of electric field with and without QED NL present. The generation of odd higher harmonics can be observed in blue.

The simulation show an excellent agreement with the theoretical predictions for many laser cycles, ensuring that the algorithm is robust. Despite the one dimensionality of this example, the setup of counter-propagating beams is of great interest for planned experiments at extreme high intensity laser facilities, as outlined in [29].

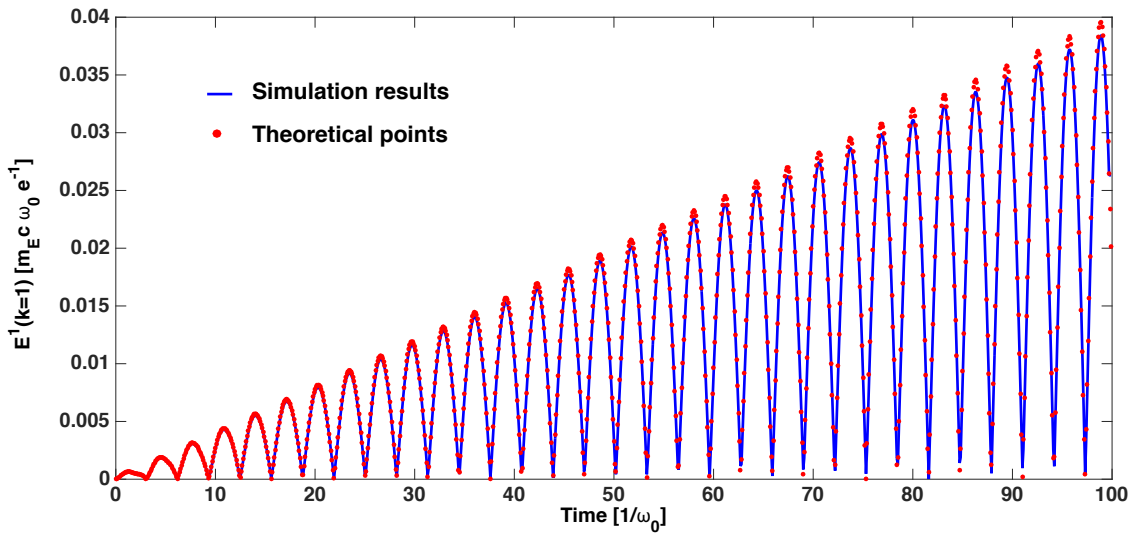


FIGURE 3.4: Temporal evolution of k = $k_0$ Fourier mode of the subtracted electric field.

### 3.1.3 1D Birefringence revisited: Green function formalism

In the previous sub-section the formalism of the Green function was introduced as a mean to solve the one-dimensional wave equation with a source term. It is valuable to understand how how different EM theoretical techniques are consistent with each other in the correct limits. In order to illustrate this we will reproduce the result of the birefringence of the vacuum derived in section 3.1.1, using the Green function formalism applied to the respective wave equation. Considering the field setup of a probe pulse in the presence of a strong static field in the following manner,

$$E_y = E_p(x,t) + E_s \,, \tag{3.22}$$

$$B_z = B_p(x,t). \tag{3.23}$$

As in section 3.1.2 we insert the ansatz that the probe field can be decomposed in $E_p(x,t) = E_{p0} + E_{p1}$ where $E_{p0} = E_0 \cos(k_0 x - \omega_0 t)$ is the unperturbed field obeying the dispersion relation $\omega_0 = k_0$, $\phi = k_0 x - \omega_0 t$ and $E_{p1}$ is the first order correction due to the quantum vacuum, to the unperturbed field, which we shall now calculate. A corresponding ansatz is also valid for the magnetic field. Inserting this into the equations QED correcte Maxwell's equations we obtain the following wave equation,

$$\Box(E_{p0} + E_{p1}) = (\partial_t^2 - \partial_x^2)(E_{p1}) = 4k_0^2 \xi E_s^2 E_0 \cos(\phi). \tag{3.24}$$

this first step is exact since by construction, the wave equation differential operator applied to $E_{p0}$ is zero. The wave equation we are left with was solved by a convolution between the source term and the appropriate Green function. This yields the following electric field,

$$E_p(x,t) = E_{p0} + E_{p1} = E_0 \cos(\phi) + 2E_0 \xi E_s^2 (k_0 t \sin(\phi) + \sin(\omega_0 t) \sin(k_0 x)) \tag{3.25}$$

Eq.(3.25) contains the sum of the zero order unperturbed classical vacuum field with two corrective terms of order $\xi E_s^2$, one with a secular growth rate and an oscillatory term. In this form, the solution

computed does not seem to be consistent with the expected result which is that the phase velocity of the probe pulse is modified. To convince ourselves that in fact this result is consistent with the refractive index Eq.(3.8) we start from the expression that is the solution of the birefringence of the vacuum and carry an expansion. We know that in a birefringent medium a wave will propagate according to

$$E_{\text{bir}} = E_0 \cos(k_0 x - \omega t). \tag{3.26}$$

Where the dispersion relation relating $\omega$ and $k_0$ is not that of the classical vacuum, but rather $\omega = v_\phi k_0 = (1 - 2\xi E_s^2)k_0$. This dispersion relation was calculated using as the phase velocity consistent with the refractive index in Eq.(3.8). To complete this derivation we will now insert this dispersion relation in Eq.(3.26) and expand the result using a standard trigonometric identity.

$$E_{\text{bir}} = E_0 \cos(k_0 x - \omega t) = E_0 \cos(k_0 x - k_0(1 - 2\xi E_s^2)t) = E_0 \cos(\phi - \delta\omega t), \tag{3.27}$$

where $\delta\omega = 2\xi k_0 E_s^2$ and such that $\delta\omega \ll \omega_0$. This last result can be decomposed into a sum yielding

$$E_{\text{bir}} = E_0 \cos(\phi - \delta\omega t) = \cos(\phi)\cos(\delta\omega t) + \sin(\phi)\sin(\delta\omega t) \approx \cos(\phi) + \delta\omega t \sin(\phi), \tag{3.28}$$

keeping a first order term in $\delta\omega$ only. Finally, re-inserting $\delta\omega$, the perturbation to the frequency of the wave due to the quantum vacuum, yields an expression consistent with eq.(3.25), except for a transient term that becomes negligible when $t \gg \omega_0^{-1}$. We finally obtain,

$$E_{\text{bir}} = \cos(\phi) + 2\xi E_s^2 k_0 t \sin(\phi). \tag{3.29}$$

Compared to the previously obtained solution

$$E_{\text{Green}} = E_0 \cos(\phi) + 2E_0 \xi E_s^2 (k_0 t \sin(\phi) + \sin(\omega_0 t)\sin(k_0 x)) = E_{\text{bir}} + 2E_0 \xi E_s^2 \sin(\omega_0 t)\sin(k_0 x) \tag{3.30}$$

This proves that solving the system of nonlinear QED corrected Maxwell's equations via a direct linearization or using the Green's function formalism, yields the same result.

As a discussion for future analytical techniques to be used in more complex setups, it is worth investigating the limitations of both techniques. Both eq.(3.29) and eq.(3.30) have an amplitude that varies with time whilst the wave is travelling through the birefringent medium. This variation of amplitude does not occur in the original solution eq.(3.26). Instead, the solution in eq.(3.26) was derived assuming that the probe pulse was already in the birefringent medium at $t = 0$, meaning that there should be no change in amplitude throughout the propagation.

The changes in amplitude observed in eqs.(3.29-3.30) come from the fact that they are a limit derived from an expansion up to a certain order and valid only for short times where $\delta\omega t$ is much smaller compared to unity. Therefore, we were to keep higher order terms in $\delta\omega$, leads to the same result as doing the full recursive Green function at all orders, that would not include a change in amplitude. This obsrvation leads us to conclude that rather than a change in amplitude, the terms propotional to time are a manifestation of a change in phase, but only up to a certain order.

Despite the limitations in terms of the field amplitudes presented in the approximate solutions, the phase velocity predicted in both models is identical and consistent with the simulation results

shown in fig.(3.2).

As we shall see in Chapter 4 both phase velocity and amplitude effects in the birefringence of the quantum vacuum have a different affect in the outcome of relevant observables in an experimental situation. This is an important connection that one must bear in mind when attempting to perform a theoretical analysis of more complex scenarios involving the birefringence of the vacuum.

## 3.2 2D Results

The one dimensional scenarios addressed in the previous sections were crucial to establish the accuracy and usefulness of the algorithm developed in one-dimension but also to explain analytical techniques one disposes of in order to tackle these problems from a theoretical point of view. However, for practical purposes, the scenarios presented are limited as not only do they deal with plane waves and homogeneous static fields, but most importantly, they are oblivious to important two-dimensional finite-size beam effects that occur in real beams and laser pulses. Therefore, the generalization of the algorithm proposed to two-dimensions provides a tool that can be extremely competitive in simulating realistic scenarios with experimental relevance. This section begins with the demonstration of the birefringence of vacuum in the presence of a static field, in two dimensions, to prove that the generalization of the algorithm to multi-dimensions does not jeopardize its accuracy. The remainder of the section is dedicated to presenting simulation results of the collision between two Gaussian pulses, in different conditions, and the subsequent generation of higher harmonics. These simulations illustrate the usefulness of a multi-dimensional code in scenarios where a self-consistent analytical treatment is not available. This final feature emphasizes the usefulness of the algorithm developed in this thesis.

### 3.2.1 2D vacuum birefringence

When performing a generalization from one dimension to multi-dimensions, a useful benchmark is to verify that the one dimensional results, in a well studied scenario, can be recovered within a two dimensional framework. Using this as motivation, a simple setup is to verify that a 2D plane wave propagating in the $x$ direction, will propagate with a phase velocity given by Eqs.(3.8-3.9) depending on whether the pulse is polarized parallel or perpendicular to the direction of the static field.

Figure 3.5 shows the simulation results of the phase velocity extracted from the simulation for a plane wave propagating in the $x_1$ direction, in a 2D scenario, in the presence of a static field $E_s = 1000$. The fact that the simulation results agree extremely well with the theoretical expression derived for a one-dimensional pulse proves that the 2D generalization of the code is accurate in the one dimensional limit of the birefringence of the quantum vacuum.

This test allows us to move on onto more complex simulation scenarios where a full self-consistent analysis is not possible, with the confidence that the two dimensional code recovers the correct results in the appropriate limits. In order to go beyond simulation setups using plane waves and really explore the effect and complexity of finite size effects, we will now investigate scenarios using realistic laser pulses. In the following cases, the laser pulses used are self-consistently initialised and will

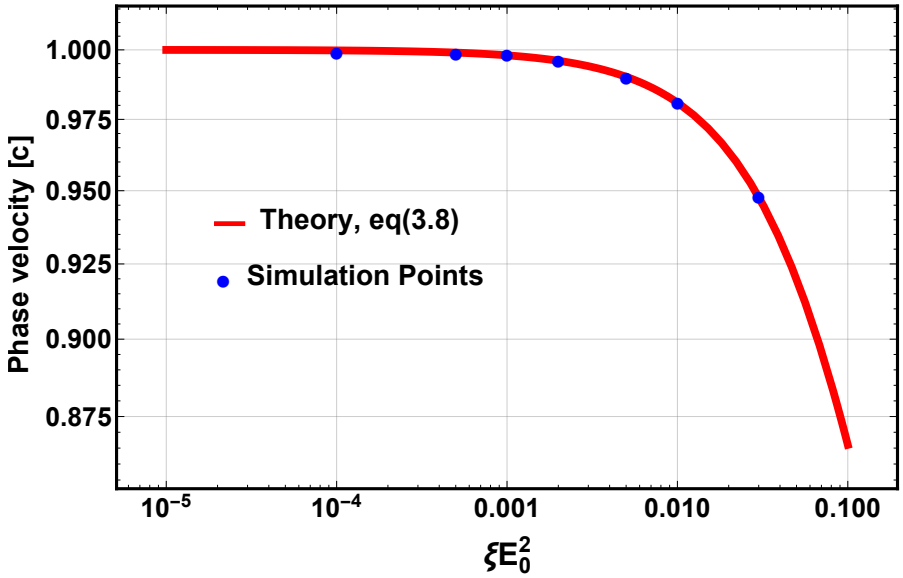


FIGURE 3.5: Simulation results of the phase velocity of a plane wave propagating in the $x_1$ direction in the presence of a strong static field, for different values of the quantum parameter $\xi$. The corresponding prediction previously derived is plotted in red.

have an intensity varying with the distance from the axis of propagation and exhibit the focusing and de-focusing effects associated to realistic laser pulses. A revision of these effects can be found in any standard optics textbook [43].

### 3.2.2 Counter-propagation of Gaussian laser pulses

In order to illustrate the usefulness of our algorithm in multi-dimensions, two setups were investigated in 2D: the counter propagation of two Gaussian pulses interacting at the focal point, and the perpendicular interaction of two Gaussian pulses focused at the same point. For these setups, a consistent analytical treatment becomes cumbersome especially due to the self-consistent treatment of both the transverse and longitudinal component of the pulses.

A quantum parameter of $\xi = 10^{-6}$ was used for the sake of providing illustrative examples. In the first setup two $\lambda = 1$ $\mu$m laser beams with a normalized vector potential $a_0 = 50$ ($\sim 10^{-4} E_s$ in normalized units) and duration of 25 femtoseconds were counter-propagated and interacted in the presence of the QED nonlinearities. Both beams had a waist $W_0 = 2.3$ $\mu$m. Figure 3.6 shows the transverse electric field of the laser beams before interaction, Fig.3.7-(a) the spatial Fourier transform of the beams with $\xi = 0$ (classical limit) and in Fig. 3.7-(b) the Fourier transform of the electric field after the interaction (asymptotic state) including the HE corrections. As shown in Fig. 3.7-(b), after the interaction, odd higher harmonics are also generated as in the 1D case, with relative amplitudes consistent with eq.(3.21). However, in this case the harmonics generated have the same Gaussian behavior as the unperturbed pulses and attain a greater spread in Fourier space after the interaction. After the pulses have spatially overlapped, the harmonics propagate and leave an imprint of the nonlinear interaction, that co-propagates with the original beam.

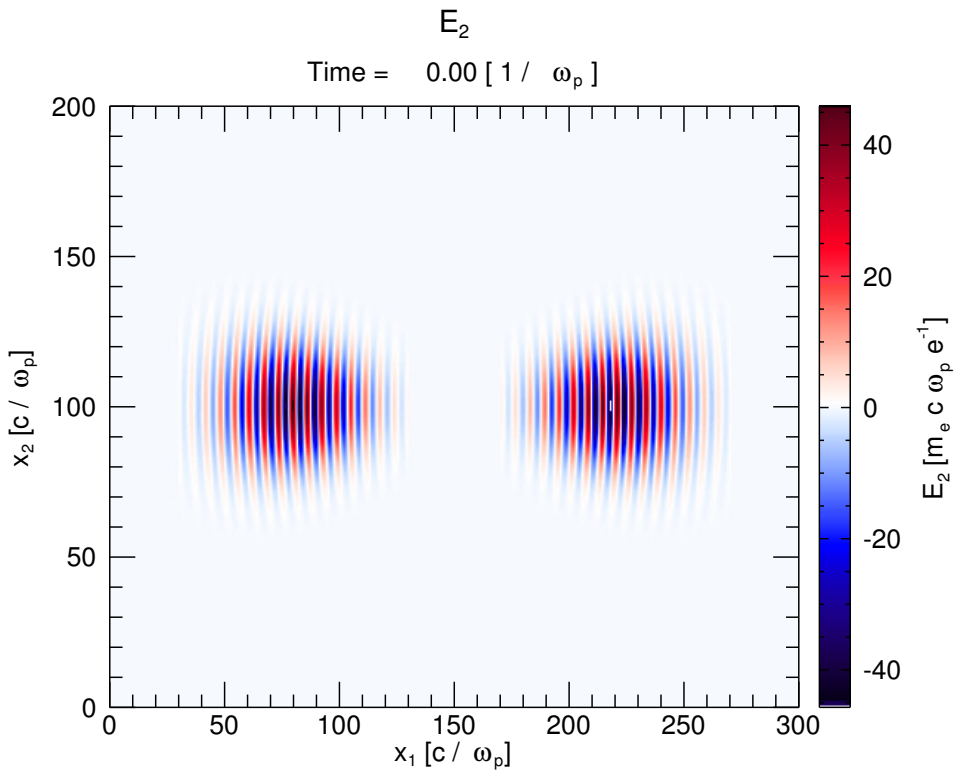


FIGURE 3.6: Initial setup of Gaussian pulses. Both pulses are polarized in the $x_2$ direction and will focus in the center of the box.

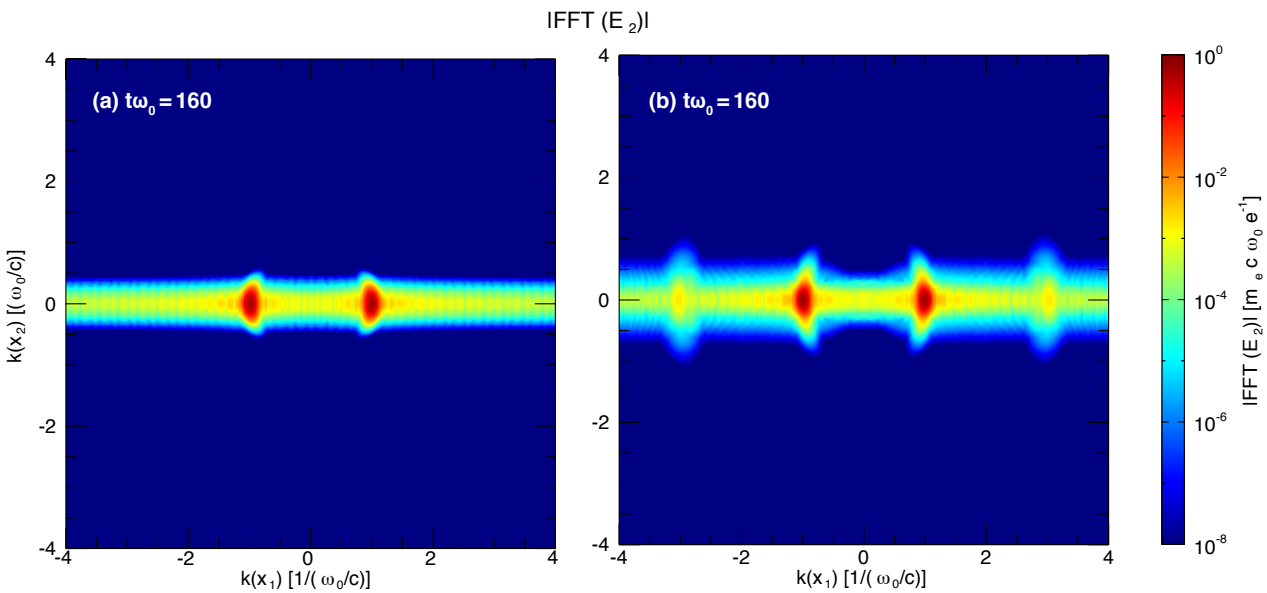


FIGURE 3.7: Spatial Fourier transform of the electric field, (a) after the interaction but when QED corrections are absent, (b) after the interaction with self-consistent inclusion of the quantum corrections. $k = 3k_0$ harmonics and small distortion of $k = k_0$ can be observed.

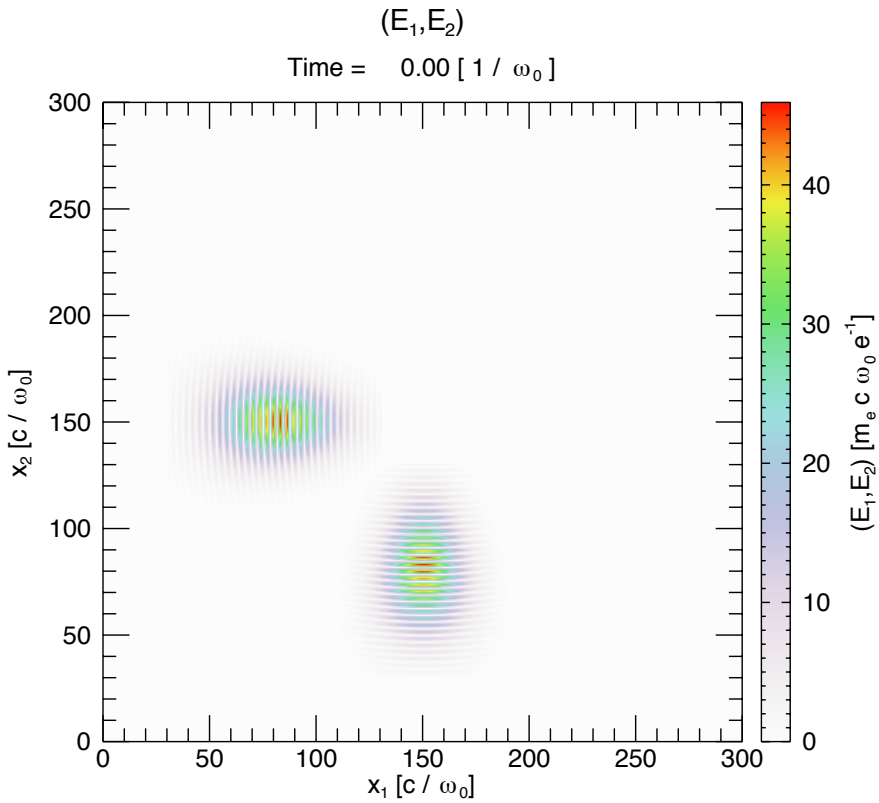


FIGURE 3.8: Electric field setup for two Gaussian pulsed traveling in perpendicular directions but focusing on the same point.

The second setup shown in Fig. 3.8 contains richer physics: it comprises of two $1\mu$m Gaussian pulses with $a_0 = 50$ and wave-numbers $k_1$ and $k_2$ that interact at their focus, with $k_1 \perp k_2$. The beam parameters are equal to those of the previous setup. The initial Fourier space of the beam propagating in the $x$ direction is shown in Fig. 3.9-(a) and this spectrum would remain unaltered during the interaction in the classical limit ($\xi$= 0). During the peak of the nonlinear interaction (at the focal point) we see in Fig. 3.9-(b) that many pairs of $(k_1, k_2)$ harmonic combinations are being generated. More interestingly, there appears to be a continuous filling of Fourier space in between the expected harmonics integer combination as the spatial overlap creates a multitude of nonlinear Gaussian modes. This effect is lessened after the interaction since there is no longer a source to feed these regions of Fourier space and only the integer expected combination of $(k_1, k_2)$ harmonics are left as an imprint of the interaction, see Fig. 3.9-(c). The longitudinal field component, inherent to a non-plane wave propagation, triggers a self-interaction of the Gaussian pulse through the QED nonlinearities [44]. This self-interaction plays the role of a coupling source when both pulses interact spatially. Such terms are responsible for the $(k_0, 2k_0)$ and the higher order $(2.5k_0, 2k_0)$ harmonic points in Fig. 3.9-(b). The self-interaction coupling combined with the different propagation directions, is the reason why this second setup generates several new harmonic couplings, compared with

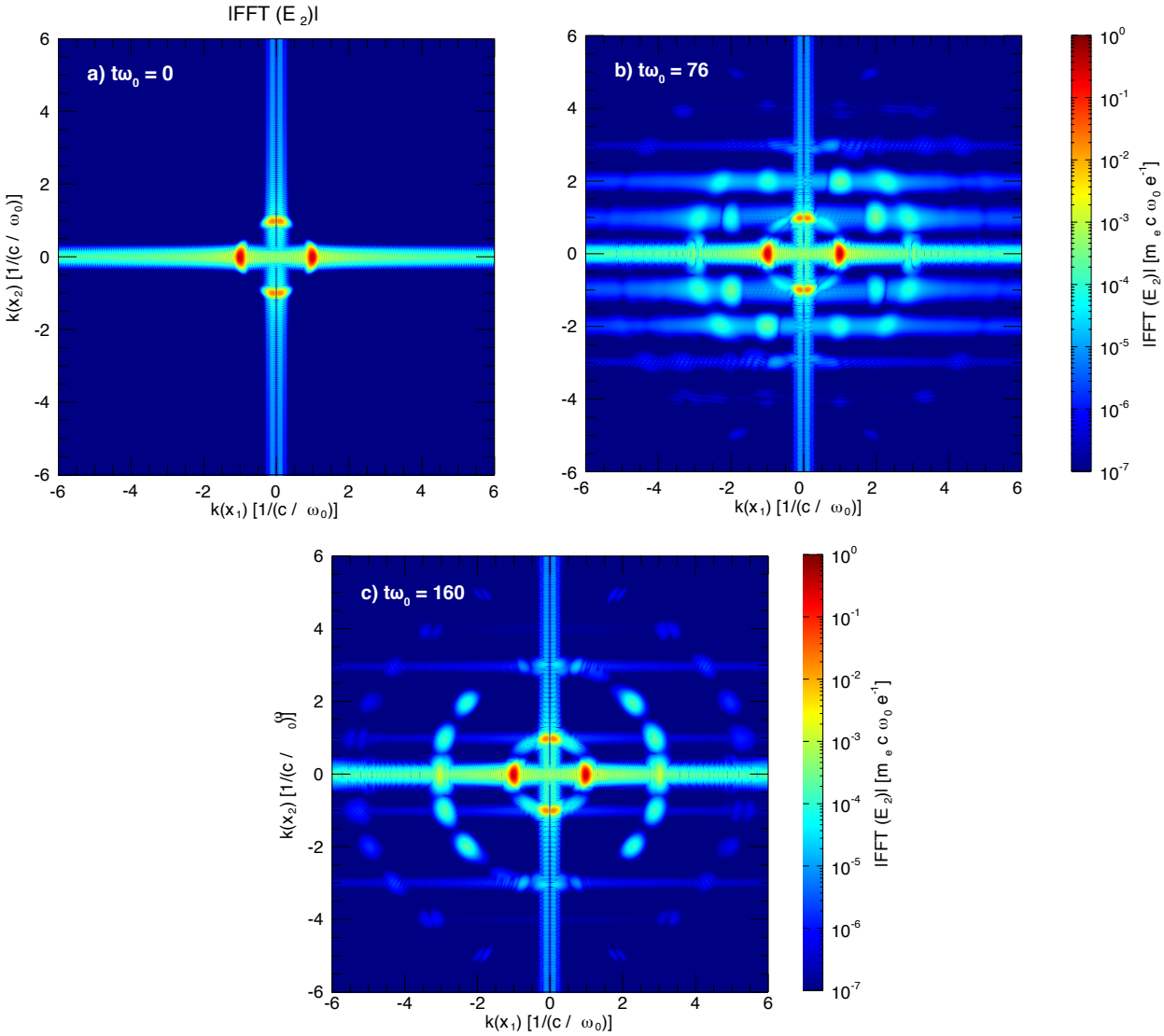


FIGURE 3.9: Spatial Fourier transform for $E_2$ field at different stages of interaction. (a) Initial Fourier space, if there were no vacuum nonlinearities this spectrum would remain unchanged throughout the interaction. (b) At peak of nonlinear interaction when the pulses are completely overlapped in space. (c) Asymptotic state: after the nonlinear interaction the pulses propagate independently but with higher harmonics generated from the interaction.

the previous counter-propagating setup.

The Fourier spectra obtained in these two setups show that the harmonics generated in either case are distinct, thus allowing to clearly distinguish both cases. Future work will include the analytical study of the relative intensity and spectral width of the generated harmonics and their possible relation with other beam parameters and with the fundamental interaction parameter $\xi$. Namely, it is of great interest to understand how the production of these higher harmonics from vacuum may be optimized in terms of the duration of the pulses as these results can provide signatures of experimental relevance. A future setup to explore will also include the interaction of two laser beams at an arbitrary angle $0 < \theta < \frac{\pi}{2}$ radians in order to model realistic experimental conditions. If this angular dependence of the interaction is well understood, one could in principle determine how well

aligned two ultra-intense beams are by looking at the Fourier spectrum after a vacuum interaction. Finally, if one assumes that the parameter $\xi$ is a well measured quantity, one could precisely measure the initial intensity of the beams. This final property enhances the interest in this analysis in a time where ultra-intense laser facilities are being upgraded or constructed around the world and the experimental techniques to measure such intensities is still not firmly established.

# Chapter 4

# Realistic scenarios of vacuum birefringence

In chapter 3 we discussed how the HE QED corrections to Maxwell's equations can induce the phenomenon of vacuum birefringence by creating an effective refractive index, greater than unity, for a pulse traveling in the presence of a strong static field. This physical consequence opens the door to the experimental detection of the existence of the quantum vacuum, in the strong field regime. In this chapter we start by explaining the experimental setup proposed for the measurement of vacuum birefringence followed by an extension of the theoretical analysis performed in chapter 3. We show that the physical observables in realistic setups are the ellipticity and angle of rotation in the polarization of a probe pulse. We will further show how the simulations that can be performed using the new numerical solver developed in this thesis, whilst emphasizing the fact that such is only possible using high performance computing tools. The diagnostics created for this setup will be explained and the results of two-dimensional simulations presented. The aim of this chapter is to prove that our work can be a valuable tool within the community to simulate currently planned experimental setups, without approximations, thus complementing the extensive theoretical work already performed within a QED formalism. Finally, the fact that our algorithm is fully EM means that the results of our simulations are the fields and therefore contain information about experimentally relevant quantities such as phase and amplitude.

## 4.1 Setup and theoretical framework

### 4.1.1 Vacuum Birefringence: probing the quantum vacuum

As originally proposed in [38, 39] and re-examined in detail in [25, 45, 46], an X-ray probe pulse of wavelength $\lambda_X$ will experience vacuum birefringence when counter-propagated with a strong optical pump laser of wavelength $\lambda_0$. In particular, due to the difference of scales ($\lambda_X \ll \lambda_0$), the X-ray probe will effectively experience a quasi-static field according to the pump profile. The setup of interest is illustrated in fig.4.1 where we see the X-ray probe pulse initially polarized at $45^o$ compared to the polarization of the pump pulse, leaving the region of interaction with an ellipticity induced in its polarization as well as a rotation on the plane of polarization, due to the quantum vacuum interaction.

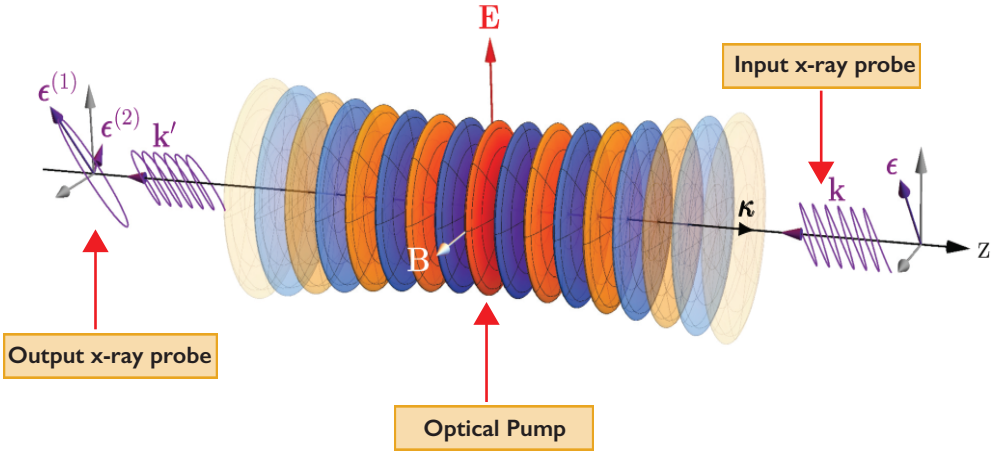


FIGURE 4.1: Experimental setup proposed to study the birefringence of the quantum vacuum via the change in the ellipticity of the polarization of a X-ray probe pulse, after trasversing a strong optical pump laser.

This setup was first proposed in [39] including a theoretical analysis that did not take into account the fact that the pump laser has a profile which varies with space and time. Since then, more powerful theoretical methods have been employed to predict the rotation of polarization and ellipticity that is expected to be observed for more complex setups taking into account finite-size beam effects. In particular, in [45] the authors use a QED M-matrix scattering formalism in order to compute the number of probe photons that flip between the two possible polarization states as well as the momentum distribution of the scattering photons, thus predicting how the probe will be modified after the interaction whilst taking into account the approximate beam structure of the pump. The authors of [46, 47] use a so-called light-front QED formalism, whereby they integrate over the world-line of a given photon within the probe pulse, in the presence of the background EM field created by the optical pump. Despite the impressive results derived in the works described, approximations regarding the pump and probe profiles must be made within both theories. These include neglecting the longitudinal component of a Gaussian beam, or limitations due to the paraxial approximation. We would like to emphasize that since our code solves the exact set of nonlinear Maxwell's equations for an arbitrary field configuration, we are able to go beyond such approximations and deliver exact results within the precision of the numerical scheme. Having explained the state of the art regarding the theoretical methods to tackle this problem, we will describe in the next section, from an electromagnetic point of view, why the phenomena of rotation of polarization and induced ellipticity occur.

### 4.1.2 Birefringence in a static field revisited

We will start with a one-dimensional approach to the problem and successively increase the complexity of the setup whilst bench-marking our results with the code. Consider a one-dimensional pulse propagating in a background static electric field, as already addressed in section 3.1.1, with a polarization at an arbitrary angle to direction of the static electric field. Without loss of generality, the

field setup can be written as

$$E_y = E_s + \cos(\theta)E_p \ , \tag{4.1}$$
$$E_z = \sin(\theta)E_p \ , \tag{4.2}$$
$$B_y = -\sin(\theta)E_p \ , \tag{4.3}$$
$$B_z = \cos(\theta)E_p \ , \tag{4.4}$$

with

$$E_p = E_{p0}\cos(k_0 x - \omega t)\exp(-(x - x_0 - ct)^2/2\sigma^2),$$

as the expression for the probe pulse package of frequency $\omega$, wave-number $k_0$, $\sigma$ the duration of the pulse, $E_{p0}$ the amplitude and $x_0$ defining the initial position. Furthermore, $E_s$ represents the strong static field and $\theta$ the arbitrary angle between the direction of $E_s$ and the polarization of the probe pulse. As we have seen in sec.3.1.1, the static electric field will induce a non-unity refractive index of the vacuum making the probe pulse travel with a phase velocity different from $c$. We also showed that the refractive index of the vacuum depended on the direction of the polarization of the probe pulse relative to the direction of the static field. In this scenario, the polarization of the probe pulse can be decomposed parallel and perpendicular components relative to the direction of the static field, such that each one of these field components will experience a different refractive index given by Eqs.(3.8-3.9) respectively. This setup is analogous to a bi-axial homogeneous anisotropic medium, defined such that the electric permittivity and magnetic permeability tensors are diagonal matrices whose elements in general differ. The fact that each field component will travel with a different phase velocity means that they continuously dephase from each other as they propagate in the quantum vacuum. The relative phase between both components introduced by the propagation is called retardance. The retardance introduced in this case is very small since the corrections to the refractive index of the vacuum are of the order $\xi E_s^2$. Nevertheless, this retardance will induce a small ellipticity in the polarization of the probe pulse, as we shall now prove. The approximate phase velocity for the parallel and perpendicular field components are given by the inverse of the refractive indexes as,

$$v_{\parallel} = 1 - 2\xi E_s^2 \ , \tag{4.5}$$
$$v_{\perp} = 1 - \frac{7}{2}\xi E_s^2 \ . \tag{4.6}$$

Assuming that the polarization angle is $\theta = \frac{\pi}{4}$, we obtain the following expressions for the fields:

$$\vec{E_p}(t,x) = \frac{A(x)}{\sqrt{2}}\left(\exp(-j\omega t)\exp(jk_{\parallel}x)\vec{e}_y + \exp(-j\omega t)\exp(jk_{\perp}x)\vec{e}_z\right) \ , \tag{4.7}$$

where $A(x)$ is the spatial pulse envelope with a Gaussian profile and $k_{\parallel}$, $k_{\perp}$ denote the parallel and perpendicular wave-numbers respectively. After a propagation time $T$ over a distance $d$ and using the relation between $v_{\phi}$ and the wave-number, we can re-write the above expression making it clear

the ellipticity induced in the polarization is due to the retardation effect,

$$\vec{E}_p(T,d) = \frac{A(x)}{\sqrt{2}}\left[\exp(-j\omega T)\exp(jk_{\|}d)\vec{e}_y + \exp(-j\omega T)\exp(jk_{\perp}d)\vec{e}_z\right] \tag{4.8}$$

$$= \frac{A(x)}{\sqrt{2}}\exp(-j\omega T)\left[\exp(jk_0(1-2\xi E_s^2)d)\vec{e}_y + \exp(jk_0(1-\frac{7}{2}\xi E_s^2)d)\vec{e}_z\right] \tag{4.9}$$

$$= \frac{A(x)}{\sqrt{2}}\exp(-j\omega T)\exp(jk_0 d)\left[\exp(-j\delta)\vec{e}_y + \vec{e}_z\right]\exp(-jk_0\frac{7}{2}\xi E_s^2 d), \tag{4.10}$$

where $\delta = (\frac{7}{2}-2)\xi E_s^2 k_0 d = \frac{3}{2}\xi E_s^2 k_0 d$ is the difference of phase between both the field components and is defined as the ellipticity induced on the probe pulse due to the quantum vacuum interaction. It must emphasized at this point that an ellipticity in the polarization of a pulse is a directly observable quantity thus representing an experimental signature of the nonlinear quantum interaction between the probe field and the background static field. In particular, techniques to measure extremely small ellipticities of the order of $10^{-9}$ for x-rays and $10^{-6}$ for optical lasers, have been developed in recent years [48]. To conclude this section we reiterate that the ellipticity induced in the polarization of a pulse traveling in the presence of a static electric field is approximately

$$\delta = \frac{3}{2}\xi E_s^2 k_0 d = \frac{3}{2}\frac{2\pi d}{\lambda_0}\xi E_s^2. \tag{4.11}$$

The fact that this result is proportional to the ratio $d/\lambda_0$, is physically relevant as it means that the greater the interaction length ($d$) compared to the vacuum wavelength $\lambda_0$, the greater the ellipticity induced. This model is however over-simplistic as in realistic scenarios, the role of the background strong static field is replaced with that of an ultra-intense laser pulse with optical frequency such that from the point of view of the probe pulse (x-ray), the field is effectively static over long periods of interaction. As is clear from the simulations performed in Chapter 3, the setup described in this sub-section is straightforward to simulate in order to verify how accurate eq.(4.11). However, before this is done, we will briefly digress to address the issue of how the ellipticity of the polarization may be extracted from the simulation in a systematic and reliable way.

### 4.1.3 Post-processing diagnostic: polarization diagnostic

In the study of the birefringence of the vacuum with the aim of simulating experimentally relevant EM setups, it is imperative to use a diagnostic able to measure the polarization of a laser pulse. In general, due to the dynamic nature of the quantum vacuum interactions, the polarization of a pulse may be varying in space during different time intervals of the simulation box. Therefore, we developed a diagnostic that acts as a polarization detector that can be placed, for specific time intervals, in a given spatial position of the simulation. To illustrate the use of this diagnostic, consider the one-dimensional setup shown in fig.4.2(a). In this example,the detector is placed at the position $x_1 = 150$ and the probe pulse travels through a static background electric field. The detector we developed will record pairs of field values $(E_z, E_y)$ at that point, as a function of time. Each of these points will then be plotted in a $(E_z, E_y)$ graph, thus allowing us to visualize the relative phase between both field components in time and measure the polarization of the pulse. This result is shown in fig.4.2(b). As this figure shows, we see a straight line of gradient one, confirming that the pulse is polarised

with an angle $\theta = -\pi/4$ in the $y - z$ plane. However in fig.4.2(b) it can also be seen that the line has a small thickness. This thickness is due to the fact that the polarisation has now the form of an extremely oblate ellipse. As the ellipticity induced cannot easily be resolved in fig.4.2(b), we perform the following trick: since we know that the ellipse has it's major axis coinciding with a line of gradient one in this graph, we rotate the coordinate system by an angle $\theta = -\pi/4$ using the following transformation:

$$x' = x\cos(\theta) - y\sin(\theta) \tag{4.12}$$

$$y' = y\cos(\theta) + x\sin(\theta), \tag{4.13}$$

where it is readily verified that the transformation matrix has a determinant equal to one. Applying the above transformation to the data collected by the detector, we obtain fig. 4.2(c) where the structure of the ellipse can be resolved in a far clearer way. Essentially, this transformation makes the x-axis of the figure correspond with the major axis or the ellipse. Finally, the diagnostic developed performs one final stage by fitting the data obtained to the general expression of an ellipse in the general quadratic form, given by

$$a'x^2 + 2b'xy + c'y^2 + 2d'x + 2e'y + f' = 0\ , \tag{4.14}$$

with fitting coefficients $a', b', c', d', e'$ and $f'$. The fitted ellipse is then plotted on the same figure as the data points and the fitting coefficients converted to the more useful ellipse parameters that parametrise an ellipse in the general form. Figure 4.2(d) shows the result of this fit in blue. Physically, the magnitude of the ellipticity induced is a measure of the flatness of the ellipse which is directly related to the magnitude of the quantum vacuum interaction.

The diagnostic developed includes a simple graphic interface that plots the simulation domain and allows the user to select where the detector has to be placed in a dynamical way. This feature combined with the fact that the detector is able to probe whatever time scales of the simulation desired, makes this a very useful and robust tool to analyse scenarios where, for example, the ellipticity induced on the probe pulse, varies as a function of the distance.

Finally, regarding the coordinate rotation performed to center the ellipse, it is worth noting that if after a rotation by the initial angle of polarisation (in this case $\theta = \pi/4$), there remains a residual de-centering of the major axis of the ellipse compared to the new $x$-axis, it means that the angle of the rotation performed does not coincide with the polarization angle of the pulse. This residual angle shows that during the interaction a rotation in the plane of polarisation of the probe pulse occured. This is a different physical effect called rotation of the angle of polarization, which we will shortly explain, that can eventually be another signature of the a quantum vacuum interaction. This effect is relevant in more complex setups where the amplitude of both field components change in a non-trivial way.

To illustrate the importance of the diagnostics developed, coupled with the QED solver, we will now use the ellipse fitting parameters obtained to extract the ellipticity of the polarization obtained in the example above and compare it with the theoretical result, eq.(4.11). To achieve this, we must

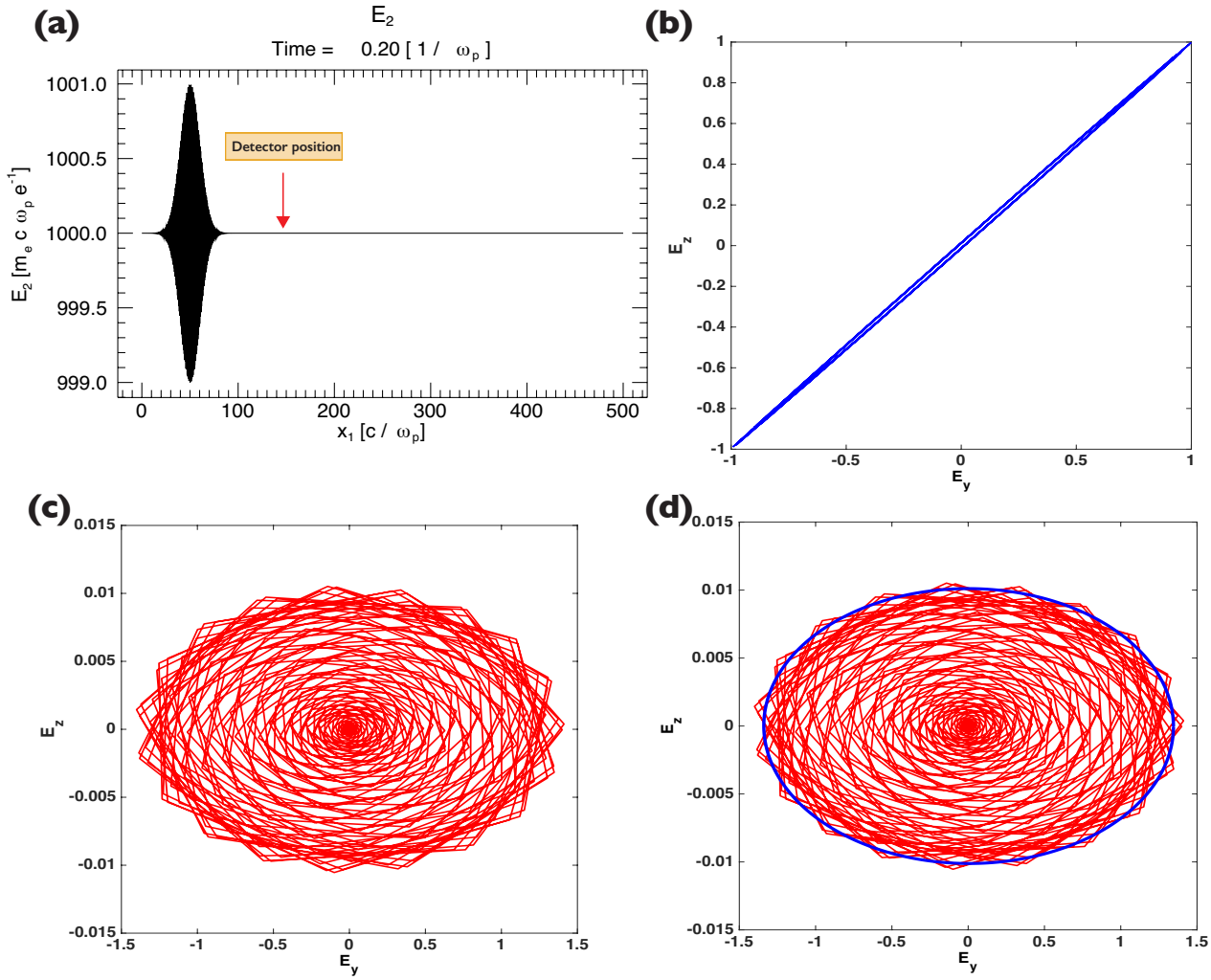


FIGURE 4.2: (a) Setup described in section 4.1.1 where a probe pulse polarized with an angle $\theta = \frac{\pi}{4}$ propagates in the presence of a strong static field, $E_s = 1000$ (b) Result of polarization diagnostic returned by the detector showing a line of gradient one but with a small thickness caused due to the ellipticity induced in polarization of the pulse. (c) Polarization graph of the points presented in (b), rotated by $\theta = -\frac{\pi}{4}$ as to center the coordinate system such that the horizontal axis coincides with the major axis of the ellipse, thus resolving the ellipticity in a more precise way. (d) The diagnostic finally performs a fit using the least squares method of the outer points of the ellipse to the general quadratic equation for an ellipse, eq.(4.14).

first obtain an expression that relates the geometrical parameters of an ellipse (major radius, minor radius etc.) to the physical ellipticity of the polarization. A general derivation of the relation between the structure of the EM fields and the corresponding geometric parameters of the ellipse induced in the polarization, is presented in Appendix A. For this example, we show that the ellipticity $\delta$ is directly related to the minor radius $b$ of the ellipse by the expression

$$b = \frac{E_p}{\sqrt{2}}\delta \,, \tag{4.15}$$

where $E_p$ is the initial amplitude of the probe pulse and $\delta$ is the ellipticity, already defined as the

accumulated phase difference between the two components of the probe pulse. Figure 4.3 shows the rotated ellipse and corresponding fit for the simulation performed with the setup previously described of a probe pulse propagating in the presence of a strong static field. The simulation was performed with a probe pulse with a 0.1 keV pulse with a normalized wave-vector $k_0 = 10$ and amplitude $E_p = 1$, in the presence of a static field of normalized magnitude $E_s = 1000$. The quantum vacuum coupling parameter used was $\xi = 10^{-11}$ and the detector was placed at $x = 150$, such that the length of interaction is equivalent to $d = 100$. All parameters were normalized with the same normalizations as in section 3.1.1. The fit returned a minor radius of the ellipse $b = 0.0103$ corresponding to an ellipticity of

$$\delta_{sim} = \frac{\sqrt{2}b}{E_p} = 0.0143$$

whereas the expected theoretical value is

$$\delta_{theo} = \frac{3}{2}\xi E_s^2 d k_0 = \frac{3}{2} \times 10^{-11} 1000^2 \times 100 \times 10 = 0.015\ .$$

Therefore, the ellipticity extracted from the simulation is accurate compared to the theoretical prediction. This finding not only serves as an excellent benchmark for the precision of the code, but also proves that the diagnostic developed serves as a powerful tool to study birefringence scenarios. Finally, there is one crucial feature revealed by the simulation results in this setup that must be emphasized. Since the strong static field is present throughout all the spatial domain of the simulation, it acts as a constant source of vacuum birefringence making the ellipticity constantly increase with the propagation distance as the probe field components are continuously becoming more de-phased. In fig.4.3, we see that the ellipse formed is actually a spiraling ellipse whose minor radius is continuously increasing. This means that, if we were to place the detector at a distance $d_2 = d + \Delta$, then the minor radius, and corresponding ellipticity induced would also increase by the ratio $d_2/d$. This will not be the case in more sophisticated setups where the x-ray probe pulse will interact with an optical pump laser, due to the finite length of the interaction created by the profile of the pump. This example also serves to illustrate a feature that is intuitive from the start: the greater the interaction region of the quantum vacuum is, the greater the induced ellipticity. Thus, we should place a strong optical laser as a pump, ideally, as intense as possible, for the longest duration possible. Finally, an important consequence that emerges from this analysis is that the ellipticity induced in the probe pulse due to vacuum birefringence is a cumulative effect.

We have shown, via simulations, that for a pulse propagating with a linear polarization of angle $0 < \theta < \pi/2$ relative to a strong static field, there is an ellipticity induced in the polarization due to the quantum interaction of vacuum birefringence. We developed a simple theoretical model to explain the ellipticity induced and predict it's value. We then compared the theoretical value calculated to that extracted from the simulation results using a diagnostic we developed. This comparison yielded an extremely accurate result thus proving the how powerful the algorithm developed in this thesis can be deliver simulation results showing a variety of phenomena associated to the quantum vacuum. With the tools developed so far and motivated by accurate results in the example presented, in the next sections we will tackle more realistic setups, from both a theoretical and simulation point

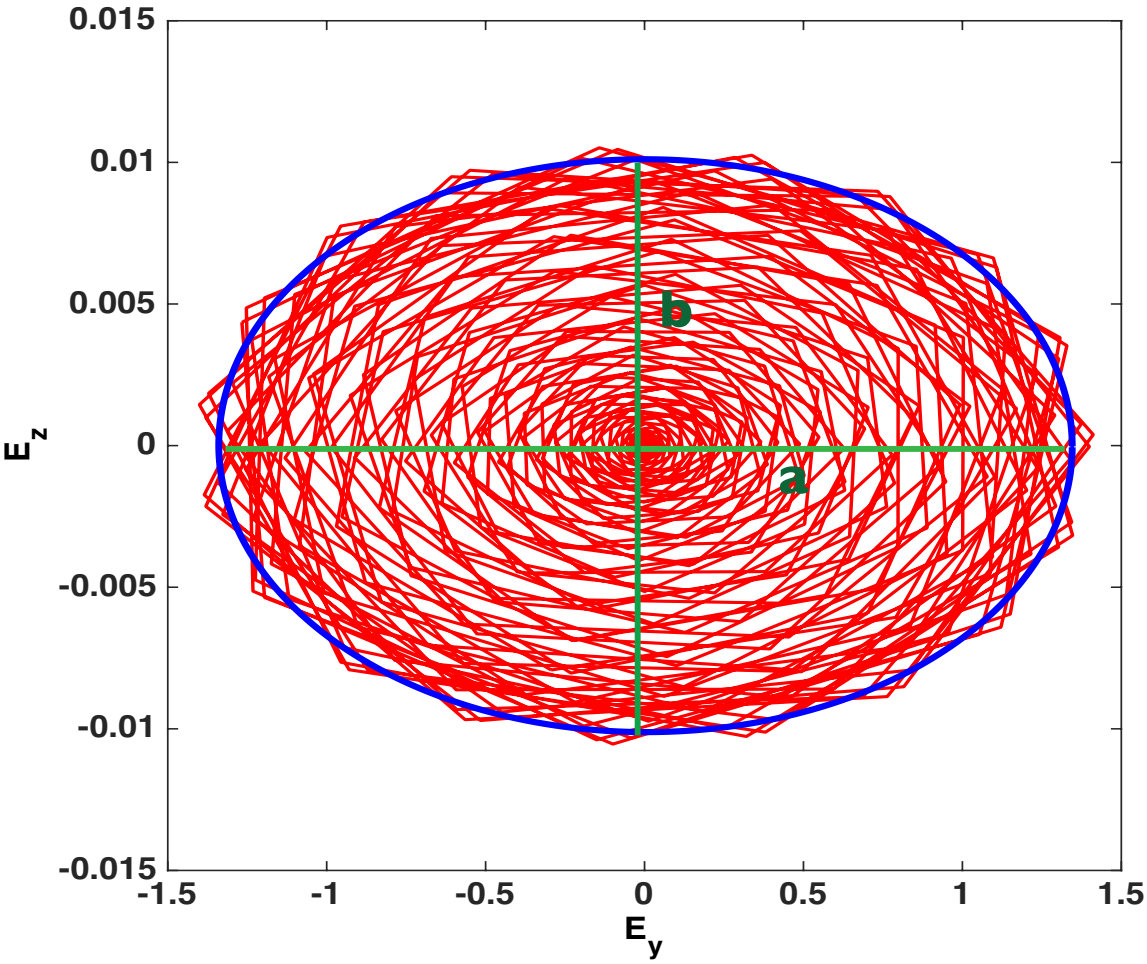


FIGURE 4.3: Polarization plot showing the ellipticity induced in the polarization of the probe pulse after propagating in a birefringent vacuum, caused by a strong static field, over a propagation distance $d = 100$. The labels $a$ and $b$ define the major and minor radii of the fitted ellipse respectively and are an output of the diagnostic developed. Using these values we can extract the value of the ellipticity induced in the polarisation of the pulse, from the simulation.

of view. The ultimate aim being to provide realistic predictions for quantum vacuum signatures that can be expected in planned experimental scenarios.

## 4.2 2D Birefringence with a realistic pump profile

In the previous section we studied the ellipticity induced in the polarisation of a probe pulse propagating in the presence of a strong static field. Despite providing useful physical insight, this scenario does not accurately portray a realistc experimental scenario where it is a strong optical laser pump, whose profile is not static, that creates the birefringence of the vacuum for the X-ray pulse. To address this, we simulate the following 2D setup, in a 1D limit, illustrated in fig.4.4, where a 10 keV X-ray is counter-propagated with a 1 $\mu$m optical pulse, both with duration of 40 fs. The intensity of the optical pump is $10^{23}$ Wcm$^{-2}$ whereas the X-ray laser had an intensity of $10^{18}$Wcm$^{-3}$. These parameters were

chosen according to the proposed beam parameters for the LCLSII update and the new SLAC X-ray laser. As shown in fig. 4.4(a), the transverse profile of the lasers was chosen to be constant (plane wave in 2D). This was done so that we can gradually increase the complexity of the setup and begin by studying exclusively how introducing a profile to the pump laser effects the ellipticity induced, rather than including at this stage the greater complexity of transverse beam effects.

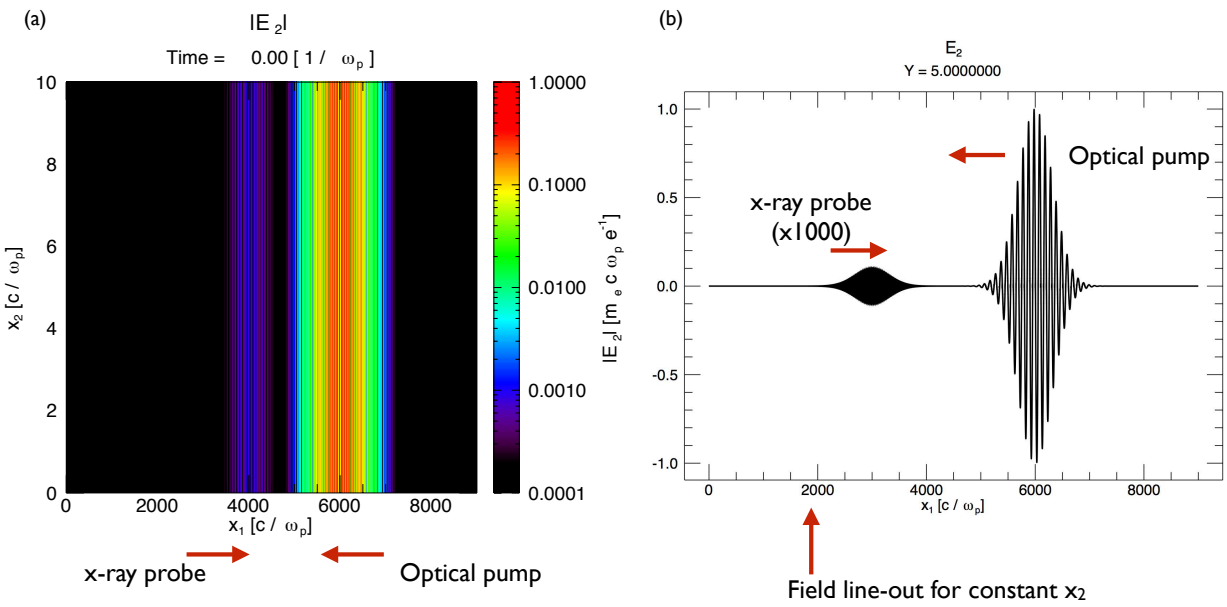


FIGURE 4.4: (a) 2D Contour plot of the field setup we wish to simulate. In this simulation we counter-propagate a weak X-ray probe laser (traveling to the right) with a strong optical laser (traveling to the left). In the transverse direction there is no profile of the beams, making this setup in practice quasi one-dimensional. (b) line-out for a constant $x_2$ of the plot shown in (a) where we can see the longitudinal profile of each laser as well as the difference in wavelengths

We will now address, from a theoretical perspective, the EM setup showed in fig.4.4. The starting point fo describe this scenario is given by the following field configuration

$$E_y = \frac{1}{\sqrt{2}} E_{py} + E_0(x,t) \ , \tag{4.16}$$

$$E_z = \frac{1}{\sqrt{2}} E_{pz} \ , \tag{4.17}$$

$$B_y = -\frac{1}{\sqrt{2}} B_{py} \ , \tag{4.18}$$

$$B_z = \frac{1}{\sqrt{2}} B_{pz} - B_0(x,t) \ . \tag{4.19}$$

Where $E_0(x,t) = B_0(x,t)$ represent the self-consistent fields of the optical pump envelope. To create a model to tackle this scenario using an EM model, we will apply the WKB (Wentzel-Kramers-Brillouin) method to solve the wave equation for the probe pulse, taking into account the profile of the pump. Let us briefly explain the basis of the WKB method and explain why it can be applied to our problem.

### 4.2.1 Solving the wave equation using the WKB approximation

Many problems in physics, once formulated,have the need to solve a wave equation. The full homogeneous wave equation for the variable $y(x,t)$, normalized such that $v_\phi \equiv \frac{v_\phi}{c}$ can be written as

$$\left(\partial_x^2 - \frac{1}{v_\phi^2}\partial_t^2\right) y(x,t) = 0, \tag{4.20}$$

where $v_\phi$ is the phase velocity of the wave. Applying the anstatz that $y \sim A(x)e^{j\omega t}$ yield the well known 1D Helmhotz equation

$$\left(\partial_x^2 - \frac{\omega^2}{v_\phi^2}\right) A(x) = 0\ . \tag{4.21}$$

Defining the wave number $k = \frac{\omega}{v_\phi}$, eq.(4.21) can be solved for $A(x)$ where two constants, $c_1$ and $c_2$ still need to be determined by the initial conditions. This solution is given by

$$A(x) = c_1 \exp(jkx) + c_2 \exp(-jkx)\ , \tag{4.22}$$

where the sign of each exponential will define the direction of propagtion. This derivation is valid as long as the wave number is constant. The WKB approximation can be used to solve wave equations in the form of eq.(4.21) but with $k$ being a function of the coordinate of the differential equation. Therefore we wish to solve the following wave equation,

$$\left(\partial_x^2 - k^2(x)\right) A(x) = 0\ , \tag{4.23}$$

by assuming the solution is of the form

$$A(x) = c_3 \exp\left(\pm j \int k(x)dx\right). \tag{4.24}$$

To verify the validity of this solution, we insert the ansatz in eq.(4.23) and by inspection try to understand when the solution is valid. This calculation can be easily shown to yield,

$$\left(\partial_x^2 + k(x)^2\right) \exp\left(\pm j \int k(x)dx\right) = \pm j k'(x) \exp\left(\pm j \int k(x)dx\right). \tag{4.25}$$

Therefore, if the right hand side of eq.(4.25) is negligible compared to the left hand side, the ansatz is valid. This will be the caseh as long as the scale of variation of the wave number is slow compared to the magnitude of the wave number. This criteria can be defined more rigorously by comparing the order of both terms in eq.(4.25), yielding

$$\frac{dk(x)}{dx}\frac{1}{k^2(x)} \ll 1\ . \tag{4.26}$$

It can be shown that the next order of the WKB approximation leads to a correction in the amplitude of the wave to account for the conservation of energy flux. This leads us to state the solution of

eq.(4.23) under the WKB approximation

$$A(x)_{WKB} = \frac{1}{\sqrt{k(x)}} \exp(\pm j \int k(x)dx) \ . \tag{4.27}$$

For the purposes of our work we must solve a wave equation for a probe pulse in the case where the refractive index of the quantum vacuum (which is closely related to the wave number), is varying in space, during the interaction, due to the presence of the optical pump laser. As we will show when we derive the dispersion relation for the probe laser in the presence of the probe pulse, it is reasonable to assume a phase velocity for the probe pulse of the type

$$v_\phi = 1 + \alpha\xi E_0^2(x),$$

where $\alpha$ is a constant and $E_0(x)$ the profile of the pump laser. Applying the relation between wave number and phase velocity and assuming that this profile can be decomposed as a product of an amplitude with an arbitrary function of order one with a scale of variation $\lambda_0$, $E_0(x) = E_0 g(x)$, we obtain that

$$k(x)^2 \approx k_p^2 \big[1 + 2\alpha\xi E_0^2 g^2(x)\big] \ , \tag{4.28}$$

where $k_p$ is the wave number of the probe in the classical vacuum. Inserting this expression for the wave number in the criteria of validity eq.(4.26) derived from the original wave equation yields the condition under which the WKB approximation can be used for our setup. This criteria is therefore,

$$\frac{\lambda_p}{\lambda_0} \ll 1. \tag{4.29}$$

The approximation is therefore valid in the slowly varying package limit, or in other words, as long the the wave-length of the probe pulse is much smaller than the wavelength of the probe laser. This condition is readily verified in the experimental conditions of interest due to the difference of scales of the x-ray probe pulse compared to the optical pump laser.

In this section we have derived the WKB approximation as a powerful tool to solve wave equations with a spatial-dependent wave number. We then applied the WKB criteria to the setup of interest in the context of vacuum birefringence and showed that the method can be applied due to the separation of scales between the two laser pulses. Finally, note that this method allows us to calculate the total phase accumulation of the probe pulse after interacting in the quantum vacuum by simply integrating over the profile of the pump laser. This technique will be extremely useful in deriving analytic results for the retardance, and thus the ellipticity induced, in the probe pulse after the interaction.

### 4.2.2 Derivation of the dispersion relation

The WKB derivation of the previous sub-section requires a dispersion relation that specifies the spatial dependence of the wave-number. This will be the purpose of this sub-section, where we will

show that not only is the dispersion relation far more complicated than in the case of a simple strong-static field, but also, new physical phenomena appear due to the fact that the pump fields vary in space and time. To derive the correct dispersion relation we start by calculating the EM invariants that result from the field setup present in eqs.(4.16-4.19), this yields the following non-vanishing invariants:

$$\begin{aligned} E^2 - B^2 &= 2E_{py}E_0 + 2B_{pz}B_0 \ , \\ \vec{E}\cdot\vec{B} &= -(E_0B_{py} + B_0E_{pz}). \end{aligned}$$

Using these invariants it is now possible to calculate all components of the polarization and magnetization of the quantum vacuum, neglecting terms of order $E_p^2E_0$ or smaller. This yields:

$$P_y = 4\xi\left(E_0^2E_{py} + B_0E_0B_{pz}\right) \ , \tag{4.30}$$

$$P_z = 7\xi\left(B_0^2E_{pz} + E_0B_0B_{py}\right) \ , \tag{4.31}$$

$$M_y = -7\xi\left(E_0^2B_{py} + E_0B_0E_{pz}\right) \ , \tag{4.32}$$

$$M_z = 4\xi\left(B_0^2B_{pz} + E_0B_0E_{py}\right) \ . \tag{4.33}$$

With these expressions one must now derive the wave equation for both the electric field components, parallel and perpendicular to the polarization of the pump field. Note that in this scenario both the probe and the pump laser will have a corresponding wave equation that is affected by the QED nonlinearities. However, to make the calculations feasible, we assume that the pump laser is unaffected by the nonlinear interaction with the probe laser. This assumption is reasonable not only due to the difference in amplitudes of each field but it is also a standard assumption when deriving instabilities in plasma physics such as Brillouin or Raman amplification. Taking these considerations into account, we obtain the following wave equation for the parallel component of the probe pulse,

$$\Box E_{py} = 4\xi\left(2(\partial_t\partial_xE_0^2 - \partial_t^2E_0^2)E_{py} + (\partial_xE_0^2 - 3\partial_tE_0^2)(\partial_tE_{py} - \partial_xE_{py}) + 2E_0^2\partial_t\partial_xE_{py} - E_0^2(\partial_x^2 + \partial_t^2)E_{py}\right) \ . \tag{4.34}$$

This differential equation is of the form of a wave equation with a source term linear in $E_{py}$ and it's derivatives but with nonlinear coefficients. Before arriving to the final dispersion relation we will re-write eq.(4.34) in a way that offers greater physical insight regarding what physical effects can be expected,

$$(a_\parallel\partial_t^2 - b_\parallel\partial_x^2)E_{py} = \alpha_\parallel E_{py} + \gamma_\parallel(\partial_tE_{py} - \partial_xE_{py}) + \beta_\parallel\partial_t\partial_xE_{py} \ , \tag{4.35}$$

Where the coeficients are defined as

$$\begin{aligned} \alpha_\parallel &= 8\xi(\partial_t\partial_xE_0^2 - \partial_t^2E_0^2) \ , \\ \gamma_\parallel &= 4\xi(\partial_xE_0^2 - 3\partial_tE_0^2) \ , \\ \beta_\parallel &= 8\xi E_0^2 \ , \\ a_\parallel &= 1 + 4\xi E_0^2 \ , \\ b_\parallel &= 1 - 4\xi E_0^2 \ . \end{aligned}$$

An important test of this result it to verify the limit where the pump field has no spatial or temporal variations (case of a strong static field), we recover the wave equation where only the refractive index of the probe pulse is changed. In this limit we set all derivatives of the pump field to zero which amounts to, $\alpha_\parallel, \beta_\parallel, \gamma_\parallel \to 0$ which leads to the correct result.

Equation (4.35) can de solved by inserting the ansatz $E_{py} \sim e^{jk-j\omega t}$ and solved for $\omega$ yielding the self-consistent dispersion relation. Note that despite the coefficients having spatial and temporal dependence due to the pump laser profile, they vary on a larger scale compared to the characteristic frequency and wavelengths of the probe pulse which permits to approximate these coefficients as quasi static and apply the WKB approximation as described in section 4.2.1. Applying the ansatz we obtain the following dispersion relation,

$$a_\parallel \omega^2 + \omega(j\gamma_\parallel - \beta_\parallel k) - (k^2 b_\parallel + \alpha_\parallel - j\gamma_\parallel k) = 0 \,. \tag{4.36}$$

The dispersion relation is quadratic in $\omega$ and can therefore be solved using the quadratic formula to yield two roots. Before showing the final result we would like to emphasize the fact that all components proportional to $\gamma_\parallel$ in Eq.(4.36), are purely imaginary. This imaginary component in the dispersion relation means that the solution to Eq.(4.36) will be complex, with an imaginary component that will lead to an exponential growth or damping of the probe amplitude in time. Applying the quadratic formula to Eq.(4.36) yields,

$$\omega = \frac{\beta_\parallel k - j\gamma_\parallel \pm \sqrt{(j\gamma_\parallel - k\beta_\parallel)^2 - 4a_\parallel(jk\gamma_\parallel - b_\parallel k^2 - \alpha_\parallel)}}{2a_\parallel} \,. \tag{4.37}$$

From Eq.(4.37), we confirm that a imaginary component arises in the dispersion relation, from the first term proportional to $\gamma_\parallel$ and also from the square-root which is a complex number. This expression appears to depend on all the coefficients in a complex manner. However, taking into account the orderings for realistic simulation parameters, this expression can be heavily simplified. To perform this ordering, one must simply replace the spatial and temporal derivatives of the pump pulse by the characteristic scale of variation, $1/\sigma$ where $\sigma$ is the duration of the pump laser. This process finally yields the following expression for the real and imaginary parts of the dispersion relation,

$$\omega = \omega_r + j\omega_i \,, \tag{4.38}$$

$$\omega_r \approx k\left(\sqrt{\frac{b_\parallel}{a_\parallel}} - \frac{\beta_\parallel}{2a_\parallel}\right) \,, \tag{4.39}$$

$$\omega_i \approx \frac{\gamma_\parallel}{2a_\parallel}\left(1 + \sqrt{\frac{a_\parallel}{b_\parallel}}\right) \,. \tag{4.40}$$

Equations (4.38-4.40), completely describe the propagation of the parallel component of the probe pulse. The same calculation was repeated for the component of the probe perpendicular to the pump

laser yielding equations exactly in the same form but with the coefficients changed to,

$$\begin{aligned}
\alpha_\perp &= 14\xi(\partial_t\partial_x E_0^2 - \partial_t^2 E_0^2), \\
\gamma_\perp &= 7\xi(\partial_x E_0^2 - 3\partial_t E_0^2), \\
\beta_\perp &= 14\xi E_0^2, \\
a_\perp &= 1 + 7\xi E_0^2, \\
b_\perp &= 1 - 7\xi E_0^2 \,.
\end{aligned}$$

A crucial conclusion of this analysis is the fact that both the real part and imaginary part of the dispersion relation for the parallel and perpendicular components are different. This means that the phase velocity of each component will be different and thus an ellipticity will be induced in the polarisation as already discussed previously. Furthermore, we have shown that there is a damping in the amplitude of the probe pulse due to the space-time variation of the pump laser during the nonlinear interaction. The fact that the damping factor is different for both the parallel and perpendicular components means that after the interaction, they will no longer have the same amplitude. This mismatch in the amplitude of both components, small as it may be, will induce a rotation in the polarization angle of the probe pulse that will be detected when the probe pulse crosses the detector, as explained in 4.1.3. Finally, the fact that the damping rate does not depend on the probe wavenumber but rather only on the characteristics of the pump, is a valuable conclusion.
The phenomena of the rotation of polarisation had already been predicted in previous work [29, 46, 47] by computing the number of photon that flip from one polarisation to another using a QED formalism. Furthermore, Dipiazza et.al in[29], predicted the rotation of polarisation in a different setup using an EM formalism. However, to our knowledge, the derivation presented here is a novelty regarding the setup proposed, and the dispersion relation, Eqs.(4.38-4.40), had not yet been derived.

So far, in the previous sections we derived the two observable physical consequences from the quantum interaction between a strong optical pump laser and a X-ray probe. In particular, we showed that the different phase shifts introduced in each polarization component of the probe due to the respective phase velocities induces an ellipticity in the polarization whilst a damping mechanism in the amplitudes of each polarisation component yields a rotation in the direction of polarisation of the pulse. As already emphasized, this setup of great experimental relevance, can be simulated with the algorithm developed in our work. In the next section we will analyse the results of the simulations performed and compare with our theoretical predictions in both a quantitative an qualitative manner.

### 4.2.3 Simulation result analysis

A crucial feature present in the simulations performed is the difference in scales between the two laser pulses. This difference in scales (optical to X-ray) is about 3 orders of magnitude. Furthermore, the simulation parameters had to be such that the wavelength of the X-ray probe could be resolved with a criteria of 20 points per wavelength but also the width of the wave packages must be captured

within the simulation domain. Finally, and the simulation duration has to be such that the time before, during and after the interaction can be simulated. These restrictions bring us to a crucial point of this work: the fact that large computational resources are necessary to perform such simulations and that the algorithm must be fully paralelized to operate on large computing clusters.The simulations about to be presented were performed at the ACCELERATES cluster (Lisbon, Portugal). A typical simulation about to be presented lasted 12 hours using 1800 cores of ACCELERATES which is equivalent to approximately 22k computational hours. The fact that the algorithm we implemented was done so in a fully parallel way represents a significant competitive advantage.

Table **??** summarizes the laser parameters used for the simulations and corresponding real parameters before normalization. The laser parameters used correspond to the proposed beam parameters for the LCLSII update and the new SLAC X-ray laser. Finally, regarding the value of the quantum coupling parameter $\xi$, we chose to vary this parameter whilst maintaining the remaining simulation parameters constant. We chose to do so for several reasons, most importantly it allows us to verify if the physical consequences we wish to observe scale linearly with the coupling parameter, but also to rule out numerical artifacts that may only occur below certain values of the $\xi$ parameter. The latter reason is important as we must not forget that the nonlinear vacuum corrections are small compared to the unperturbed fields and therefore, from a computer precision point of view, there will be a limit to the precision of the machine, as well as numerical noise issues.

| Physical Quantity | Pump Laser | | Probe Laser | |
|---|---|---|---|---|
| | Real value | Normalised | Real value | Normalised |
| $\omega$ | $1.88 \times 10^{15}$ | – | $9.5 \times 10^{18}$ | – |
| $\lambda$ | 1 $\mu$m | 1001 | 1.2 nm | 1 |
| Intensity (W cm$^{-3}$) | $10^{23}$ | – | $10^{18}$ | – |
| Electric field (V/m) | $8.69 \times 10^{14}$ | 0.34 | $2.75 \times 10^{12}$ | 0.001 |
| Duration (fs) | 40 | 316 | 40 | 316 |

TABLE 4.1: Laser parameters for the LCLSII update and the new SLAC X-ray laser. For the simulations performed for this setup all quantities were normalised to the X-ray frequency.

The one-dimensional theory previously presented can be applied to the simulation setup shown in fig.4.4 as we used plane waves in the transverse direction for both probe and pump. However, the longitudinal profile of both pulses can be intialised with any function desired. In particular, it is of interest to test how the results vary according to the wave packet of the pump laser. To understand this dependence, we performed simulations of the setup illustrated in fig.4.4 for different values of $\xi$ parameters but also for two different functions for the pump laser profile:

$$E_0(x, t = 0) = E_0 \exp\left(\frac{-(x - x0)^2}{2\sigma^2}\right) , \tag{4.41}$$

$$E_0(x, t = 0) = E_0 \cos(k_0 x) \exp\left(\frac{-(x - x0)^2}{2\sigma^2}\right) . \tag{4.42}$$

Where $k_0$ and $\sigma$ are the wave-number and duration of the pulse, respectively. These profiles were selected to compare the induced ellipticity and rotation of polarisation when the pump laser is a Gaussian package to when that same package is modulated by an oscillating function. Most importantly, whilst eq.(4.42) has associated to it two spatial scales $(\sigma, k_0)$, the profile in eq.(4.41) only has one scale of variation. Furthermore, as we saw in section 4.2.1, the spatial integral over the square of the pump profile is an important quantity that measures the effective length of interaction between the probe pulse and the birefringent medium. The physical reason behind this is the fact the phase of a wave in an inhomogeneous media is the sum of the optical phase in each layer of infinitesimal width. This motivates us to calculate the spatial integral of the square of both pump profiles in order to estimate what can be expected in each case. This calculation yields,

$$\int_{-\infty}^{\infty} \exp\left(\frac{-(x-x0)^2}{2\sigma^2}\right) dx = E_0^2\sqrt{\sigma^2\pi}, \tag{4.43}$$

$$\int_{-\infty}^{\infty} \cos^2(k_0 x) \exp\left(\frac{-(x-x0)^2}{2\sigma^2}\right) dx = E_0^2\sqrt{\sigma^2\pi}\left(\frac{e^{-(k_0\sigma)^2}+1}{2}\right). \tag{4.44}$$

Eq.(4.43) can be recovered as a limit of Eq.(4.44) by taking limit $k_0 \to 0$ which corresponds exactly to making the wavelength of the oscilating modulation of the pump laser to infinity thus recovering the laser profile eq.(4.41) from eq.(4.42). Furthermore, since for the simulations performed, the quantity $k_0\sigma \approx 20$, the exponential of this number squared in eq.(4.44) is approximately zero, meaning that in practice, the results of these integrations differ approximately by a factor of two, i.e.

$$\int_{-\infty}^{\infty} \exp\left(\frac{-(x-x0)^2}{2\sigma^2}\right) dx = E_0^2\sqrt{\sigma^2\pi}, \tag{4.45}$$

$$\int_{-\infty}^{\infty} \cos^2(k_0 x) \exp\left(\frac{-(x-x0)^2}{2\sigma^2}\right) dx \to E_0^2\frac{\sqrt{\sigma^2\pi}}{2}. \tag{4.46}$$

This last limit corresponds to the existence of multiple wavelengths within the pump envelope. We therefore expect the results of the simulations for both cases, in terms of the ellipticity induced and rotation of polarisation, to differ by a factor of approximately two.

The simulations were performed for values of $\xi = [10^{-4} - 10^{-7}]$ for both profiles. Figure 4.5(a), shows the result of the ellipticity diagnostic after a rotation by $\theta_0 = -\pi/4$ applied to a simulation with $\xi = 10^{-4}$ and the pump profile eq.(4.41). In red, we see the plot of the fitted expression to the outer ellipse. Figure 4.5(a) shows that an ellipticity was induced and a polarisation rotation of the probe pulse. This angle of rotation can be measured from this diagnostic by measuring the angle between the major axis of the ellipse and the horizontal axis in Fig. 4.5(a). This angle is automatically given as an output of the fitted ellipse and serves as a direct measurement of the rotation in the polarisation. Figure 4.5(b) shows the same ellipse, but further rotated by this residual angle from the rotation in polarisation thus centering the ellipse about the $E_y$ axis. A new fit of the centered ellipse was performed and is shown in Fig.4.5(b). This procedure was done to show that the ellipse parameters obtained from the fit are invariant under coordinate rotation. Finally, one qualitative conclusion can be extracted from the result if this diagnostic: in Fig. 4.5(a) the major axis of the ellipse makes a negative angle with the horizontal axis after being rotated by the initial polarisation angle $\theta_0 = \pi/4$,

which means that the polarisation after the interaction has changed by an angle $\theta < \pi/4$. From this we conclude that the amplitude of the $E_z$ component of the probe was damped by a greater amount than the $E_y$ component. This result is qualitatively consistent with the theoretical expression derived for the damping rate in Eq.(4.38) with $\gamma_\perp > \gamma_{||}$ leading to a greater damping rate for the perpendicular ($E_z$) component than for the parallel ($E_y$).

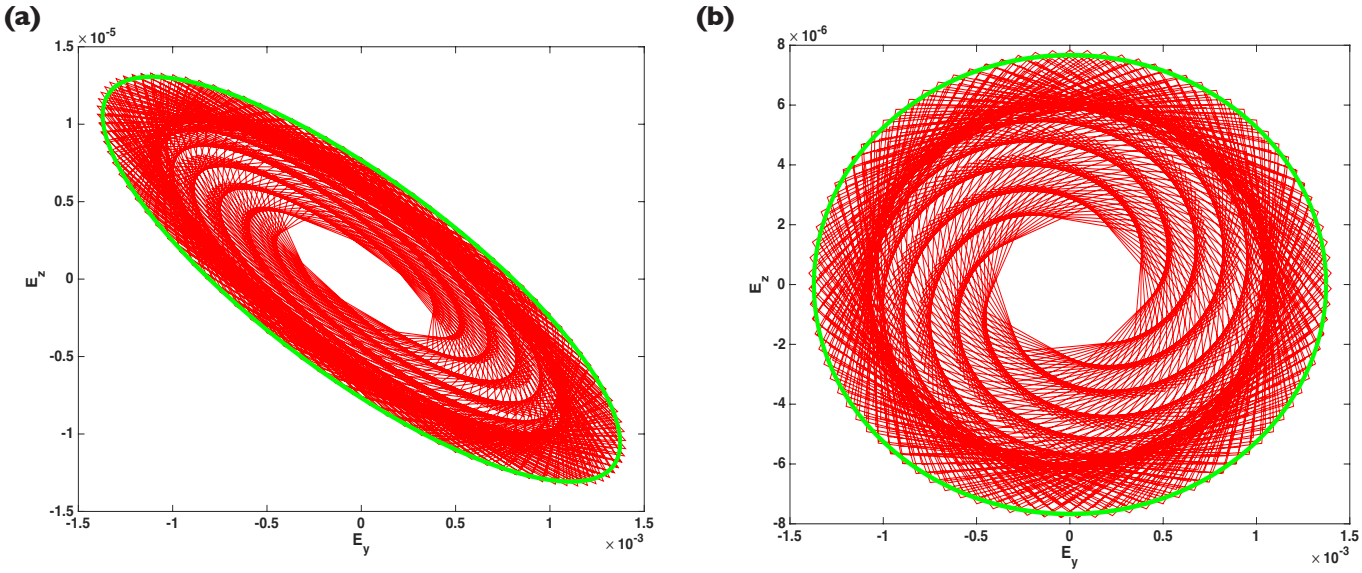


FIGURE 4.5: Figure showing the results of the ellipticity diagnostic with the respective fit performed. In (a) the original polarization was rotated by $\theta = -\pi/4$ where we see that the residual angle that remains indicates the quantum interaction created a rotation in the original direction of polarization. In (b) we show figure (a) but rotated once again by this residual angle, measured from the diagnostic, to verify that the fitting parameters are invariant under coordinate rotations.

Using the results derived so far, we will now derive theoretical expressions for both the ellipticity induced and polarisation rotation angle, based on the dispersion relation eq.(4.38-4.40) and respective equations for the perpendicular component of the field. The ellipticity induced in the polarization of the probe pulse can be calculated using the WKB approximation by integrating the phase of each component during the interaction period and subtracting each of the accumulated phases. Multiplying this phase difference by the wave number of the probe pulse yields the ellipticity. This calculation was repeated for each type of pump profile yielding

$$\delta_{\text{theo1}} = \frac{3}{2} k_0 \sqrt{\pi} \sigma \xi E_0^2 \,, \tag{4.47}$$

$$\delta_{\text{theo2}} = 3 k_0 \sqrt{\pi} \sigma \xi E_0^2 \,. \tag{4.48}$$

Where the 1,2 subscripts refer to each pump profile, Eqs.(4.41-4.42), respectively. In this calculation the real part of the dispersion relation was approximated by Eq.(4.39). Note that Eqs.(4.47-4.48) differ by a factor of 2, due to the integration over the pump profile, as already explained. The ellipticity

diagnostic yields the value of the minor radius of the ellipse that can then be related to the ellipticity by the expression,

$$\delta_{\text{sim}} = \frac{2\sqrt{2}}{E_p} b_{\text{sim}} \ . \tag{4.49}$$

This result can then be compared to the theoretical expressions, Eqs.(4.47-4.48). Having derived theoretical expressions for the ellipticity expected from the simulation, using the real part of the dispersion relation, we also derived the corresponding theoretical angle of rotation. This was done by estimating the imaginary part of the dispersion relation thus arriving at the expected damping rate of each component given by

$$\Gamma_{\parallel 1} \approx 4\xi E_0^2 \sigma, \tag{4.50}$$

$$\Gamma_{\perp 1} \approx 7\xi E_0^2 \sigma, \tag{4.51}$$

$$\Gamma_{\parallel 2} \approx 8\xi E_0^2 \sigma, \tag{4.52}$$

$$\Gamma_{\perp 2} \approx 14\xi E_0^2 \sigma \ . \tag{4.53}$$

Where again, the 1,2 subscripts refer to each pump profile. The final polarisation angle ($\theta$) is related to the ratio of the amplitudes of each component, after the interaction, by the expression

$$\tan(\theta) = \frac{E_z}{E_y} = \exp(-(\Gamma_\perp - \Gamma_\parallel)). \tag{4.54}$$

Inserting Eqs.(4.50-4.53) into Eq.(4.54) and noting that the rotation in the initial polarisation of $\theta_0 = \frac{\pi}{4}$, due to the HE quantum vacuum will be given by the final angle measured subtracted by the initial angle $\theta_0$, allows us to arrive at the final expression for the angle of rotation of polarisation that can be compared to that extracted from the simulation. These expressions, for each case of the pump profile, are given by,

$$\Delta\phi_{\text{theo1}} = \frac{\pi}{4} - \arctan\left(e^{-3\xi E_0^2 \sigma}\right), \tag{4.55}$$

$$\Delta\phi_{\text{theo2}} = \frac{\pi}{4} - \arctan\left(e^{-6\xi E_0^2 \sigma}\right), \tag{4.56}$$

The simulation described was repeated for different values of $\xi$. The ellipticities induced and the polarisaion rotation angles were extracted from the simulation and are plotted in fig.4.6(a)-(b). The same plot also includes the corresponding theoretical expressions eqs(4.47-4.48) and eqs.(4.55-4.56), respectively.

The first conclusion that can be drawn from the results presented in fig.4.6(a)-(b) is that the simulation points both for the ellipticity induced and also for the polarisation rotation angle, change by a factor of 2 when comparing the results with each type of pump profile. This result is in remarkable agreement with what we had predicted by performing a spatial integration over the pump profile and seems to indicate that the effect of the longitudinal profile of the pump can be taken into account using our technique, motivated by the WKB approximation. On the other hand, for both physical quantities, the theoretical expressions previously derived and plotted as the orange and blue lines

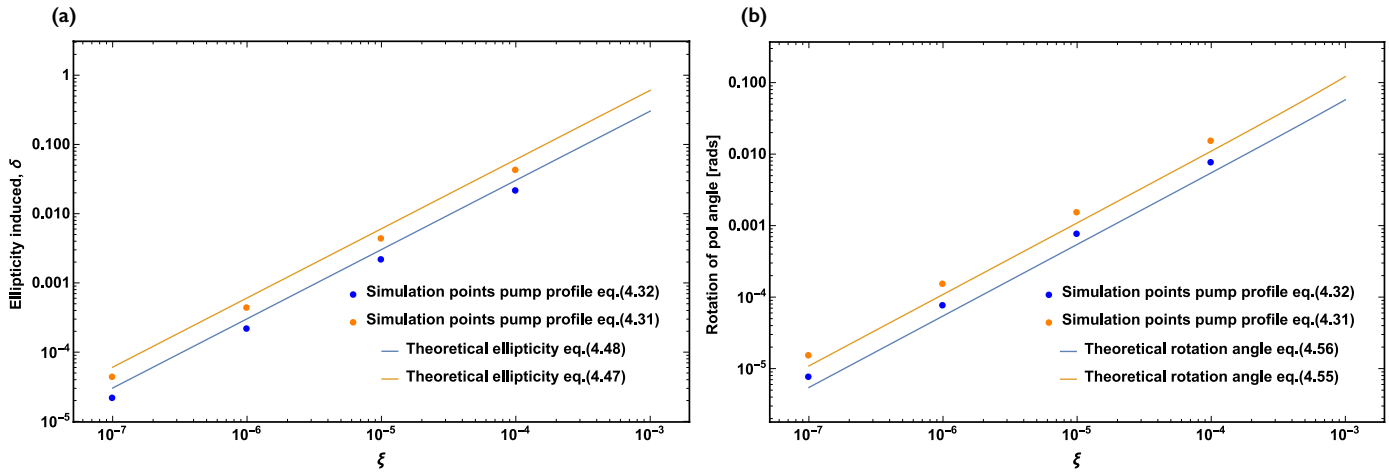


FIGURE 4.6: (a) Figure comparing the ellipticities extracted from the simulations performed for different values of the quantum coupling parameter. The points in blue and orange refer to the results of the simulations using eqs.(4.42),4.41), respectively and are compared to the theoretical expressions derived for the corresponding pump profile, eqs.(4.48,4.47), respectively. (b) Figure comparing the rotation of polarization angle extracted from the simulations performed for different values of the quantum coupling parameter. The points in blue and orange refer to the results of the simulations using eqs.(4.42),4.41), respectively and are compared to the theoretical expressions derived for the corresponding pump profile, eqs.(4.56,4.55), respectively.

show a good agreement with the simulation results up to a multiplicative factor of the order of unity. Nevertheless, the theoretical expressions deliver results with the correct order of magnitude. The fact that the theoretical expressions do not agree as closely as those of simulations from previous sections may be due to a several number of reasons that we will now discuss.

Both from a theoretical and computational point of view, the simulations presented in this section are extremely complex. Furthermore, the theoretical analysis performed to derive the relevant dispersion relations assumed that the propagation of the pump in the quantum vacuum is not modified which should be the case, however due to finite resolution numerical effects may not be the case due to the interpolation of the invariants. The main reason for the small mismatch lies the method used to derive the damping rates for the polarisaton rotation angle, which was rather crude as the spatial and temporal derivatives of the laser pump were simply replaced by the characteristic scale of variation of the pump, $1/\sigma$.

Despite the agreement between theory and simulation not being perfect, we were able to derive useful expressions and above all, show that the algorithm is able to reproduce all the physical effects that we predicted, most importantly, we have shown that these physical effects scale linearly with the quantum parameter $\xi$ of the simulation. This final conclusion if extremely valuable, as it shows that for future more complex simulations, it is reasonable to use an increased value of $\xi$ compared with the physical value, without changing the reliability and accuracy of the physical results obtained. Another conclusion that cannot be illustrated in the results directly but serves as an important test of the diagnostic, is that the fitting parameters of the ellipse do not vary when one varies the position detector in the transverse direction. This had to be the case since we used plane waves in the transverse direction and therefore the fields are constant for any line-out.

To conclude, we have shown that our algorithm can be used to simulate setups of experimental interest aiming to detect the existence of the quantum vacuum by measuring changes in the ellipticity and angle of polarisation of a X-ray pulse probing a birefringent vacuum created by a strong pump. This final demonstration illustrates how the algorithm developed in this Master thesis can be a powerful tool for the strong field QED community by delivering simulation results in multi-dimensional EM setups that can complement the theoretical work being developed using other formalisms, to understand the quantum vacuum.

# Chapter 5

# Conclusions and future prospects

The work developed throughout this master thesis had the objective of developing a computational tool to study the quantum vacuum, encompassing theoretical, numerical and high performance computing concepts. In this final chapter we wish to state an overview of the work performed and reiterate the main conclusions which we believe can contribute to the development of the field and be considered in the short term for several projects planned to study the quantum vacuum detect the existence of the quantum vacuum rather than setting an upper limit to the coupling constant.

Regarding the outcome of this master thesis, a numerically stable and robust generalized FDTD scheme to solve the nonlinear set of QED Maxwell's equations was developed and incorporated in a standard PIC loop. This work represents an important step towards modeling plasma dynamics in extreme scenarios when QED processes significantly alter the collective behavior of the system. The algorithm developed to tackle the nonlinearity of the set of QED Maxwell's equations, as well as the numerical aspects of precision and stability were described in Chapter 2. From the numerical analysis, we derived a nonlinear numerical dispersion relation and showed that for typical simulation times, the algorithm is stable. Nevertheless, due to the nonlinear nature of the equations, we showed that there will always be a small growth rate associated to a numerical wave, and derived the time scale in which the algorithm will become unstable.

In Chapter 3, we presented simulations confirming predicted optical phenomena such as vacuum birefringence and high harmonics generation in one-dimensional setups, delivering results with an excellent accuracy. The code was also extended for two-dimensional scenarios where two setups of interacting Gaussian beams were studied. The results highlight the importance of transverse beam effects and hint that the generation of higher harmonics from quantum vacuum can be achieved via this interaction. The spectrum of the harmonics could provide a direct measurement of important beam properties such as the peak intensity and alignment. This algorithm may also be used to test two and three dimensional setups that have been proposed in the literature (where transverse and finite spot size effects are taken into account under certain approximations), thus complementing the results of previous theoretical works [29, 46].

Once the algorithm was properly tested and benchmarked in multi-dimensions, we concentrated our efforts on performing simulations and theoretical analysis of a setup with short term experimental relevance using realistic laser parameters. This was the purpose of chapter 4, to verify using self-consistent simulations that a probe pulse will acquire a rotation and ellipticity of the polarisation, when counter-propagated with a strong laser pump. To achieve this objective we developed important diagnostic tools to measure the polarisation of a pulse in the simulation domain. Furthermore,

we developed a fully EM theoretical model to arrive at a dispersion relation for the simulation setup of interest thus obtaining theoretical predictions for the ellipticity induced and rotation of polarisation angle. These theoretical expressions were compared to the corresponding simulation quantities extracted using the diagnostic, showing a good agreement. Finally, we repeated the simulation setup using a realistic pump profile, including transverse effects, and were able to show that in this case both the ellipticity induced and rotation of polarisation angle vary according to the off axis distance. Although a theoretical analysis of this last complex setup was not performed, the results are a demonstration of how useful the algorithm developed can be to provide predictions regarding experimentally significant quantities, in a self-consistent manner. We conclude from Chapter 3 and Chapter4 that our algorithm contributes to the generalization of the Yee scheme, one of the most successful and commonly used algorithms in computational physics, to scenarios where nonlinear polarization and magnetization can impact EM propagation. This code can be used to benchmark planned experiments, leveraging on ultra-intense laser facilities able to deliver intensities of $10^{23} - 10^{24}$ W/cm$^2$, to verify for the first time the dynamics of the quantum vacuum below the Schwinger limit.

We believe that our algorithm paves the way to a series of future work that can be orientated towards the needs of the strong field QED community. The fact that all around the world, top laser facilities are upgrading their ultra-intense laser sources to unprecedented intensities, presents an opportunity for the computational tool developed in this work to deliver sound predictions of the magnitude of the phenomena that can be expected when probing the quantum vacuum. In particular, the fact that realistic experimental setups involve complex optical phenomena, makes the problem unattainable from a theoretical point of view and extremely demanding from a computational point of view. The fact that our work is fully self-consistent within an EM framework and computationally paralelized in order to run on large super computing clusters, is crucial for the strategic relevance of our algorithm. In concrete terms, it would be extremely useful to simulate the setup described in Chapter 4, simulataneously using realistic pulse profiles for both pump and probe, rather than a plane wave for the probe. In particular, the fact that we can vary initial parameters such as the focus, divergence and intensity profile of the laser, means we will be able to perform a parameter scan and understand exactly what are the laser parameters that deliver the largest experimental signatures of the quantum vacuum. This will be pursued in a near future by our group.

One feature of the algorithm that was mentioned but not investigated in this work due to scope limitations, is the fact that our QED solver is fully integrated within the PIC code OSIRIS. This means that one could simulate usual plasma dynamics, at a kinetic scale, but using a Maxwell's equations solver that takes into account the quantum vacuum corrections. This can be extremely useful in astrophysical scenarios where fields of the order of the Schwinger limit dictate the dynamics of the system.

The work in [49], showed that in extreme scenarios such as neutron star and pulsar magnetospheres, it is likely that General Relativity (GR) effects, assume a greater role compared to QED corrections in terms of the macroscopic properties of the system such as the spin-down luminosity. However, the photon busrts emmitted from such system have to traverse large distances in the presence of strong magnetic fields and the respective plasma present in the magnetosphere. The existence of observational signatures, in the detected, of high magnetic field phenomena associated to

the quantum vacuum corrections can help understand the magnetic field profiles present in the system and thus help clarify the dynamics of such ultra-intense systems. A thorough review of all the physical processes that are important in neutron star interiors and magnetospheres of pulsars, can be found in [50], including the modification to the photon modes in the presence of strong magnetic fields and the plasma in these extreme scenarios. The conclusions of these simulations may then be used to identify what, if any, physical mechanisms regarding quantum vacuum-plasma interaction are relevant.

To conclude, we believe that the work developed in this Master thesis will have a significant impact in the strong field QED community and open many doors towards future collaborations with other top theoretical and experimental laser facilities around the world with the objective of understanding and probing the quantum vacuum for the first time.

# Bibliography

[1]T. Rothman, *Everything's Relative: And Other Fables from Science and Technology*, **Comment**: Great book on common misconseptions and unclaimed heroes in the history of Physics. (Sept. 2003), p. 72.

[2]P. A. M. Dirac, "The quantum theory of the electron", Proceedings of the Royal Society of London A: Mathematical, Physical and Engineering Sciences **117**, **Comment**: P.Dirac's groundbreaking paper where the equation bearing his name is first introduced, with the respective consequences explored., 610–624 (1928).

[3]P. A. M. Dirac, "Quantised singularities in the electromagnetic field", Proceedings of the Royal Society of London A: Mathematical, Physical and Engineering Sciences **133**, **Comment**: Groundbreaking article where the hole theory is first introduced and the positron proposed, 60–72 (1931).

[4]W. Heisenberg, "The fluctuations of charge connected with the formation of matter from radiation", Schsiche Akad. Wissen **86**, **Comment**: Formal treatment of vacuum fluctuations is performed using formalism already developed by Heisenberg. (1934).

[5]W. Heisenberg, "Comments on the dirac theory of the positron", Z.Phys. **90**, **Comment**: Heisenberg's interpretation of Dirac's theory is stated and the conclusion that quantum fluctuations lead to vacuum polarization. (1934).

[6]H. E. W. Heisenberg, "Folgerungen aus der diracschen theorie des positrons" zeitschr", Z.Phys. **98**, **Comment**: Fundamental paper on which this theory is based. The full nonlinear corrections to Maxwell's equations are computed and the weak field, low frequency approximation is derived. English translation can be found in arXiv:physics/0605038 [physics.hist-ph] (1936).

[7]F Sauter, "Ãber das verhalten eines elektrons im homogenen elektrischen feld nach der relativistischen theorie diracs", Z.Phys **69**, **Comment**: Original article where the process of pair production was addressed by Sauter as a tunneling process (1931).

[8]G. V. Dunne, "The heisenberg-euler effective action: 75 years on", International Journal of Modern Physics A **27**, **Comment**: Accurate historic overview of the HE QED corrections, ranging from the work of Dirac that motivated Heisenberg, to the subsequent work by J.Schwinger. (2012).

[9]C. Danson, D. Hillier, N. Hopps, and D. Neely, "Petawatt class lasers worldwide", High Power Laser Science and Engineering **3**, **Comment**: Recent overview of facilities available to deliver > 200 TW. The main techniques for amplification and applications of such technology are also discussed. (2015).

[10]A. Spitkovsky, "Electrodynamics of Pulsar Magnetospheres", in Young neutron stars and their environments, Vol. 218, edited by F. Camilo and B. M. Gaensler, IAU Symposium, **Comment**: Revision of current understanding of the electrodynamics of pulsar magnetospheres and the main challenges in modelling such systems. (2004), p. 357.

[11]J. S. Heyl and N. J. Shaviv, "Qed and the high polarization of the thermal radiation from neutron stars", Phys. Rev. D **66**, **Comment:** In this article quantitative predictions of vacuum polarization effects on the dynamics of pulsar emmited radiation, are made. This work also proposes how these effects may be measured by detectors on earth and serve as evidence for the existence on the non-linear QED vacuum, 023002 (2002).

[12]R. A. Fonseca, L. O. Silva, F. S. Tsung, V. K. Decyk, W. Lu, C. Ren, W. B. Mori, S. Deng, S. Lee, T. Katsouleas, and J. C. Adam, *OSIRIS: A three-dimensional, fully relativistic particle in cell code for modeling plasma based accelerators*, Vol. 2331, **Comment**: Massivelly parallel fully relativistic PIC code developed in a collaboration between IST and UCLA. The algorithm developed in this thesis shall be incorporated in this code. (Springer Berlin / Heidelberg, 2002), pp. 342–351.

[13]J. M. Dawson, "Particle simulation of plasmas", Rev. Mod. Phys. **55**, **Comment**: Review of the PIC method, difficulties associated to the method and an interesting opinion on how such computational techniques can power future research in plasma physics., 403–447 (1983).

[14]D. Griffiths, *Introduction to elementary particles*, Physics textbook, **Comment**: Chapter 11 includes a brief and complete overview on how to create a field theory from a given Lagrangian density and how to extract physical significance from local symmetry groups. (Wiley, 2008).

[15]M. Vranic, G. T., R. A. Fonseca, and L. O. Silva, "Quantum radiation reaction in head-on laser-electron beam interaction", ArXiv **1511.04406**, **Comment**: QED-PIC code simulations results and theoretigal models that investigate the evolution of the energy spread and the divergence of electron beams while they interact with different laser pulses at intensities where quantum effects and radiation reaction are of relevance. (2015).

[16]D. Green and C. Harvey, "Simla: simulating particle dynamics in intense laser and other electromagnetic fields via classical and quantum electrodynamics", Computer Physics Communications **192**, 313 –321 (2015).

[17]T. G. Blackburn, C. P. Ridgers, J. G. Kirk, and A. R. Bell, "Quantum radiation reaction in laser electron-beam collisions", Phys. Rev. Lett. **112**, 015001 (2014).

[18]N. V. Elkina, A. M. Fedotov, I. Y. Kostyukov, M. V. Legkov, N. B. Narozhny, E. N. Nerush, and H. Ruhl, "Qed cascades induced by circularly polarized laser fields", Phys. Rev. ST Accel. Beams **14**, **Comment**: Monte-Carlo simulations of electron-positron-photon cascades initiated by slow electrons in circularly polarized fields of ultra-high strength are presented and discussed. This serves to show how different numerica tools complement each other in the self-consistent modeling of QED phenomena within ultra-intense laser-matter physics., 054401 (2011).

[19]M. Vranic, T. Grismayer, J. Martins, R. Fonseca, and L. Silva, "Particle merging algorithm for pic codes", Computer Physics Communications **191**, 65 –73 (2015).

[20]T. Grismayer, M. Vranic, J. L. Martins, R. Fonseca, and S. L. O, "Seeded qed cascades in counter propagating laser pulses", ArXiv **1511.07503**, submitted to Physical Review E (2015).

[21]T. Grismayer, M. Vranic, J. L. Martins, R. A. Fonseca, and L. O. Silva, "Laser absorption via quantum electrodynamics cascades in counter propagating laser pulses", Physics of Plasmas" **23**, 056706, **Comment:** A model for laser light absorption in electron-positron plasmas self-consistently created via QED cascades is described. QED cascades are studied with multi-dimensional particle-in-cell

simulations complemented by a QED module and a macro-particle merging algorithm that allows to handle the exponential growth of the number of particles. (2016).

[22]C. P. Ridgers, C. S. Brady, R. Duclous, J. G. Kirk, K. Bennett, T. D. Arber, and A. R. Bell, "Dense electron-positron plasmas and bursts of gamma-rays from laser-generated quantum electrodynamic plasmas)", Physics of Plasmas **20**, 056701 (2013).

[23]M. Vranic, J. L. Martins, J. Vieira, R. A. Fonseca, and L. O. Silva, "All-optical radiation reaction", Phys. Rev. Lett. **113**, **Comment**: 3D full-scale particle-in-cell simulations showing that the radiation reaction dominated regime can be reached in an all-optical configuration through the collision of a 1 GeV laser wakefield accelerated electron bunch with a counterpropagating laser pulse., 134801 (2014).

[24]A. Gonoskov, S. Bastrakov, E. Efimenko, A. Ilderton, M. Marklund, I. Meyerov, A. Muraviev, A. Sergeev, I. Surmin, and E. Wallin, "Extended particle-in-cell schemes for physics in ultrastrong laser fields: review and developments", Phys. Rev. E **92**, **Comment**: Review of state-of-the-art PIC simulation techniques including QED processes. Future challenges are stated and current limitations are explained., 023305 (2015).

[25]T. Heinzl and A. Ilderton, "Exploring high-intensity qed at eli", English, The European Physical Journal D **55**, **Comment**: Overview on the many QED phenomena that we expect to be able to probe using the intensities to be achieved in the ELI project. Simple description of each process, with relevant references and state of the art understanding, is given. (2009).

[26]A. Di Piazza, C. Müller, K. Z. Hatsagortsyan, and C. H. Keitel, "Extremely high-intensity laser interactions with fundamental quantum systems", Rev. Mod. Phys. **84**, **Comment**: Extremely thorough review of strong field QED processes and how such phenomena can be detected and can affect laser-laser, laser-matter interactions., 1177–1228 (2012).

[27]J. J. Klein and B. P. Nigam, "Birefringence of the vacuum", Phys. Rev. **135**, **Comment**: Vacuum birefringence derivation from HE QED Maxwell equations. Despite an error in the equations arrived for the phase velocity in equation (12), the remaining physical insight given if very relevant. (1964).

[28]G. Zavattini, U. Gastaldi, R. Pengo, G. Ruoso, F. D. Valle, and E. Milotti, "Measuring the magnetic birefringence of vacuum: the pvlas experiment", International Journal of Modern Physics A **27**, **Comment**: Detailed review on the physics of vacuum birefringence due to HE QED nonlinearities. Excellent explanation of experimental setup and some results are displayed, in a concise way. (2012).

[29]A. Di Piazza, K. Z. Hatsagortsyan, and C. H. Keitel, "Light diffraction by a strong standing electromagnetic wave", Phys. Rev. Lett. **97**, **Comment**: The theoretical approach used in this work to derive the correction to the probe pulse wave package due to the HE QED nonlinearities is useful and must be generalized for the theoretical work to be developed in this thesis., 083603 (2006).

[30]T. Cowan, Sauerbrey, Schlenvoigt, and Schramm, **Comment**: Results of this experiment are to appear in the upcoming year. (2016).

[31]M. Soljaic and M. Segev, "Self-trapping of electromagnetic beams in vacuum supported by qed nonlinear effects", Phys. Rev. A **62**, **Comment**: Quasi-3D EM setup, yielding an extremely interesting conclusion: after two beams interact at right angles, the resuling wave packet can be a spatial soliton due to the HE QED modified Maxwell equations., 043817 (2000).

[32]B. King, A. Di Piazza, and C. H. Keitel, "A matterless double slit", Nat Photon **4**, **Comment**: Appealing experimental setup and results that it is possible to produce an interference pattern resembling that produce by a double-slit experiment. This result is to be reproduced in this thesis., 92–94 (2010).

[33]G. Brodin, M. Marklund, and L. Stenflo, "Proposal for detection of qed vacuum nonlinearities in maxwell's equations by the use of waveguides", Phys. Rev. Lett. **87**, **Comment**: Novel experimental setup to detect QED nonlinearities using existing technology. Clear notation of HE Lagrangian., 171801 (2001).

[34]B. King, P. Böhl, and H. Ruhl, "Interaction of photons traversing a slowly varying electromagnetic background", Phys. Rev. D **90**, **Comment**: First numerical algorithm to solve the set of HE QED modified Maxwell equations in a 1D setup including also higher order, multi-photon interactions. The formalism explained in this work is detailed and useful, whilst the results presented are to be repreoduced in this thesis., 065018 (2014).

[35]K. Yee, "Numerical solution of initial boundary value problems involving maxwell's equations in isotropic media", Antennas and Propagation, IEEE Transactions on **14**, **Comment**: FDTD method to solve Maxwell equations. This is the algorithm that must be generalized to take into account the HE QED corrections., 302–307 (1966).

[36]Allen.Taflove and S. C. Hagness, *Computational electrodynamics*, **Comment**: Very informative source regarding numerical foundations of the Yee scheme in multidimensions. Stability and other important concepts are also thoroughly discussed. (Artech House; 3 edition (May 31, 2005), 2005) Chap. 3, pp. 59–62.

[37]J. Mckenna and P. M. Platzman, "Nonlinear interaction of light in a vacuum", Phys. Rev. **129**, **Comment**: Demonstration that the HE QED modified Maxwell equations are unchanged for an arbitrary number of plane waves propagating in the same direction., 2354–2360 (1963).

[38]R. Baier and P. Breitenlohner, "The vacuum refraction index in the presence of external fields", Il Nuovo Cimento B (1971-1996) **47**, **Comment**: Starting from the low energy limit of the polarization tensor for the propagation of a photon in an external field, the expressions for the modified vacuum refractive indexes are derived for the first time., 117–120 (2015).

[39]E. Brezin and C. Itzykson, "Polarization phenomena in vacuum nonlinear electrodynamics", Phys. Rev. D **3**, **Comment**: Pioneer work on the birefringence of the vacuum. In particular, the expressions for the vacuum refractive index due to a strong static electric or magnetic field are derived using a fully covariant formalism. Most importantly, the setup of the experiment to detect the quantum vacuum, explored in Chapte 4, is proposed for the first time., 618–621 (1971).

[40]N. Narozhny and A. Fedotov, "Third-harmonic generation in a vacuum at the focus of a high-intensity laser beam", English, Laser Physics **17**, **Comment**: High Harmonic generation is formally derived in the context of ultra-high intensity laser interactions in the quantum vacuum. The angular spectrum of the scattered photon is computed., 350–357 (2007).

[41]A. Di Piazza, K. Z. Hatsagortsyan, and C. H. Keitel, "Harmonic generation from laser-driven vacuum", Phys. Rev. D **72**, **Comment**: This article investigates the high harmonic generation from vacuum in the field of a superstrong standing laser wave as a possible experimental signature in future experiments., 085005 (2005).

[42]J. Jackson, *Classical electrodynamics*, **Comment**: Reference textbook of advanced Classical Electrodynamics. Very complete chapters regarding mathematical techniques to tackle electromagnetic problems and respective physical interpretations. (Wiley; 3 edition, 1998) Chap. 7.

[43]B. Saleh and M. Teich, *Fundamentals of photonics*, Wiley Series in Pure and Applied Optics, **Comment**: Reference textbook in theoretical and applied optics. A wide range of basic and advanced topics are covered in depth with many problems to work through. (Wiley, 2007).

[44]A. Paredes, D. Novoa, and D. Tommasini, "Self-induced mode mixing of ultraintense lasers in vacuum", Phys. Rev. A **90**, **Comment**: Interesting theoretical approach to the self-interaction and harmonic generation for a Gaussian beam propagting in the Quantum vacuum. This paper provides theoretical benchmarks that could be easily simulated with the tool developed in our work, 063803 (2014).

[45]F. Karbstein, H. Gies, M. Reuter, and M. Zepf, "Vacuum birefringence in strong inhomogeneous electromagnetic fields", Phys. Rev. **D92**, **Comment**: Based on the Fermi Golden rule applied to the low energy limit of the polarization tensor for a Gaussian pulse. The authors predict the expected values for the rotation of polarisation and ellipticity induced in realistic beam geometries, after applying a few approximations. The results of this article can be compared to our simulation results in the appropriate EM setup., 071301 (2015).

[46]V. Dinu, T. Heinzl, A. Ilderton, M. Marklund, and G. Torgrimsson, "Photon polarization in light-by-light scattering: finite size effects", Phys. Rev. D **90**, **Comment**: Using a QED formalism, expressions for photon helicity and polarisation-flip probabilities are in arbitrary background fields that model the laser pump profile., 045025 (2014).

[47]V. Dinu, T. Heinzl, A. Ilderton, M. Marklund, and G. Torgrimsson, "Vacuum refractive indices and helicity flip in strong-field qed", Phys. Rev. D **89**, **Comment**: Lightfront-QED formalism is introduced in this article as a means of modelling the interaction of a photon in a background EM field by integrating over the wordline of the photon using the polarisation tensor., 125003 (2014).

[48]T. Hahn, J. Bierbach, C. Rödel, D. Hemmers, M. Yeung, B. Dromey, S. Fuchs, A. Galestian, S. Kuschel, M. Zepf, G. G. Paulus, and G. Pretzler, "Broadband xuv polarimetry of high harmonics from plasma surfaces using multiple fresnel reflections", Applied Physics B **118**, **Comment**: Pioneer technique to measure the ellipticity and polarisation angle of a light pulse, to an unprecedented precision. The precision limits demonstrated in this work are crucial to compare with the magnitude of the physical effects obtained in our simulations., 241–245 (2015).

[49]J Pétri, "A 3+ 1 formalism for quantum electrodynamical corrections to maxwell equations in general relativity", Monthly Notices of the Royal Astronomical Society **451**, **Comment**: The dynamical equations applicable to the electrodynamics of neutro stars and pulsars, are derived taking into account both General relativity curvature effects and also the QED vacuum nonlinearities. This article

concludes that Relativistic corrections are likely to play a far more important role relative to QED vacuum corrections, in terms of the macroscopic dynamics of the system., 3581–3586 (2015).

[50] A. K. Harding and D. Lai, "Physics of strongly magnetized neutron stars", Reports on Progress in Physics **69**, **Comment**: Extensive review of the possible physical processes occuring in the magnetosphere of pulsars and neutron stars. Amongst the several topics discussed, the effect of vacuum polarization on the outgoing photon sources, in the presence of the magnetic field profile of the system is studied. This reference is extremely interesting for our futurely planned work of studying the high intensity QED processes occuring within these astrophysical systems., 2631 (2006).

# Appendix A

# Appendix

The diagnostic developed to measure the polarisation of a laser pulse, was used throughout Chapter 4 and represents a useful tool for the work performed but also for the future work discussed in Chapter 5. As we saw, a crucial feature in the usefulness of the diagnostic is the ability to fit data to the expression of an ellipse in the general parametric form. However, the ability to relate the geometric coefficients of the fitted ellipse to the physical quantities we wish to extract is crucial as it enables us to deliver physically relevant quantities that can probe the quantum vacuum. In this Appendix we will show how these relations can be derived in a systematic way.

The general parametric form of an ellipse parametrised by $0 \leq t < 2\pi$ with major radius $a$, minor radius $b$, angle of rotation compared to the x-axis $\varphi$ and centered about the point $(X_c, Y_c)$ is given by

$$x(t) = X_c + a\cos(t)\cos(\varphi) - b\sin(t)\sin(\varphi), \tag{A.1}$$

$$y(t) = Y_c + a\cos(t)\sin(\varphi) + b\sin(t)\cos(\varphi). \tag{A.2}$$

Figure A.1 illustrates the geometrical meaning of the parameters defined above.

In the setups considered in this work, the relevant quantities we wish to extract are the ellipticity of the polarisation and the polarisation rotation angle. As we saw, these quantities are closely related to the phase difference and amplitude of the incoming field components, respectively. Therefore, we will assume that once the detector is placed in the simulation domain, it will be recording a pair of fields $(y, x)$ as a function of time. These fields can be written, without loss of generality as

$$y = E_y \cos(t + \varepsilon_1), \tag{A.3}$$

$$x = E_x \cos(t + \varepsilon_2). \tag{A.4}$$

Where $t$ represents time, $E_y$ and $E_x$ are the respective amplitudes of each field component and $\varepsilon_1$, $\varepsilon_2$ represent the phase of each wave. As we already saw, the relation between $E_y$ and $E_x$ will dictate the polarisation angle given by

$$\tan(\theta) = \frac{E_y}{E_x}. \tag{A.5}$$

In particular, if $E_y = E_x$ the polarisation angle of the pulse is $\theta = \pi/4$. On the other hand, $\varepsilon_1$ and $\varepsilon_2$

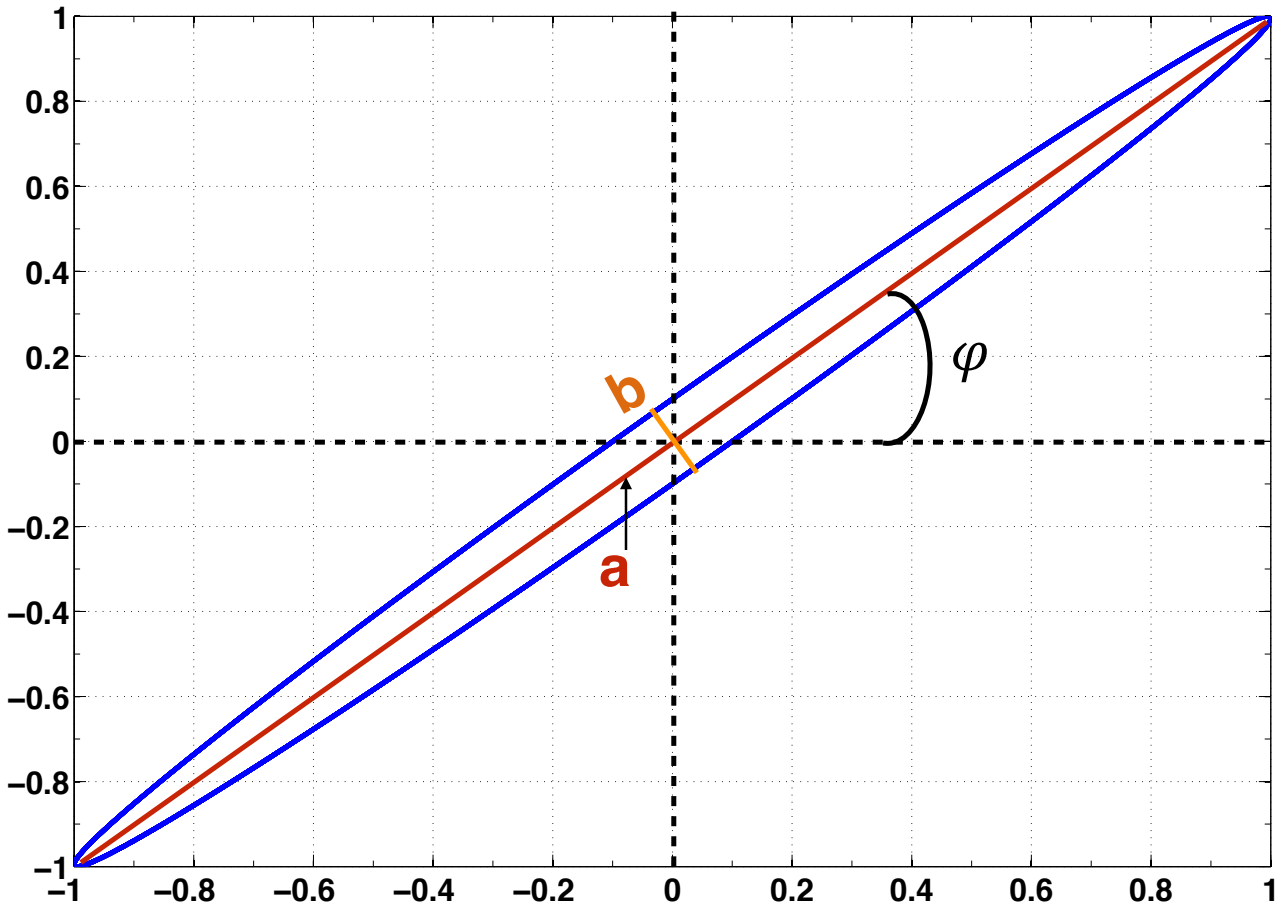


FIGURE A.1: Example of an arbitrary ellipse with the respective defining geometric parameters in the general parametric form.

will determine the ellipticity of the polarisation. Some limiting cases of interest include when $\varepsilon_1 = \varepsilon_2 = 0$, in which case the polarisation is linear, or $\varepsilon_1 - \varepsilon_2 = \pm\frac{\pi}{2}$, in which case the polarisation will be circular.

Eqs.(A.3-A.4), can be expanded using the trigonometry identity of the Cosine of a sum. This yields

$$y = E_y\big(\cos(t)\cos(\varepsilon_1) - \sin(t)\sin(\varepsilon_1)\big), \tag{A.6}$$

$$x = E_x\big(\cos(t)\cos(\varepsilon_2) - \sin(t)\sin(\varepsilon_2)\big). \tag{A.7}$$

Our primary objective is to be abe to relate one of the fitting coefficients to the ellipticity of the polarization, defined as $\delta \equiv \varepsilon_1 - \varepsilon_2$. To do so, we will perform a coordinate rotation on Eqs.(A.6-A.7) by an angle $-\varphi$. Furthermore we will take advantage of the fact that $\varepsilon_1 \sim \varepsilon_2 \ll 1$ due to the perturbative nature of the QED corections induced. This transformation yields

$$y' = (E_y\cos(\varphi) - E_x\sin(\varphi))\cos(t) + (E_x\sin(\varphi)\varepsilon_1 - E_y\cos(\varphi)\varepsilon_2)\sin(t), \tag{A.8}$$

$$x' = (E_y\sin(\varphi) + E_x\cos(\varphi))\cos(t) - (E_x\cos(\varphi)\varepsilon_1 + E_y\sin(\varphi)\varepsilon_2)\sin(t) \tag{A.9}$$

So far this is general, however, it will be of interest that this angle of rotation corresponds to the initial polarisation angle so that we can center the major axis of the ellipse along the $x$ axis. Furthermore, it is interesting to analyse a few limiting cases of Eqs.(A.8-A.9). We start of by taking the limit where $\varphi = pi/4$, this yields

$$y' = \frac{E_y - E_x}{\sqrt{2}}\cos(t) + \frac{E_x\varepsilon_1 - E_y\varepsilon_2}{\sqrt{2}}\sin(t), \tag{A.10}$$

$$x' = \frac{E_y + E_x}{\sqrt{2}}\cos(t) - \frac{E_x\varepsilon_1 + E_y\varepsilon_2}{\sqrt{2}}\sin(t) \tag{A.11}$$

This form can sill not be fully compared to the general parametric form of an ellipse since the rotation of $\pi/4$ only leads to a special case if initially the amplitudes were the same. Therefore, we will now take this further limit where $E_y = E_x = E_0$ to show that when the rotation angle matches the initial polarization angle, we can relate the fitting parameters directly to the ellipticity induced. Applying this final limit to Eqs.(A.10-A.11), we obtain

$$y' = E_0\left(\frac{\varepsilon_1 - \varepsilon_2}{\sqrt{2}}\right)\sin(t), \tag{A.12}$$

$$x' = \frac{2E_0}{\sqrt{2}}\cos(t) - E_0\left(\frac{\varepsilon_1 + \varepsilon_2}{\sqrt{2}}\right)\sin(t). \tag{A.13}$$

This result is very useful since comparing Eqs.(A.12-A.13) with Eqs.(A.1-A.2) we can verify that the ellipticity can be related to the minor radius as

$$b = \frac{E_0}{\sqrt{2}}(\varepsilon_1 - \varepsilon_2) \Rightarrow \delta = \frac{\sqrt{2}b}{E_0}. \tag{A.14}$$

This expression allows us to extract the ellipticity of the polarisation from the fitting parameters, in the case when the amplitudes of the fields are equal.

To arrive at the previous result, we assumed that each phase was small but also that the angle by which we rotated the initial points corresponds to the angle of polarisation (in this example $\pi/4$). However, in the simulations performed, we wish to place the detector in a position to measure the polarisation of the pulse *after* a nonlinear interaction has occured and therefore we may no longer know what the angle of polarisation is, in the case the phenomenon of rotation of polarisation occured. To study this further, we start from Eqs.(A.8-A.9), and apply the substitution $\varphi \to \varphi + \Delta$, where now $\varphi$ is the initial angle of polarisation (which we know), and $\Delta$ is the extra angle of rotation of polarisation induced due to the nonlinear interaction. Applying this transformation we obtain

$$y' = (E_y\cos(\varphi+\Delta) - E_x\sin(\varphi+\Delta))\cos(t) + (E_x\sin(\varphi+\Delta)\varepsilon_1 - E_y\cos(\varphi+\Delta)\varepsilon_2)\sin(t), \tag{A.15}$$

$$x' = (E_y\sin(\varphi+\Delta) + E_x\cos(\varphi+\Delta))\cos(t) - (E_x\cos(\varphi+\Delta)\varepsilon_1 + E_y\sin(\varphi+\Delta)\varepsilon_2)\sin(t) \tag{A.16}$$

This solution can now be expanded taking advantage of the fact that that $\Delta \ll \varphi$ due to the perturbative nature of the quantum vacuum interaction. This expansion allows us to relate the points obtained from the diagnostic, to the two relevant quantities in the problem, the ellipticity $\delta$ and the rotation of polarisation angle $\Delta$.